Structural basis for a nucleoporin exportin complex between RanBP2, SUMO1-RanGAP1, the E2 Ubc9, Crm1 and the Ran GTPase

Vladimir Baytshtok (ORCID: 0000-0002-7390-3580)[1,4], Michael A. DiMattia (ORCID: 0009-0000-8349-3936)[1,2,4], and Christopher D. Lima (ORCID: 0000-0002-9163-6092)[1,3]

[1] Structural Biology Program, Sloan Kettering Institute, Memorial Sloan Kettering Cancer Center, 1275 York Ave, New York, NY 10065

[2] Current address: Schrödinger New York, 1540 Broadway, 24th Floor, New York, NY 10036, USA.

[3] Howard Hughes Medical Institute, 1275 York Avenue, New York, NY 10065

[4] These authors contributed equally

Correspondence should be addressed to C.D.L. (limac@mskcc.org)

Running Title: RanBP2-Crm1-RanGAP1 complex

Summary

The human nucleoporin RanBP2/Nup358 interacts with SUMO1-modified RanGAP1 and the SUMO E2 Ubc9 at the nuclear pore complex (NPC) to promote export and disassembly of exportin Crm1/Ran(GTP)/cargo complexes. In mitosis, RanBP2/SUMO1-RanGAP1/Ubc9 remains intact after NPC disassembly and is recruited to kinetochores and mitotic spindles by Crm1 where it contributes to mitotic progression. Interestingly, RanBP2 binds SUMO1-RanGAP1/Ubc9 with motifs that also catalyze SUMO E3 ligase activity. Here, we resolve cryo-EM structures of a RanBP2 C-terminal fragment bound to Crm1, SUMO1-RanGAP1/Ubc9, and two molecules of Ran(GTP), one bound to Crm1 and the other bound to RanGAP1 and RanBP2. These structures reveal several unanticipated interactions with Crm1 including a nuclear export signal (NES) for RanGAP1, the deletion of which mislocalizes RanGAP1 and the Ran GTPase in cells. Our structural and biochemical results support models in which RanBP2 E3 ligase activity is dependent on Crm1, the RanGAP1 NES and Ran GTPase cycling.

Keywords: Nucleoporin, SUMO, ubiquitin-like modifier, Ran GTPase, exportin, nuclear pore complex, nucleocytoplasmic transport

Introduction

The nuclear pore complex (NPC) coalesces nucleoporin subunits and their phenylalanine-glycine (FG) repeats to present a physical barrier between the nucleus and cytoplasm.[1] Most cargo larger than ~40 kDa can be escorted through the NPC by virtue of nuclear export signals (NES) or nuclear localization signals (NLS) that are recognized by karyopherins that in turn bind FG repeats to traverse the NPC.[2-5] Directionality and cargo release depend on a Ran GTPase gradient with Ran(GTP) in the nucleus and Ran(GDP) in the cytoplasm.[4,6] The Ran gradient is maintained by the cytoplasmic Ran GTPase activating protein RanGAP1 that stimulates GTP hydrolysis to convert Ran(GTP) to Ran(GDP) and the nuclear guanine exchange factor (GEF) Rcc1 that catalyzes GDP-GTP exchange to generate Ran(GTP).[7,8] The nucleoporin RanBP2 (also known as Nup358) resides on the cytoplasmic side of the NPC where it coordinates many of these activities.[9-12] RanBP2 includes FG repeats that interact with karyopherins, Ran binding domains (RBDs) that disengage Ran(GTP) from importin and exportin-cargo complexes, and motifs that interact with SUMO-modified RanGAP1.[13-19]

Ubiquitin (Ub) and ubiquitin-like (Ubl) proteins such as SUMO regulate cellular processes through covalent attachment to proteins or other substrates through a cascade of activities catalyzed by E1 activating enzymes, E2 conjugating enzymes and E3 protein ligases.[20-22] RanGAP1 was the first SUMO substrate identified[14,15,23,24] but unlike most substrates, RanGAP1 can remain bound to the SUMO E2 Ubc9 even after SUMO conjugation.[24-28] Indeed, it is the SUMO-RanGAP1/Ubc9 complex that is recruited to NPCs via RanBP2's IR1-M-IR2 region which contains tandem IR (internal repeat) motifs, each of which includes a SUMO interaction motif (SIM) that binds SUMO and other elements that bind Ubc9.[14,27,29] Additionally, both IR1 and IR2 are able to catalyze SUMO E3 ligase activity when expressed separately or together within IR1-M-IR2.[28,30] SUMO E3 ligases include the SP-RING family that use a RING domain to interact with charged SUMO~E2 ("~" denotes a thioester

bond) and a second family, as exemplified by RanBP2 and ZNF451, that bind SUMO~E2 through SIMs and elements that recognize the E2.[30-33] These E3 ligases stimulate E2 discharge by positioning the charged Ub/Ubl~E2 in a closed conformation primed for conjugation (reviewed in refs. 21, 22).[34-36]

Three SUMO proteins are widely expressed in human cells: SUMO1, SUMO2 and SUMO3, with SUMO2 and SUMO3 sharing ~95% sequence identity.[32,37] RanBP2 exhibits a binding preference for SUMO1 over SUMO2/3 resulting in a more stable complex with SUMO1-RanGAP1/Ubc9 relative to SUMO2/3-RanGAP1/Ubc9, thus leading to preferential protection of the SUMO1-RanGAP1 isopeptide bond from SUMO proteases.[27,38-40] RanBP2 exhibits binding specificity for SUMO1, but cellular substrates of the RanBP2 E3 ligase are typically modified by SUMO2/3[41,42] suggesting that RanBP2 is a receptor for SUMO1-RanGAP1/Ubc9 while retaining E3 ligase activity with SUMO2/3. Several models have been put forward for how RanBP2 functions as an E3 ligase,[17,40,43] but how its structure and interactions with SUMO1-RanGAP1/Ubc9, Crm1 and the Ran GTPase impact its E3 ligase activities remains unclear.

RanGAP1 exists in both unmodified and SUMO-modified forms and shuttles between nucleus and cytoplasm, and while Crm1 is implicated as its exporter, an NES within RanGAP1 has not been identified.[14,44,45] Further, RanBP2 maintains interactions with SUMO1-RanGAP1/Ubc9[43,46] in mitosis and is recruited to kinetochores and spindles by Crm1,[47] interactions that are perturbed by leptomycin B, a molecule that disrupts Crm1-NES interactions.[47,48] To address a basis for these interactions, we employed structural, cellular, and biochemical studies to reconstitute and characterize activities of complexes formed between RanBP2, SUMO1-RanGAP1, Ubc9, Crm1 and the Ran GTPase.

Results

Reconstitution and cryo-EM analysis of RanBP2/SUMO1-RanGAP1/Ubc9/Crm1/Ran(GTP)

Reconstitution of RanBP2/SUMO1-RanGAP1/Ubc9/Crm1/Ran complexes utilized a RanBP2 fragment first characterized in detail by Melchior and colleagues[17,43] that spans residues 2300-3060 and includes the IR1-M-IR2 motifs flanked by two FG repeats and two RBDs, the N-terminal RBD3 and C-terminal RBD4 (RanBP2^{RBD3-4}, Fig. 1A). A GTPase-defective Ran variant Ran^{Q69L} was reported to stabilize interactions between Crm1 and RanBP2.[17] In our reconstitution, Ran^{Q69L}(GTP) co-migrated with RanBP2^{RBD3-4}/SUMO1-RanGAP1/Ubc9/Crm1 but size exclusion chromatography (SEC) revealed a broad peak consistent with polydispersity or conformational heterogeneity, perhaps due to multiple Ran binding sites presented by RanGAP1, the two RBDs, and potentially Crm1 (Figs. 1B-C, S1A). To determine if the two RBDs contributed to this behavior, truncations of RanBP2^{RBD3-4} were generated: RanBP2$^{2300-2910}$ containing only RBD3 and RanBP2$^{2446-3060}$ containing only RBD4 (RanBP2^{RBD3} and RanBP2^{RBD4}, respectively; Fig. 1A-B). RanBP2^{RBD3} exhibited a broad elution profile similar to RanBP2^{RBD3-4}, but RanBP2^{RBD4} eluted later than RanBP2^{RBD3} or RanBP2^{RBD3-4}, with a 100 kDa reduction in apparent molecular weight, much larger than expected for deletion of a 17 kDa RBD domain (Fig. 1C, S1A). As RanBP2^{RBD4} contributed to a more compact architecture, a RanBP2^{RBD4}/SUMO1-RanGAP1/Ubc9 complex was purified, incubated with Crm1 (3-fold molar excess) and Ran^{Q69L}(GTP) (10-fold molar excess), and purified again by gel filtration (Fig. S1B). Prior to vitrification, the sample was mild crosslinked using bis(sulfosuccinimidyl)suberate (BS3) to stabilize complexes (Fig. S1C-E).

Data collection and processing produced ~700k unique particles containing Crm1 from cryo-EM micrographs collected from four grids (see Star Methods; Figs. S1F-M and S2, Table S1). Crm1/Ran^{Q69L}(GTP) was separated from unbound Crm1, resulting in ~535k particles and a reconstruction with an overall resolution of 3.18 Å with densities evident for RanBP2, portions of

RanGAP1 and other diffuse densities emanating from the Crm1 ring. Focused refinement of Crm1/Ran^{Q69L}(GTP) improved the overall resolution to 2.89 Å. 3D classification revealed that the RanGAP1 GAP domain was highly mobile, anchored to Crm1 via an N-terminal helix, and bound to Ran^{Q69L}(GTP) and the RanBP2 RBD4. Further processing resulted in reconstructions using ~290k particles for the RDB4/Ran^{Q69L}(GTP)/RanGAP1^{GAP} subcomplex at an overall resolution of 3.52 Å, with focused refinements of RBD4/Ran^{Q69L}(GTP) at 3.37 Å and the GAP domain at 3.52 Å. The C-terminal domain of RanGAP1, SUMO1 and Ubc9 were resolved after signal subtraction and 3D classification of 74k particles to generate reconstructions from 61k particles for subcomplexes containing RanBP2/Ubc9/SUMO1-RanGAP1^{CTD} or Crm1/Ran^{Q69L}(GTP) at 3.29 Å and 3.10 Å, respectively. As components of the complex exist in multiple conformations (Fig. S2), these reconstructions were combined to generate a composite map for model building and refinement.

Overall architecture

The architecture of the RanBP2^{RBD4}/SUMO1-RanGAP1/Ubc9/Crm1/Ran^{Q69L}(GTP) complex reveals Crm1 and RanBP2 as major organizing factors of the complex (Fig. 2). At the center is Crm1 bound to one molecule of Ran^{Q69L}(GTP) with SUMO1-RanGAP1^{CTD}/Ubc9 and RanGAP1^{GAP}/Ran^{Q69L}(GTP)/RanBP2 RBD4 subcomplexes on the periphery of the Crm1 ring. Crm1 adopts a closed toroidal, cargo-bound conformation similar to that described previously (PDB: 3GJX, 3NBY, 5DIS).[49-52] The RanBP2 FG1-IR1-M-IR2-FG2-RBD4 fragment wraps around the complex with the two FG domains, defined as FG1 and FG2, positioned on opposite sides of the Crm1 ring. The RanBP2 IR1 motif is bound to SUMO1-RanGAP1/Ubc9 and flanked by disordered segments that link it to FG1 and FG2. Following FG2 is another disordered segment that separates FG2 from RBD4. The latter is bound to a molecule of Ran^{Q69L}(GTP) that is in turn bound by the GAP domain of RanGAP1. RanGAP1 includes an N-terminal leucine-rich

repeat (LRR) GAP domain and a C-terminal domain (CTD) that are separated by more than 50 Å and connected by a ~70 residue acidic linker that is not observed in reconstructions.

Crm1 interacts with Ran^{Q69L}(GTP) and the FG repeats of RanBP2

Interactions between Crm1 and Ran^{Q69L}(GTP) in our complex resemble those previously reported and will not be discussed further.[51,53] FG regions of RanBP2^{RBD4} were reported to contribute to Crm1 binding[17] and continuous densities for FG1 residues 2507-2517 and FG2 residues 2841-2881 are observed, respectively (Figs. 3A-B, S3). Residues from FG1 interact with outer helices (A helices) of HEAT (Huntingtin, EF-3, PP2A, TOR1) repeats 14-16 of Crm1, burying ~1280 Å^2 of combined surface area with FG1 residues Val2508, Val2509, Pro2512, Phe2514 and Phe2516 as major contributors to the interface (Fig. 3A). RanBP2 FG2 includes six phenylalanine residues and one tryptophan within residues 2841-2881 that engage Crm1 HEAT repeats 2-7, burying a total surface area of ~3630 Å^2 with Phe2842 coordinated by Crm1 HEAT repeats 2 and 3, Phe2850 and Leu2853 coordinated by Crm1 HEAT repeats 3 and 4, Phe2861 and Phe2863 coordinated by HEAT repeats 4 and 5, and Trp2872 coordinated by Crm1 A and B helices of HEAT repeats 5 and 6 with Phe2870 stacking above Trp2872 (Fig. 3B-D). The last observed aromatic anchor in FG2 is Phe2880 which docks into a pocket formed by Crm1 HEAT repeat 7.

Structures of other proteins containing FG repeats have been determined in complex with Crm1.[51,53,54] FG repeats from human Nup214 (PDB 5DIS)[51] and yeast Nup42p (PDB 5XOJ)[53] also bind within pockets created by Crm1 helices 14-16, although they adopt distinct conformations or polarities relative to each other or to RanBP2 FG1 (Fig. S4A). Of note, Phe114 of Nup42p and Phe1922 of Nup214 dock into the same hydrophobic groove of Crm1 as Phe2514 of RanBP2 FG1 (Fig. S4A). FG repeats from Nup214 continue to wrap around Crm1, binding in several hydrophobic pockets formed by Crm1 HEAT repeats 17-20, some of which are also bound by FG repeats from Nup42p and Yrb2p (yeast RanBP3, PDB 3WYF).[54]

Continuous densities are not observed for RanBP2 past Gly2517, but isolated densities consistent with phenylalanine side chains are observed in pockets formed by HEAT repeats 18 and 19 where Nup214 Phe1947 binds Crm1 (Fig. S4B left panel) and HEAT repeats 17 and 18 where Phe1982 of Nup214, Phe92 of Nup42p, and Phe100 of Yrb2p bind Crm1 (Fig. S4B right panel). Interactions between Crm1 and FG repeats of Nup214 and Yrb2p overlap with RanBP2 FG2 residues 2841-2853 as illustrated by comparing Phe2842 and Phe2850 of RanBP2 with phenylalanine residues of Nup214 and Yrb2p (Fig. S4C). FG2 in our structure, however, continues to wrap around Crm1 HEAT repeats 5-7, a feature not observed in other structures for complexes between FG regions and Crm1. While the SUMO1-RanGAP1/Ubc9 subcomplex is present in only a subset of our particles, FG2 residues Lys2868-Thr2872 are observed in all reconstructions and are within 7-8 Å of the C-terminal helix of RanGAP1.

RanGAP1 forms a complex with Ran^{Q69L}(GTP) and RBD4 of RanBP2

The GAP domain of RanGAP1 is bound to a molecule of Ran^{Q69L}(GTP) that in turn interacts with the C-terminal RBD4 of RanBP2 (Fig. 4A). This subcomplex structure is similar to a crystal structure of the *Schizosaccharomyces pombe* RanGAP1 in complex with human Ran(GMPPNP) and the RBD of RanBP1 (PDB 1K5D).[55] While similar, notable differences include the absence of the N-terminal human RanGAP1 helix which is not conserved in fission yeast, the inactivating Q69L mutation in Ran, and subtle differences in the way RBD4 engages Ran relative to the RBD of RanBP1 which are likely due to differences in primary sequences (~55 % seq identity). Additionally, Arg2975 and Lys2980 of RanBP2 RBD4 penetrate deeper into a Ran interface where their side chain nitrogen atoms contact the carbonyl oxygen atoms of Arg29 and His30 (Fig. 4B), part of the switch I region of Ran which undergoes large conformational changes in response to nucleotide binding and identity. Another notable difference is in the RanGAP1-Ran interface where the ε-amine of Arg93 of human RanGAP1, in addition to forming a salt bridge with Glu46 as also observed in the *S. pombe* structure, contacts

Ala41 of Ran, which is within 4-5 Å from the γ-phosphate of GTP and the coordinating Mg^{2+} ion (Fig. 4C). Additional hydrogen bonding interactions present in our complex but not observed in the *S. pombe* RanGAP1-Ran complex involve Asp273 of RanGAP1, which forms a hydrogen bonding network with Ser135 and Arg95 of Ran (Fig. 4D).

Based on the *S. pombe* RanGAP1-Ran-RanBP1 structure, it was proposed that in the absence of a classical catalytic Arg finger, RanGAP1 activates Ran for GTP hydrolysis by stabilizing the switch II loop of Ran, thereby properly orienting the catalytic glutamine residue within Ran.[55,56] Our structure confirms this model and expands upon it via comparison to the currently available structures for human Ran(GMPPNP) bound to RBD1, RBD2, RBD3, and RBD4 domains of RanBP2 in the absence of RanGAP1.[11,57] Inspection of the Ran switch II loop in these structures shows that it adopts conformations that would clash with RanGAP1 in our human complex and in *S. pombe* structures (Fig. 4E-G). For instance, when superimposing the RanBP2 RBD4-Ran(GMPPNP) structure onto our structure,[11] we observe that Ran Phe72 is 14 Å away from Phe72 of Ran of our structure and, along with Lys71, Glu70, Gly74, and the catalytic Gln69 would clash with the main chain and side chain atoms of RanGAP1 (Fig. 4F-G). Thus, as has been reported previously, RanGAP1 stabilizes the switch II loop of Ran[55,56] but we further note that it does so by restricting conformational flexibility of the switch II loop, which in turn orients the catalytic glutamine and neighboring switch II residues to catalyze GTP hydrolysis in the absence of a catalytic Arg finger.

RanGAP1 contacts Crm1 via two distinct interfaces

The N-terminal RanGAP1 GAP domain is tethered to Crm1 by its N-terminal helix, which occupies the hydrophobic Crm1 NES-binding pocket between the A helices from HEAT repeats 11 and 12 (Figs. 5A-D, S3 panel 10) and overlaps with Crm1-bound NES motifs from protein kinase inhibitor (PKI) and Snurportin (Spn1; S4D).[51,53] The RanGAP1 N-terminal helix is conserved in vertebrate and invertebrate species, although this is less clear for insects (Fig.

5E). These N-terminal residues are missing or not conserved in organisms such as *S. cerevisiae*, *S. pombe* and *A. thaliana* (Fig. 5E).

Unlike the N-terminal GAP domain, which is observed in most particles, the C-terminal domain of RanGAP1 is observed in only 14% of particles suggesting high mobility within this complex (Fig. S2). Despite this mobility, reconstructions show that the C-terminal RanGAP1 domain is conjugated to SUMO1 via Lys524 and bound to Ubc9 with Ubc9 and SUMO1 coordinated by the RanBP2 IR1 module (Fig. S3 panels 2 and 3). The structure of the SUMO1-RanGAP1/Ubc9/RanBP2 IR1 subcomplex shares overall similarities to a crystal structure of human SUMO1-RanGAP1^{CTD}/Ubc9/RanBP2^{IR1-M} (PDB 1Z5S, RMSD = 0.897).[27] In addition, a new interface is observed between Crm1 and the SUMO1-RanGAP1^{CTD}/Ubc9/RanBP2^{IR1} subcomplex consisting of the two C-terminal RanGAP1 helices (residues 557-585) and Crm1 HEAT repeats 5-7, with additional contributions from Ubc9, interactions that bury approximately 1960 Å^2 of combined surface area (not including the RanGAP1-Ubc9 interface; Fig. 5F-H). A substantial portion of the RanGAP1/Crm1 interface consists of interactions between residues from Crm1 HEAT repeats 6 and 7 and a pocket formed by RanGAP1 residues Tyr585, Leu581, Gln582, His578, and Phe575, where a network of hydrophobic and electrostatic contacts are established (Fig. 5G). Another notable interaction involves insertion of Lys245 of Crm1 into the RanGAP1/Ubc9 interface which involves several hydrogen bonding and hydrophobic contacts (Fig. 5H). This interface does not appear to contribute to specific recognition of SUMO1 as no contacts are observed between Crm1 and SUMO1.

As contacts between Crm1 and the N-terminal helix of the RanGAP1 GAP domain and the SUMO1-RanGAP1/Ubc9 subcomplex were unexpected, we sought to confirm if any of these interactions could be recapitulated by AlphaFold multimer (version 2.2) which was released after our structures were determined.[58] Indeed, even in the absence of RanBP2 and Ran(GTP), AlphaFold predicts interactions between Crm1 and the N-terminal helix of the GAP domain in 17 of 25 predictions (Fig. S4E). Perhaps more surprising given that it was only present in 14% of

our particles, it also predicts a similar interface between Crm1 and the C-terminal domain of RanGAP1 in 24 of 25 predictions (Fig. S4E).

The N-terminal helix of RanGAP1 is a nuclear export signal

Prior studies in yeast and human cells showed that RanGAP1 shuttles between the nucleus and cytoplasm.[14,44,45,59] In addition, localization of human RanGAP1 is perturbed by leptomycin B (LMB) suggesting a dependency on Crm1 for export.[44] Our structures reveal that the N-terminal helix of RanGAP1 occupies the hydrophobic Crm1 NES-binding pocket (Figs. 5B-D, S3 panel 10, S4D)[51,53] suggesting that it may function as an NES for human RanGAP1. The RanGAP1 N-terminal helix projects Ile6, Leu9, Leu13, Thr16, and Val18 into Crm1 which can be aligned to the $x\text{-}\varphi^0\text{-}x_2\text{-}\varphi^1\text{-}x_3\text{-}\varphi^2\text{-}x_2\text{-}\varphi^3\text{-}x\text{-}\varphi^4$ NES motif described for PKI-type NES signals, where x is any residue and φ is hydrophobic (Fig. 5B-D).[50] One exception is Thr16 at φ^3, a position typically occupied by Phe or Leu in prototypical NES motifs. In addition, hydrogen bonding interactions are evident between the Crm1 Lys568 ε-amino group and the backbone carbonyls of Ala14 and Thr16 of RanGAP1 (Fig. 5C).

To determine if the N-terminal 18 amino acids of RanGAP1 are sufficient for nuclear export, human hTERT-RPE1 cell lines were generated that stably express monomeric EGFP fused to wild type N-terminal residues of RanGAP1 or a mutant sequence where four of the key NES motif hydrophobic residues (Ile6, Leu9, Leu13, and Thr16) are replaced by alanine (4A mutant) (Fig. 6A). While $RanGAP^{1\text{-}18\text{-}WT}$-mEGFP was predominantly cytoplasmic, $RanGAP^{1\text{-}18\text{-}4AMUT}$ was observed in the nucleus and cytoplasm, suggesting that the N-terminal residues of RanGAP1 can induce nuclear export when fused to EGFP and that residues Ile6, Leu9, Leu13, and Thr16 of RanGAP1 contribute to export (Fig. 6A).

To assess if the N-terminal helix of endogenous RanGAP1 functions as an NES in cells, CRISPR-Cas9 was used to delete residues 5-17 of RanGAP1 in hTERT-RPE1 cells (Fig. 6B). Isolated clones homozygous for the Δ5-17 deletion express a RanGAP1 variant where 4 of the 5

key hydrophobic residues of the putative RanGAP1 NES motif are deleted (ΔNES; Fig. 6C). Western blot analysis of lysates obtained from these clones showed similar basal levels of unmodified and SUMO1-modified RanGAP1 in two of the three isolated clones and that RanGAP1 in those clones is phosphorylated after nocodazole arrest,[60] suggesting that removal of the NES does not perturb known post-translational modifications of RanGAP1 (Fig. 6C-D). Characterization of clone 3 was not pursued further due to the lower levels of RanGAP1 observed in this clone (Fig. 6C). Confocal microscopy of fixed cells using an α-RanGAP1 antibody confirmed that cells expressing RanGAP1$^{\Delta NES}$ exhibit staining of the nuclear rim similar to cells with wild type RanGAP1 (Fig. 6E). However, quantification of nuclear to cytoplasmic ratios (N/C) for RanGAP1 in wild type RPE1 and RanGAP1$^{\Delta NES}$ cells revealed that RanGAP1$^{\Delta NES}$ exhibits higher N/C ratios compared to wild type RanGAP1 suggesting an export defect for RanGAP1$^{\Delta NES}$ (Fig. 6F). Treatment of cells with LMB resulted in higher N/C ratios for RanGAP1 in wild type RPE1 cells consistent with Crm1 mediating nuclear export of RanGAP1 and similar to the basal N/C ratios seen in RanGAP1$^{\Delta NES}$ cells. In contrast, LMB treatment of cells expressing RanGAP1$^{\Delta NES}$ resulted in a comparatively smaller increase in N/C ratios. These results are consistent with the N-terminal helix of RanGAP1 functioning as a Crm1-dependent NES in cells.

Nuclear localization of Ran in cells expressing RanGAP1$^{\Delta NES}$

Cells were next analyzed for localization of the Ran GTPase because RanGAP1 is the primary activator of the Ran GTPase in human cells and because RanGAP1$^{\Delta NES}$ is retained in the nucleus. While total levels of Ran remained unaffected (Fig. 6G), immunostaining using a Ran-specific antibody showed that Ran is redistributed from the nucleus to the cytoplasm in cells expressing RanGAP1$^{\Delta NES}$ compared to cells expressing wild type RanGAP1 (Fig. 6H, compare N/C ratios for WT vs Δ2 vs Δ10 in the absence of LMB). Treating wild type cells with LMB redistributed Ran from the nucleus to the cytoplasm, shifting N/C ratios close to those

observed for cells expressing RanGAP1$^{\Delta NES}$ in the absence of LMB (Fig. 6H). By comparison, treating cells expressing RanGAP1$^{\Delta NES}$ with leptomycin B altered N/C ratios only slightly (Fig. 6H). These results suggest that nuclear retention of RanGAP1$^{\Delta NES}$ may contribute to mislocalization of Ran in these cells.

A Ran GTP-GDP gradient, where GTP-bound Ran is nuclear and GDP-bound Ran is cytoplasmic, is required for normal active nucleocytoplasmic transport (NCT).[6] While immunofluorescence experiments conducted here cannot distinguish between GTP and GDP-bound Ran, we posited that mislocalization of Ran might result in perturbations in NCT. To test this, we generated stable RPE1 cell lines in wild type and RanGAP1$^{\Delta NES}$ backgrounds that express fluorescent reporters tagged with constitutive or optogenetically-inducible NES and NLS signals to quantify steady-state NCT as well as transport kinetics, respectively (Fig. S5).[61-63] Confocal microscopy with live cells showed no transport defects either at steady-state (Fig. S5A-E) or with respect to the kinetics of export (Fig. S5F-I) or import (Fig. S5J-M) using these engineered reporter systems.

Mitotic defects are not evident for cells expressing RanGAP1$^{\Delta NES}$

The RanBP2/SUMO1-RanGAP1/Ubc9 complex remains intact during mitosis after NPC disassembly and is recruited to kinetochores and mitotic spindles in a Crm1-dependent manner where the complex is thought to mediate mitotic functions involving stabilization of microtubule-kinetochore interactions as well as SUMO conjugation of topoisomerase IIα, Aurora B kinase, and other substrates.[41-43,46,47,64-67] Further, addition of LMB to asynchronous cells inhibits mitotic recruitment of RanBP2/SUMO1-RanGAP1/Ubc9 suggesting involvement of the Crm1 NES binding site in this process.[47] Given that RanGAP1 contains an NES, we speculated that interactions between the RanGAP1 NES and Crm1 may contribute to RanBP2/SUMO1-RanGAP1/Ubc9 recruitment by Crm1. Cells expressing RanGAP1$^{\Delta NES}$ were analyzed for differences in co-localization or defects in mitosis. However, RanGAP1$^{\Delta NES}$ co-localized with

Crm1 in metaphase and anaphase in a manner similar to wild type RanGAP1 (Fig. S6A). Differences in mitotic localization of Ran were also not observed in cells expressing RanGAP1$^{\Delta NES}$ compared to WT RanGAP1 (Fig. S6B). Finally, cell cycle distributions of asynchronous cells expressing wild type or RanGAP1$^{\Delta NES}$ cells failed to uncover significant differences in any cell cycle phase (Fig. S6C-D). These results suggest that interactions between the RanGAP1 NES and Crm1 are dispensable for growth under the conditions tested and that the RanGAP1 NES is not required for Crm1-dependent recruitment of the RanBP2/SUMO1-RanGAP1/Ubc9 complex in mitosis. It is also noteworthy that SUMO1 conjugation to RanGAP1 is not essential for viability or mitotic progression in several human cell lines,[68] suggesting that SUMO1 modification of RanGAP1 and the NES might act redundantly with respect to interactions with RanBP2 and Crm1.

Ran GTPase activity, the RanGAP1 NES and Crm1-Ran-cargo turnover

Prior work from the Melchior group showed that the RanBP2/SUMO1-RanGAP1/Ubc9 complex was able to stimulate Crm1-cargo release in the presence of wild type Ran(GTP) or limiting amounts of Ran^{Q69L}(GTP).[17] With respect to this activity, we wondered if the RanGAP1 NES motif might also play a role in Ran(GTP) turnover and disassembly of Crm1/Ran(GTP)/cargo complexes by directly competing with cargo NES motifs for Crm1 binding. To determine if the RanGAP1 NES contributes to Ran GTPase cycling and cargo disassembly in the context of the Crm1/RanBP2/SUMO1-RanGAP1/Ubc9 complex, real-time GTPase assays were performed assuming that GTP hydrolysis rates might reflect iterative rounds of assembly and disassembly of Crm1/Ran(GTP)/cargo complexes. These assays were conducted at steady state in the presence of the GEF Rcc1 to exchange GDP for GTP in Ran and to allow for continuous GTPase cycling during the time course. Assays included RanBP2 complexed with either SUMO1-RanGAP1/Ubc9 or SUMO1-RanGAP1$^{\Delta N18}$/Ubc9 in the absence and presence of Snurportin (Spn1) as additional NES cargo for Crm1.[17,69]

Rates of GTP hydrolysis for wild type SUMO1-RanGAP1 and SUMO1-RanGAP1$^{\Delta N18}$ complexes in the absence or presence of Crm1 were similar (Fig. S6E). Addition of the NES cargo Spn1 decreased GTPase rates suggesting that cargo dissociation became rate limiting or that this complex inhibited the RBDs ability to extract Ran(GTP) from Crm1. While rates decreased, no significant differences were observed for either K_m or V_{max} for GTP hydrolysis for complexes containing wild type SUMO1-RanGAP1 or SUMO1-RanGAP1$^{\Delta N18}$ across a range of Ran concentrations (Fig. S6E). As such, we confirm prior observations that the rate-limiting step for cargo disassembly is extraction of Ran(GTP) from Crm1 by the RBDs of RanBP2[17] and that competition between RanGAP1 and Spn1 for the Crm1 NES binding pocket does not contribute to cargo assembly/disassembly under the conditions tested. It remains possible that the RanGAP1 NES might compete with cargo NES motifs that are weaker relative to Spn1.[69]

E3 ligase activity depends on IR1 and is modulated by Ran, Crm1 and the RanGAP1 NES

RanBP2 IR1-M-IR2 and isolated IR1 and IR2 motifs bind SUMO and Ubc9 to catalyze E3 SUMO ligase activity in vitro, with IR1 exhibiting greater activity.[27,30,40,43] While IR1 and IR2 can each bind SUMO1-RanGAP1/Ubc9, IR1 was proposed as the preferred binding site due to its higher affinity for SUMO and Ubc9.[27,40,43] This creates an apparent paradox: are these motifs receptors for SUMO1-RanGAP1/Ubc9, E3 ligases for activated SUMO~Ubc9 thioesters, or can these motifs accommodate both? One model for how the two IR modules cooperate in the context of larger RanBP2 fragments suggests that IR1 is the principal E3 ligase in the absence of SUMO1-RanGAP1/Ubc9 and that IR2 catalyzes E3 ligase activity when SUMO1-RanGAP1/Ubc9 binds and occludes IR1.[43] Our structure reveals that SUMO1-RanGAP1/Ubc9 associates with the RanBP2 IR1 motif in the context of a larger RanBP2 fragment (Fig. 7A). Further, EM densities are not apparent for IR2, suggesting high mobility, an observation consistent with the model that it binds charged SUMO~E2 for conjugation to substrates.

To test if IR1 and IR2 are required for E3 ligase activity in intact RanBP2/SUMO1-RanGAP1/Ubc9/Crm1/Ran complexes we performed SUMO2 conjugation assays with wild type RanBP2^{RBD3-4} or variants containing deletions of motifs I and II in IR1 or IR2, which are required for E3 ligase activity.[27] Borealin is a component of the chromosome passenger complex (CPC) and an endogenous substrate of RanBP2 that is preferentially modified by SUMO2/3 during mitosis.[41] We reconstituted a subcomplex of the CPC with Borealin, Survivin and a fragment of Incenp$^{1-58}$ for use in SUMO conjugation assays (Fig. 7B).[43] To determine if the Ran GTPase cycle modulates RanBP2 E3 ligase activity, SUMO conjugation assays were performed under multiple turnover conditions in the presence of Rcc1 and either Ran(GTP), Ran^{Q69L}(GTP) in which GTP cannot be hydrolyzed, Ran(GDP), or with no Ran present (Figs. 7C-E, S7). Complexes containing wild type RanBP2^{RBD3-4} catalyzed SUMO2 conjugation to Borealin whereas deletion of IR1 motifs I and II resulted in a loss of Borealin modification by SUMO2 (Fig. 7D-E). In comparison, deletion of IR2 motifs I and II resulted in conjugation activity comparable to wild-type RanBP2^{RBD3-4}. These results suggest that IR1 functions as the dominant SUMO E3 ligase under these conditions. Addition of Ran(GDP) had little impact on SUMO2 modification of Borealin, but conjugation was impaired when Ran(GTP) was added under conditions where Rcc1 promoted GDP/GTP exchange (Fig. 7D-E, S7B). To further determine if Ran(GTP) cycling affects SUMO conjugation activity, Ran^{Q69L}(GTP) was added resulting in a substantial loss of conjugation activity suggesting that locking Ran in the GTP-bound conformation severely impairs the E3 ligase activity of the complex (Fig. 7D-E).

Ran^{Q69L}(GTP) inhibited conjugation in these assays, so we next explored if this was dependent on the RanGAP1 NES as this interaction is Crm1 and Ran^{Q69L}(GTP)-dependent. Crm1 was titrated into reactions in the presence of excess Ran^{Q69L}(GTP) and RanBP2/SUMO1-RanGAP1/Ubc9 complexes containing either wild type SUMO1-RanGAP1 or SUMO1-RanGAP1$^{\Delta N18}$. Increasing Crm1 concentrations diminished SUMO conjugation activity in the presence of wild type SUMO1-RanGAP1 but no effect was observed for complexes containing

SUMO1-RanGAP1$^{\Delta N18}$ that lack the NES (Fig. 7F-G). The inhibitory effect of adding Crm1 in the presence of Ran^{Q69L}(GTP) was not evident when using Ran(GTP) in the presence of GAP and GEF effectors (Fig. S7A), although the presence of Ran(GTP) resulted in some inhibition of ligase activity when Crm1 was present (Fig. 7D-E and Fig. S7B). Crm1-dependent inhibition of ligase activity in the presence of Ran^{Q69L}(GTP) suggests that our structure of RanBP2/SUMO1-RanGAP1/Ubc9/Crm1/Ran^{Q69L}(GTP) represents an inhibited conformation for the RanBP2 E3 ligase perhaps because IR1 is less able to dissociate from SUMO1-RanGAP1/Ubc9 to accommodate charged SUMO~E2 when the NES of RanGAP1 is stably bound to Crm1/Ran^{Q69L}(GTP).

Discussion

The RanBP2/SUMO1-RanGAP1/Ubc9 complex is found at the cytoplasmic face of the NPC in interphase cells where it plays critical roles in nucleocytoplasmic trafficking.[10,12,16,17] In mitotic cells, RanBP2/SUMO1-RanGAP1/Ubc9 remains intact and is recruited to kinetochores and spindles in a Crm1-dependent manner where it plays roles in the fidelity and progression of mitosis.[42,46,47,64,66,67] Importantly, RanBP2/SUMO1-RanGAP1/Ubc9 functions as a SUMO E3 ligase targeting several substrates including a number of mitotic and interphase targets.[41,42,66,70-72] Here, we capture a structure of a RanBP2 fragment that includes its SUMO E3 ligase motifs, two FG-binding regions, and the last Ran-binding domain in complex with SUMO1-RanGAP1/Ubc9, Crm1, and Ran^{Q69L}(GTP). Reconstructions and models for this complex reveal interactions that were not anticipated, namely identification of a RanGAP1 NES and interactions between SUMO1-RanGAP1/Ubc9 and Crm1. Our structures, combined with other recent human structures[11,57], enabled comparative analysis of interactions between the GAP domain of RanGAP1 and the switch II region of Ran, a region critical for Ran GTPase activity in the absence of a classical Arg finger. Finally, our description of the interactions between two RanBP2 FG regions, FG1 and FG2, and Crm1 expand our understanding of how karyopherins

such as Crm1 navigate the FG mesh of the NPC, while confirming several previous models of Crm1 FG binding.[51,53,54]

Prior work in yeast and human cells has shown that RanGAP1 shuttles between the nucleus and cytoplasm and that human RanGAP1 accumulates in the nucleus upon treatment with LMB, suggesting Crm1-dependent export.[14,44,45] We identify the NES of RanGAP1 that contributes to its Crm1-dependent cellular localization. Mislocalization of RanGAP1 in the nucleus is correlated with mislocalization of Ran, but we were unable to observe defects in NCT for several model proteins carrying classical NLS and NES signals. Further work is required to determine if mislocalization of Ran or RanGAP1 contributes to NCT defects and/or differential gene expression by limiting or enhancing import and export of relevant factors, whether protein or RNA. Additionally, RanGAP1 itself may impact nuclear processes such as heterochromatin assembly and gene expression, as has been shown in *S. pombe*,[73] suggesting that mislocalization of RanGAP1 has the potential to perturb gene expression.

We observe that the IR1 SUMO E3 module of RanBP2 is bound to SUMO1-RanGAP1/Ubc9 whereas density for the IR2 module is not observed, a finding consistent with prior studies showing that IR1 forms a more stable complex and is the preferred binding partner for SUMO1-RanGAP1/Ubc9.[27,40,43] Our SUMO conjugation assays show that IR1 is required and that IR2 is dispensable for SUMO2 modification of Borealin, at least in the context of the RanBP2/SUMO1-RanGAP1/Ubc9/Crm1/Ran complex. It remains possible that IR2 may function as an E3 ligase under other conditions or for different SUMO substrates as previously put forward by Melchior and colleagues where IR2 becomes the active SUMO E3 ligase in the context of the IR1-bound RanBP2/SUMO1-RanGAP1/Ubc9 complex.[43] That Ran^{Q69L}(GTP) inhibits SUMO E3 ligase activity in the presence of Crm1 in a RanGAP1 NES-dependent manner leads us to speculate that interactions between RanBP2 IR1 and SUMO1-RanGAP1/Ubc9 can be affected by Ran(GTP) and Crm1 binding, and that in the presence of these factors, the IR1 module becomes less accessible for charged SUMO2~E2. This latter

point may have implications for RanBP2 E3 ligase activity while it is engaged at the NPC during active transport relative to its activities during mitosis.

Limitations of the study

Our studies advance an understanding of interactions within a RanBP2/SUMO1-RanGAP1/Ubc9/Crm1/Ran^{Q69L}(GTP) complex where Ran^{Q69L}(GTP) was used to lock it into one of its many possible functional states. Further analysis and structures of this complex with wild type cycling Ran, Crm1-Ran-cargo, and SUMO conjugation targets such as Borealin would be necessary to better understand conformational changes and activities associated with this complex. Structures of complexes with SUMO1-RanGAP1$^{\Delta NES}$/Ubc9 or with additional charged SUMO~E2 would also be informative with regards to how the NES-Crm1 interactions affect cargo disassembly and E3 ligase activities. Confocal microscopy in human RPE1 cell lines showed that deletion of the RanGAP1 NES alters Ran and RanGAP1 localization but these studies are limited to RPE1 cells where overt defects in mitosis or nucleocytoplasmic transport of model substrates were not detected. Our studies do not address phenotypes in other cell lines or organisms, which may be more sensitive to mislocalization of these components, especially under stress conditions. SUMO modification assays described here suggest that the IR1 module is required for SUMO E3 ligase activity and that IR2 is dispensable for SUMO modification of Borealin. It is possible that IR2 contributes to SUMO modification with substrates other than Borealin or in the absence of Crm1. Finally, while RanGAP1^{NES}-Crm1 interactions stabilize the complex in vitro and contribute to reduction of SUMO ligase activity in the presence of Ran^{Q69L}(GTP), it is unclear what effect, if any, these interactions would have in vivo in the presence of wild type Ran.

Acknowledgements

We thank members of the Lima lab for advice and Jason De La Cruz of the MSK Richard Rifkind Center for Cryo-EM funded in part by the NCI Cancer Center Support Grant (CCSG, P30 CA008748) for assistance during cryo-EM data collection. This research was supported in part by an NIH Grant R35 GM118080 (C.D.L.). The content is solely the responsibility of the authors and does not represent the official views of the National Institutes of Health. C.D.L. is an investigator of the Howard Hughes Medical Institute.

Authors Contributions

V.B., M.A.D., and C.D.L. designed experiments. M.A.D. and C.D.L. designed substrates for structural work. M.A.D. collected cryo-EM data and M.A.D. and C.D.L. determined structures. V.B. generated cell lines and performed cell assays and biochemical experiments. V.B. and C.D.L. wrote the initial draft and edited the manuscript.

Declaration of interests

The authors declare no competing financial interests.

Main figure titles and legends

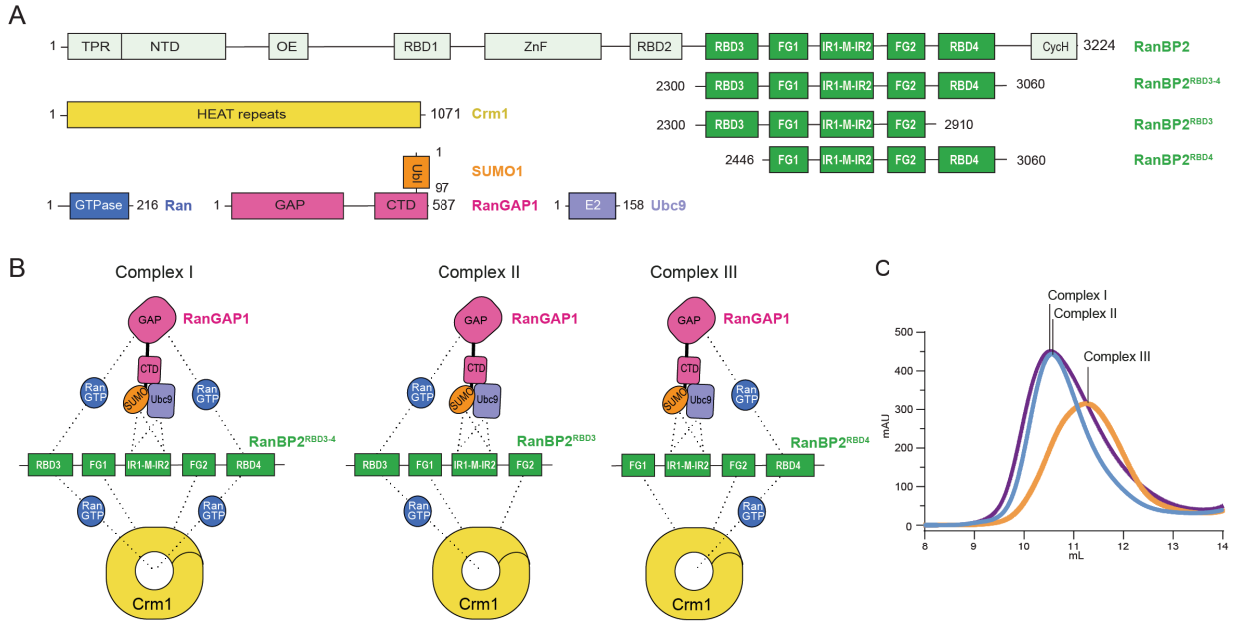

Figure 1 – Reconstitution of RanBP2/SUMO1-RanGAP1/Ubc9/Crm1/Ran^{Q69L}(GTP) complexes.

A Components and domain organization: full length RanBP2 and fragments, Crm1, Ran GTPase, RanGAP1 conjugated to SUMO1, and the E2 Ubc9. RBD, FG, and IR domains indicated within RanBP2.

B Schematic indicating multivalent protein-protein interactions in complexes assembled with RanBP2 variants containing RBD3 and RBD4 (Complex I), RBD3 (Complex II), or RBD4 (Complex III). Dashed lines indicate possible interactions.

C Profiles obtained by size exclusion chromatography for complexes I, II and III shown in B. See Fig. S1 for SDS-PAGE gels and fractions.

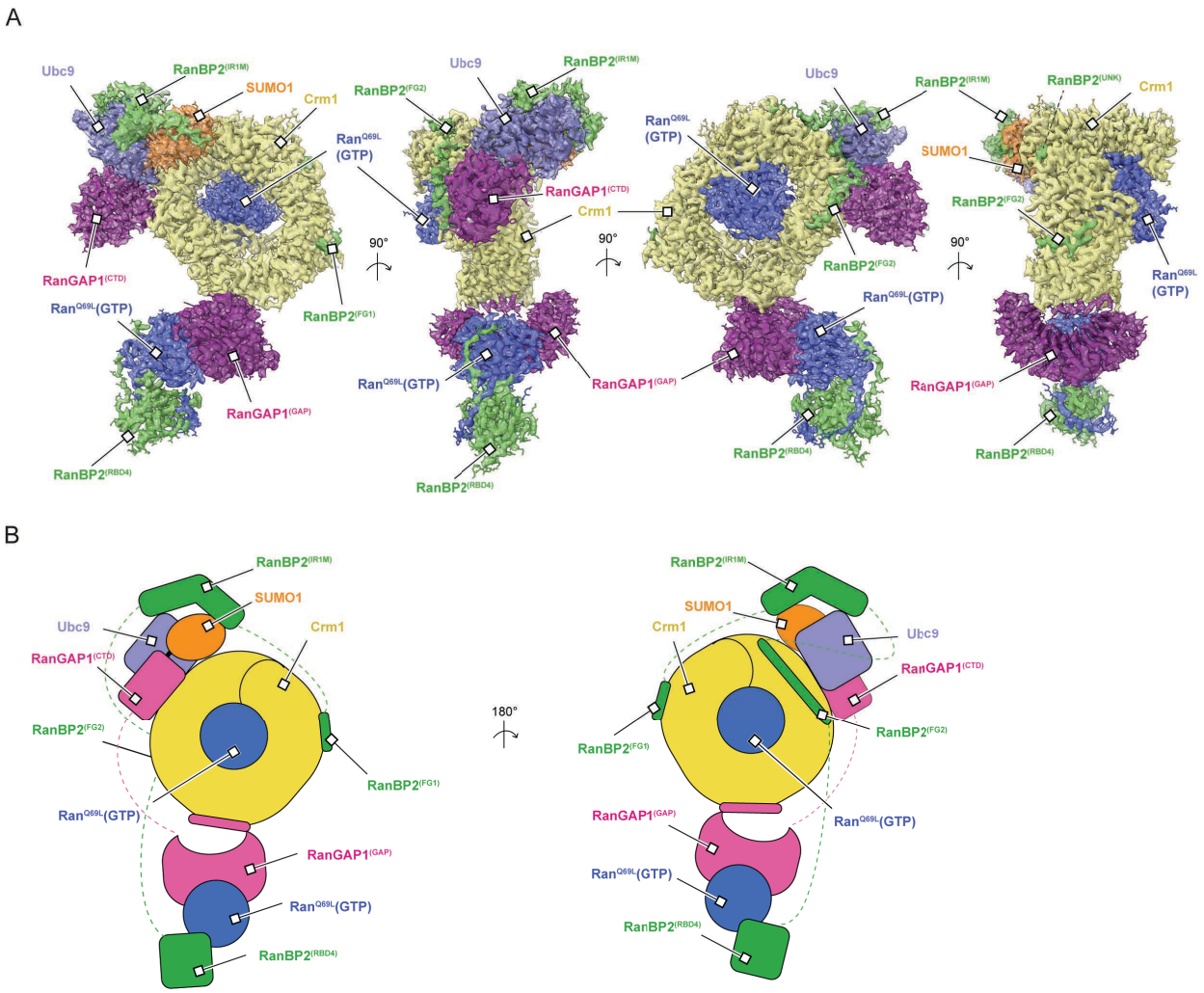

Figure 2 – Cryo-EM structures of RanBP2^{RBD4}/SUMO1-RanGAP1/Ubc9/Crm1/Ran^{Q69L}(GTP).

A Orthogonal views of the composite map and models. EM density (contoured at level 9) and atomic model overlaid and components individually colored and labelled as indicated. RanBP2$^{(UNK)}$ indicates unassigned density likely belonging to RanBP2 as discussed in the text.

B Cartoon representation of the complex. Dashed lines indicate disordered regions colored as in panel A.

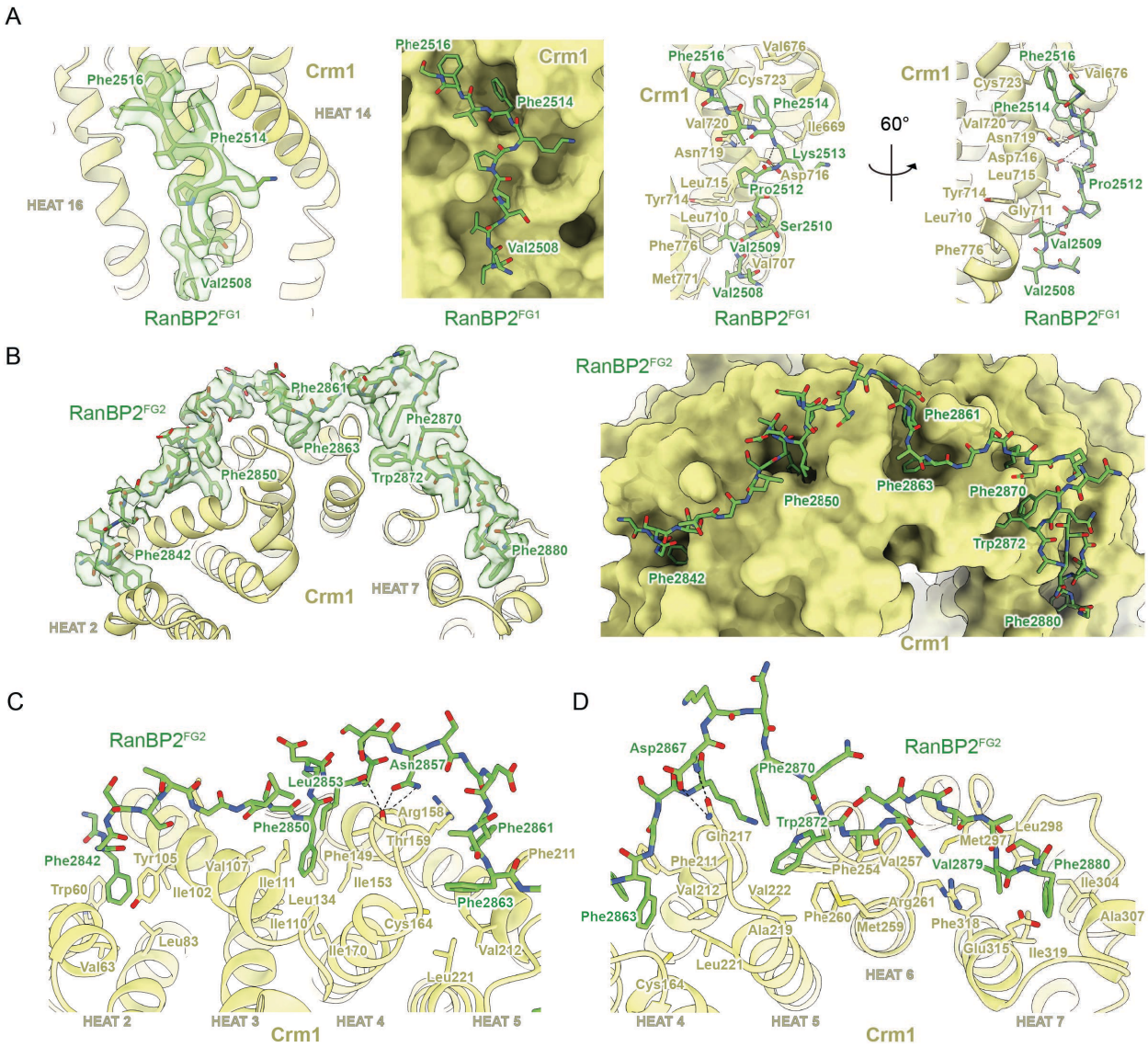

Figure 3 – FG1 and FG2 repeats of RanBP2 bound to Crm1.

A EM density for RanBP2 FG1 (contoured at level 6) overlaid with model to highlight interactions with Crm1 HEAT repeats 14-16, depicted in cartoon representation (left panel); FG1 residues in stick representation and Crm1 as surface representation to emphasize deep pockets on its surface (second panel); the FG1-Crm1 interface with side chains and potential hydrogen bonds shown (dashed lines, third and fourth panels).

B EM density (contoured at level 5.5) and RanBP2 FG2 residues highlighting interactions with Crm1 HEAT repeats 2-7, depicted in cartoon representation (left panel). Similar view of

FG2 model with Crm1 depicted as surface representation to emphasize deep pockets on its surface (right panel).

C FG2 (stick representation) interactions with Crm1 HEAT repeats 2-5 (cartoon and stick representation for side chains) with potential hydrogen bonds depicted as dashed lines.

D Detailed view of the interface between FG2 and Crm1 HEAT repeats 4-7 depicted as in panel C.

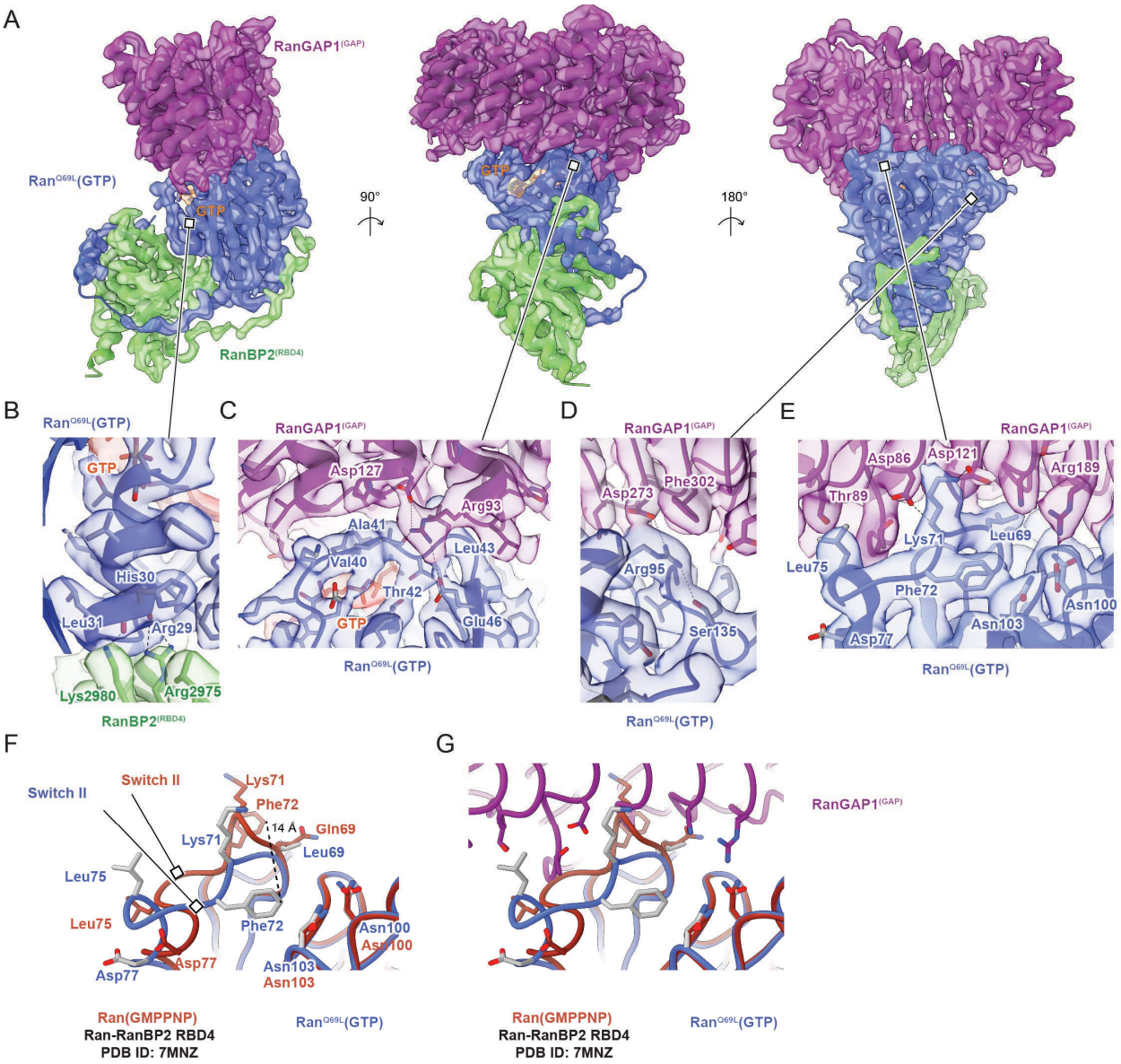

Figure 4 – RanGAP1^{GAP}/Ran^{Q69L}/RanBP2^{RBD4} subcomplex structure.

A Orthogonal views with EM density (contoured at level 9) overlaid with cartoon representation. Proteins are labeled and colored as in Fig 2, GTP EM density colored red, lines pointing to magnified views in panels B-E.

B Magnified view of interactions between RanBP2^{RBD4} Arg2975 and Lys2980 and the switch I helix of Ran^{Q69L}. EM density (contoured at level 9.2) overlaid on cartoon model with residues in stick representation and potential hydrogen bonds indicated as dashed lines.

C Magnified view of interactions of Arg93 of the GAP domain and its proximity to the γ-phosphate of GTP and Ala41 and Glu46 of the switch I region of Ran^{Q69L}. EM density (contoured at level 8), model representation as in (B).

D Magnified view of interactions between Ran^{Q69L} Ser135, Arg95 and RanGAP1 Asp273, Phe302. EM density (contoured at level 8), model representation as in (B).

E Magnified view of the switch II loop of Ran^{Q69L} and the RanGAP1 GAP domain. EM density (contoured at level 9.2), model representation as in (B).

F Overlay of Ran models from the Ran(GMPPNP)-$RanBP2^{RBD4}$ complex (dark orange; PDB 7MNZ)[11] and Ran^{Q69L}(GTP) from our $RanGAP1^{GAP}$-Ran^{Q69L}(GTP)-$RanBP2^{RBD4}$ complex (coloring as in A-E) to highlight conformational differences in switch II loops, including the 14 Å movement of Phe72 (dashed line; same view as in (E)).

G Overlay of Ran models as in (F) but including the GAP domain of RanGAP1 to highlight potential clashes between its surfaces and the switch II loop of Ran from 7MNZ.

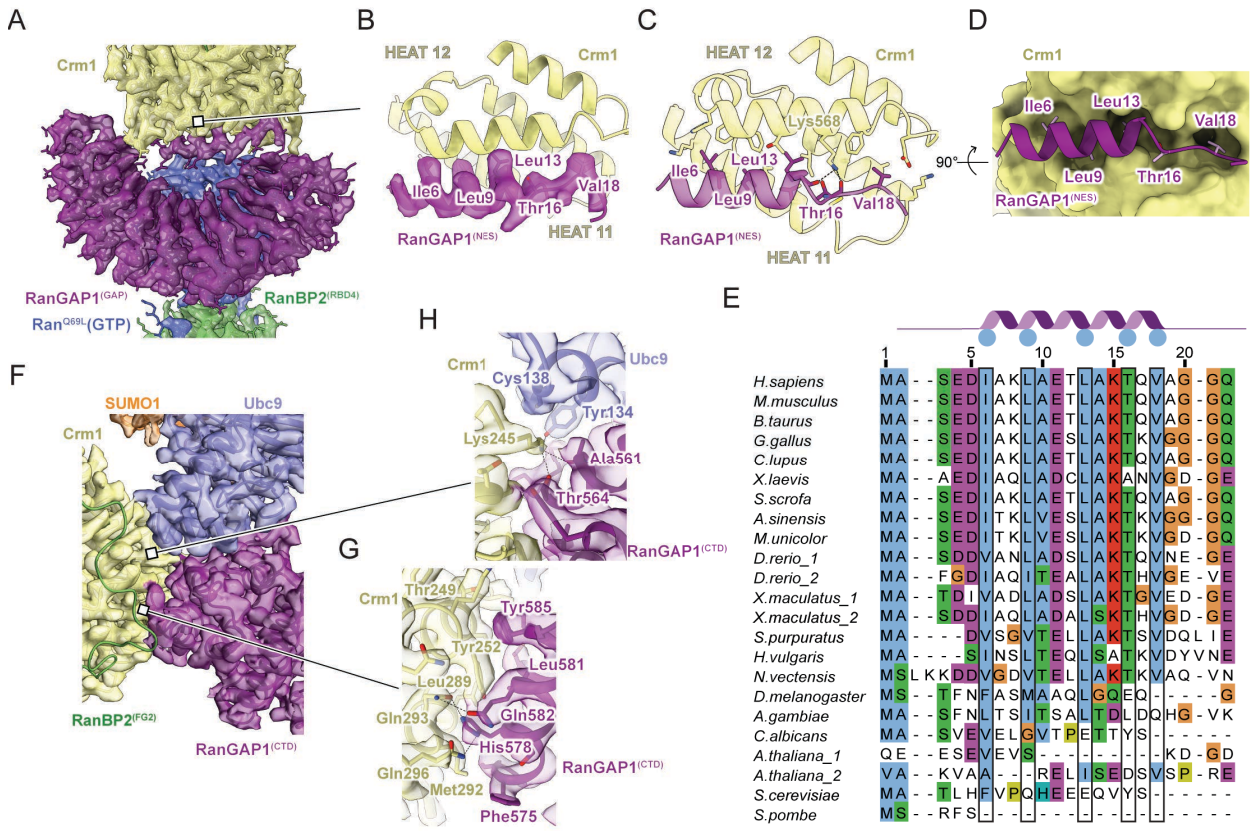

Figure 5 – RanGAP1 interacts with Crm1 via its GAP and CTD domains.

A The N-terminal helix of RanGAP1 interacts with Crm1. Coloring, EM density (contoured at level 9) and model representation as in Fig 2 (rightmost panel). Line points to magnified view in (B).

B Magnified view of (A) to highlight EM density (contoured at level 8) for key residues of the RanGAP1 NES that dock into the Crm1 pocket formed by helices from HEAT repeats 11 and 12.

C Same view as in (B) but showing side chain contacts and potential hydrogen bonds between the RanGAP1$^{(NES)}$ and Crm1 surface.

D Similar view as in (C) depicting the RanGAP1$^{(NES)}$ in cartoon representation and a surface representation of Crm1 to highlight the NES binding pocket.

E Multiple sequence alignment of RanGAP1 N-termini across 20 indicated species. Blue circles in cartoon above the alignment and boxes indicate position of residues within the NES motif. Numbering shown for *H. sapiens* RanGAP1.

F Magnified views of the Crm1/RanGAP1^{CTD}/Ubc9 interface shown in the same orientation as in Fig. 2A (third panel from the left). EM density (contoured at level 10) overlaid with cartoon representation for Crm1, Ubc9, RanGAP1^{CTD} and SUMO1. EM densities omitted for RanBP2^{FG2} to enable visualization of the interface. Lines pointing to magnified view in (G) and (H).

G Magnified view of (F) highlighting interactions between the C-terminal helices of RanGAP1^{CTD} and Crm1. EM density (contoured to level 14) and model representations as in (C) with potential hydrogen bonds as dashed lines.

H Magnified view of (F) highlighting Crm1 interactions and Lys245 in the interface between RanGAP1^{CTD} and Ubc9. EM density (contoured to level 12) with models represented as in (G).

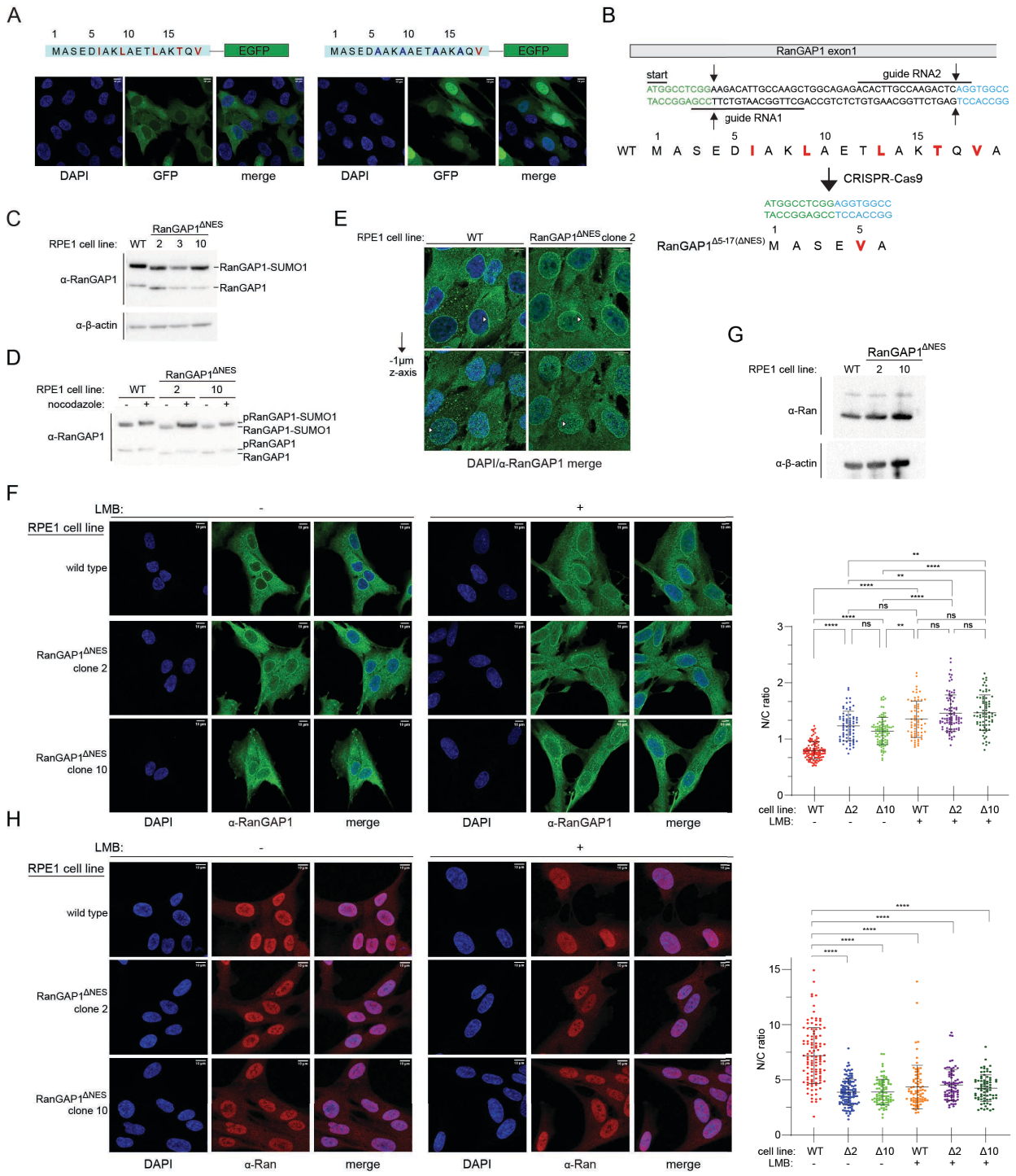

Figure 6 – The N-terminal helix of RanGAP1 encodes a nuclear export signal.

A Schematics for the N-terminal fragments of RanGAP1 fused to monomeric EGFP (wild type left panel; mutant with 4 of 5 NES residues mutated to alanine right panel) shown above confocal microscopy images of stable cell lines as representative z-stack average projections to

highlight cytoplasmic localization for wild type and nuclear localization for the mutant. Cells stained with DAPI; GFP visualized via native GFP fluorescence using 488 nm excitation. Brightness/contrast adjusted for individual channels.

B Schematic of CRISPR-Cas9 strategy to generate an in-frame deletion of RanGAP1 residues 5-17 to remove the RanGAP1 NES.

C Western blot analysis of wild type and clones (2, 3 and 10) expressing RanGAP1$^{\Delta NES}$ to highlight expression levels and amounts of unmodified and SUMO1-modified RanGAP1. 20 µg of lysate was loaded in each lane and probed with a rabbit polyclonal α-RanGAP1 antibody (Sigma, HPA062034) at a 1:4000 dilution (top blot) and β-actin as a loading control (bottom blot) probed with a mouse monoclonal α-β-actin antibody (Santa Cruz, SC81178) at a 1:500 dilution.

D Western blot analysis of wild type RanGAP1 or RanGAP1$^{\Delta NES}$ lysates to highlight similar levels of phosphorylation after nocodazole treatment. 7.5 µg of lysate was loaded in each lane and blots were probed with rabbit polyclonal α-RanGAP1 antibody (Sigma, HPA062034) at 1:2000 dilution.

E Confocal microscopy images for cells expressing wild type RanGAP1 or RanGAP1$^{\Delta NES}$ to highlight RanGAP1 localization to the nuclear periphery in both cell lines independent of the RanGAP1 NES. White arrowheads point to prototypical nuclear ring staining for RanGAP1 in the nuclear focal plane (top panels, z-stack slice shown) and RanGAP1 puncti on the periphery of the nuclear envelope after translocating 1 µm in the z-plane (bottom panels, z-stack slice shown). RanGAP1 detected with rabbit polyclonal α-RanGAP1 primary antibody (Bethyl, A302-027A) and α-rabbit IgG-Alexa647 secondary VHH nanobody (Thermo, SA5-10327), both at 1:1000 dilution. Brightness/contrast adjusted for individual channels.

F Confocal microscopy images for cells expressing wild type RanGAP1 or RanGAP1$^{\Delta NES}$ (clones 2 and 10) in the absence or presence of leptomycin B (LMB) to highlight nuclear accumulation RanGAP1$^{\Delta NES}$ relative to wild type RanGAP1. Cells were treated with methanol control (left panels, -) or 50 nM leptomycin B (LMB, right panels, +) for 20-21 hours, fixed, and

stained for RanGAP1 using the same antibodies and dilutions as in (E). Representative average 2D projections of confocal z-stacks shown with brightness/contrast adjusted separately for each channel. Right graph depicts the ratio of nuclear to cytoplasmic RanGAP1 calculated using CellProfiler.[74] Individual values and bars representing means +/- SD are shown. Kruskal-Wallis with Dunn's multiple comparison tests were used to calculate statistical significance using Prism. n ≥ 66 cells across at least 3 biological replicates. * P < 0.05, ** P < 0.01; *** P < 0.001; **** P < 0.0001, ns – not significant.

G Western blot analysis of Ran in cells expressing wild type RanGAP1 or RanGAP1$^{\Delta NES}$ to highlight similar levels of expression. Ran (top blot) detected with a mouse monoclonal α-Ran antibody (BD, 610340) at 1:8000 dilution and β-actin (bottom blot) as loading control (bottom blot) detected with a mouse monoclonal α-β-actin antibody (Novus, NBP1-47423) at 1:300,000 dilution. 20 µg of lysate was loaded in each lane.

H Confocal microscopy images with an α-Ran antibody in cells expressing wild type RanGAP1 or RanGAP1$^{\Delta NES}$ (clones 2 and 10) in the absence or presence of leptomycin B (LMB) to highlight cytoplasmic mislocalization of Ran in cells expressing RanGAP1$^{\Delta NES}$ with or without LMB or in wild type cells after LMB treatment. Ran detected with mouse α-Ran monoclonal primary antibody (BD, 610340) and α-mouse IgG-Alexa647 secondary antibody (H+L Thermo A32787) at 1:250 and 1:1000 dilutions, respectively. LMB treatment, imaging, and analysis as in (G). Right graph depicts results for n ≥ 73 across at least 3 biological replicates. p-values and statistical analysis as in G. No significant difference between the means of Δ2 (-LMB), Δ10 (-LMB), WT (+LMB), Δ2 (+LMB), Δ10 (+LMB).

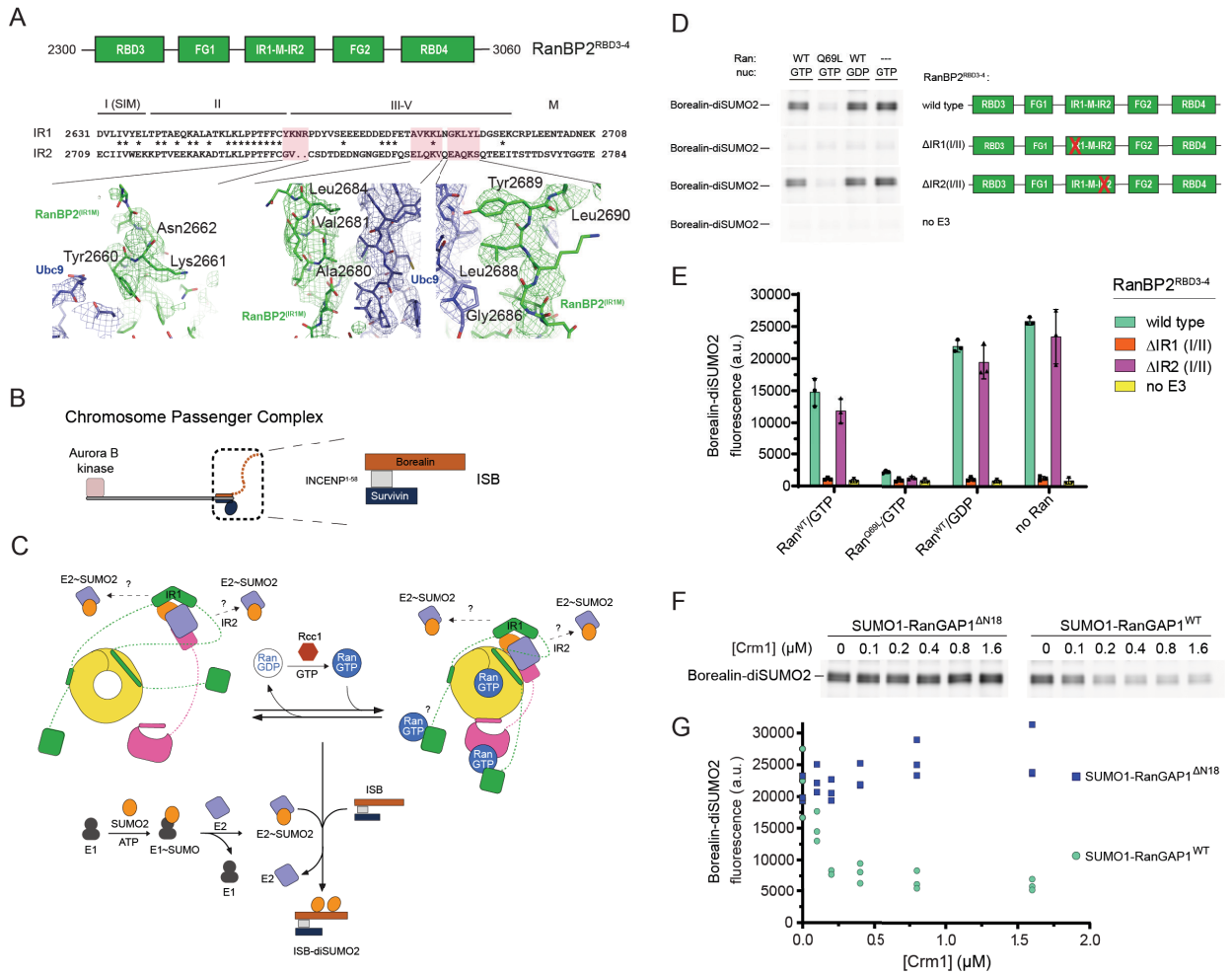

Figure 7 – RanBP2 E3 ligase activity depends on IR1 and cycling Ran GTPase, and is inhibited by RanGAP1 NES-Crm1 interactions.

A Schematic (top) of RanBP2^{RBD3-4} above the sequence alignment of IR1-M to IR2 (middle) and magnified views of highlighted regions to illustrate electron density for key residues that are present in IR1 but absent in IR2 (bottom, coloring as in Fig. 2), confirming that IR1 is the module seen in the structure. Motifs I(SIM), II, III-V and M[27] labelled as shown.

B Schematic of the Chromosome Passenger Complex (CPC) indicating the full length complex containing Aurora B kinase (left) and the truncated complex used in SUMO modification assays of Borealin that lacks the Aurora B kinase but retains interactions between Incenp$^{1-58}$, Survivin, and Borealin (right).[43,75]

C Schematic illustrating the components and reaction intermediates in our reconstituted system for SUMO2 modification of Borealin (D-G) to highlight cargo-free (left) and cargo-bound Crm1 (right) in concert with interactions with Ran, and to highlight IR1 and IR2 as potential E3 ligases with binding of charged E2~SUMO2 as indicated by question marks. The SUMO conjugation cascade and SUMO modification of Borealin at the bottom. Rcc1 and GTP indicated and used to regenerate Ran(GTP) for Ran GTP-GDP cycling.

D SDS-page analysis of Borealin-diSUMO2 products with variations of reaction components labeled at the top and various RanBP2 variants used indicated in schematics (right). Gels for Borealin-diSUMO2 products for wild type, ΔIR1(I/II), and ΔIR2(I/II) were cropped from a single representative gel (Supplemental Data); the “no E3” control was cropped from a separate gel run at the same time. Gels visualized via Alexa488 fluorescence (see Star Methods for details).

E Graph showing quantification of intensities for Borealin-diSUMO2 bands from (D) via densitometry. Individual data points for three independent experiments shown. Bars represent means +/- SD.

F SDS-page analysis of Borealin-diSUMO2 product formation with SUMO1-RanGAP1$^{\Delta N18}$ or wild type SUMO1-RanGAP1 in the presence of wild type RanBP2^{RBD3-4}, Ran^{Q69L}(GTP), Ubc9 and increasing concentrations of Crm1 (see Star Methods for details). Borealin-diSUMO2 products visualized as in (D).

G Graph showing quantification of intensities for Borealin-diSUMO2 bands from (F) via densitometry. Individual data points shown for three independent experiments.

Supplemental information titles and legends

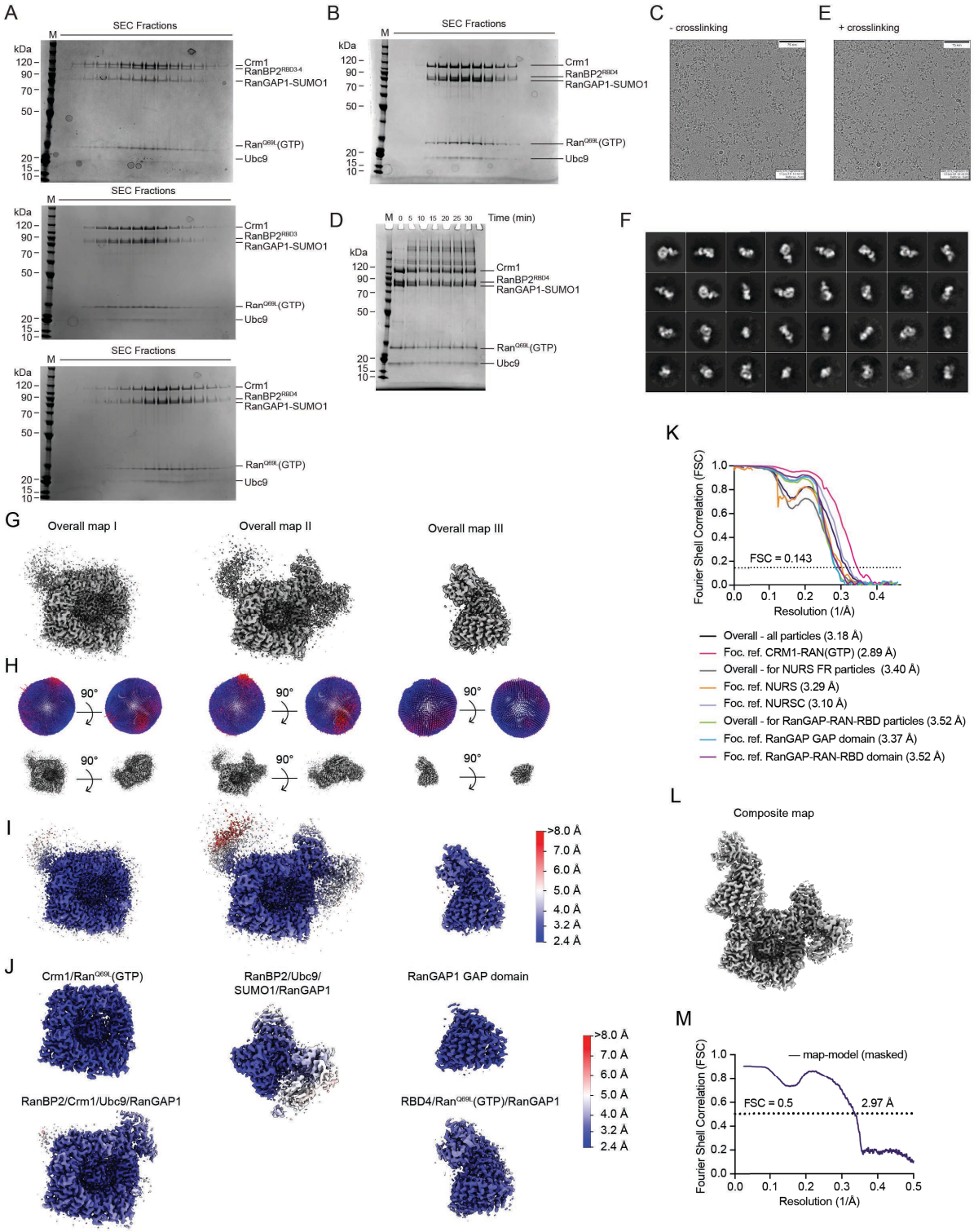

Figure S1 – Full Coomassie gels of complex reconstitutions and quality of cryo-EM reconstructions - related to Figures 1, 2, S2, and STAR Methods.

A Coomassie-stained SDS-PAGE gels of size exclusion fractions of Complexes I-III as shown in Fig 1(B-C).

B Coomassie-stained SDS-PAGE gel of size exclusion fractions of RanBP2^{RBD4}/SUMO1-RanGAP1/Ubc9/Crm1/Ran^{Q69L}(GTP) that were pooled, concentrated, and used for grid preparation.

C Representative micrographs showing the appearance of particles on grids without crosslinking.

D Crosslinking time course of RanBP2^{RBD4}/SUMO1-RanGAP1/Ubc9/Crm1/Ran^{Q69L}(GTP) with 250 μM of BS3. Reaction was quenched after 30 mins before grid preparation.

E Representative micrographs showing the appearance of particles on grids after BS3 crosslinking.

F Representative 2D class averages of the RanBP2^{RBD4}/SUMO1-RanGAP1/Ubc9/Crm1/Ran^{Q69L}(GTP) complex.

G-I Overall maps (G; see Fig. S2), their angular distribution plots (H), and their local resolution estimates (I).

J Focused refinement maps (see Fig. S2) and their local resolution estimates.

K FSC curves calculated between half maps from the indicated reconstructions.

L Composite map of RanBP2^{RBD4}/SUMO1-RanGAP1/Ubc9/Crm1/Ran^{Q69L}(GTP).

M FSC curve calculated between the final refined model and the composite map.

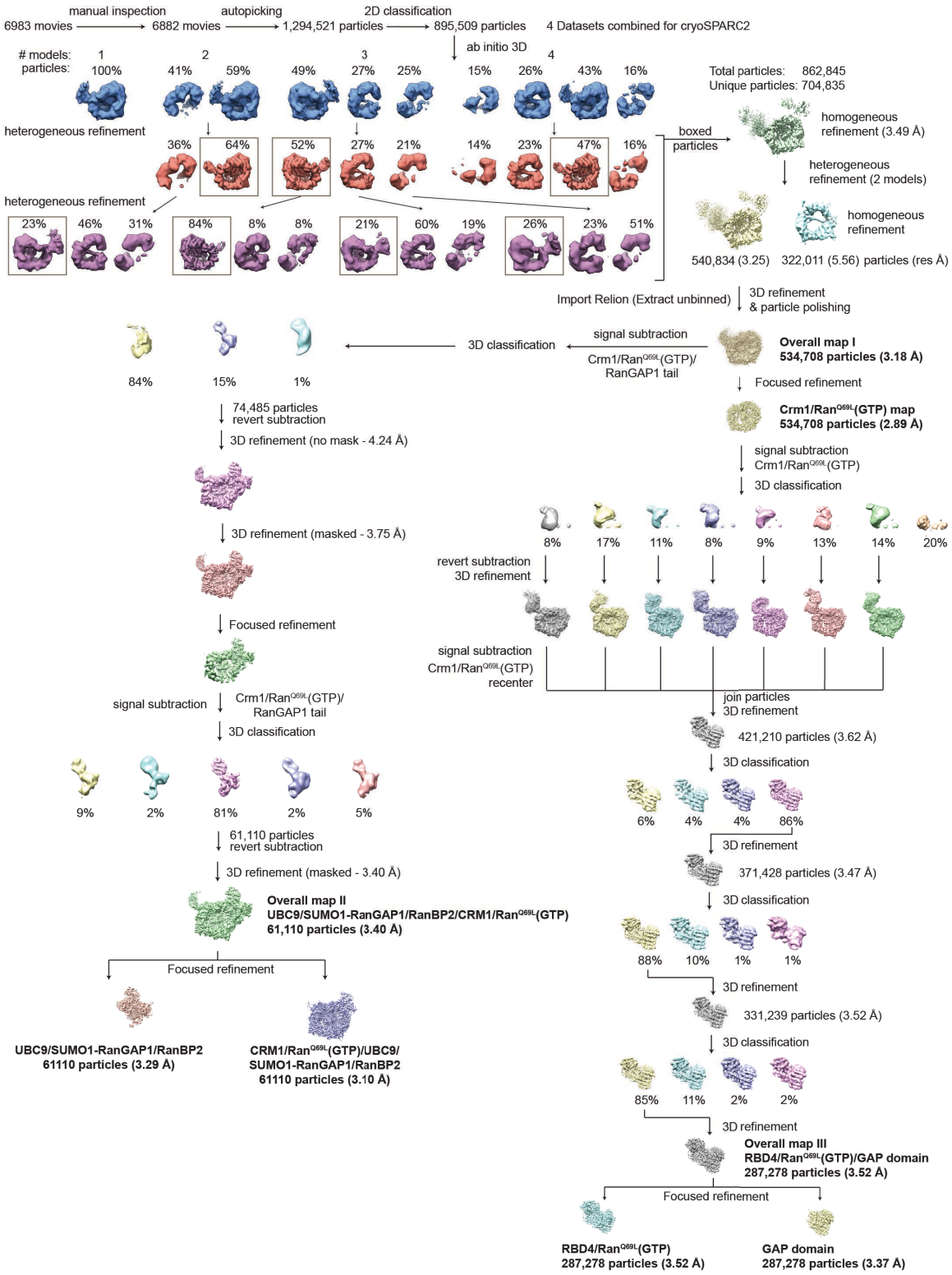

Figure S2 – Cryo-EM data collection and processing workflow used to generate overall and composite maps – related to Figures 2, S1, and STAR Methods.

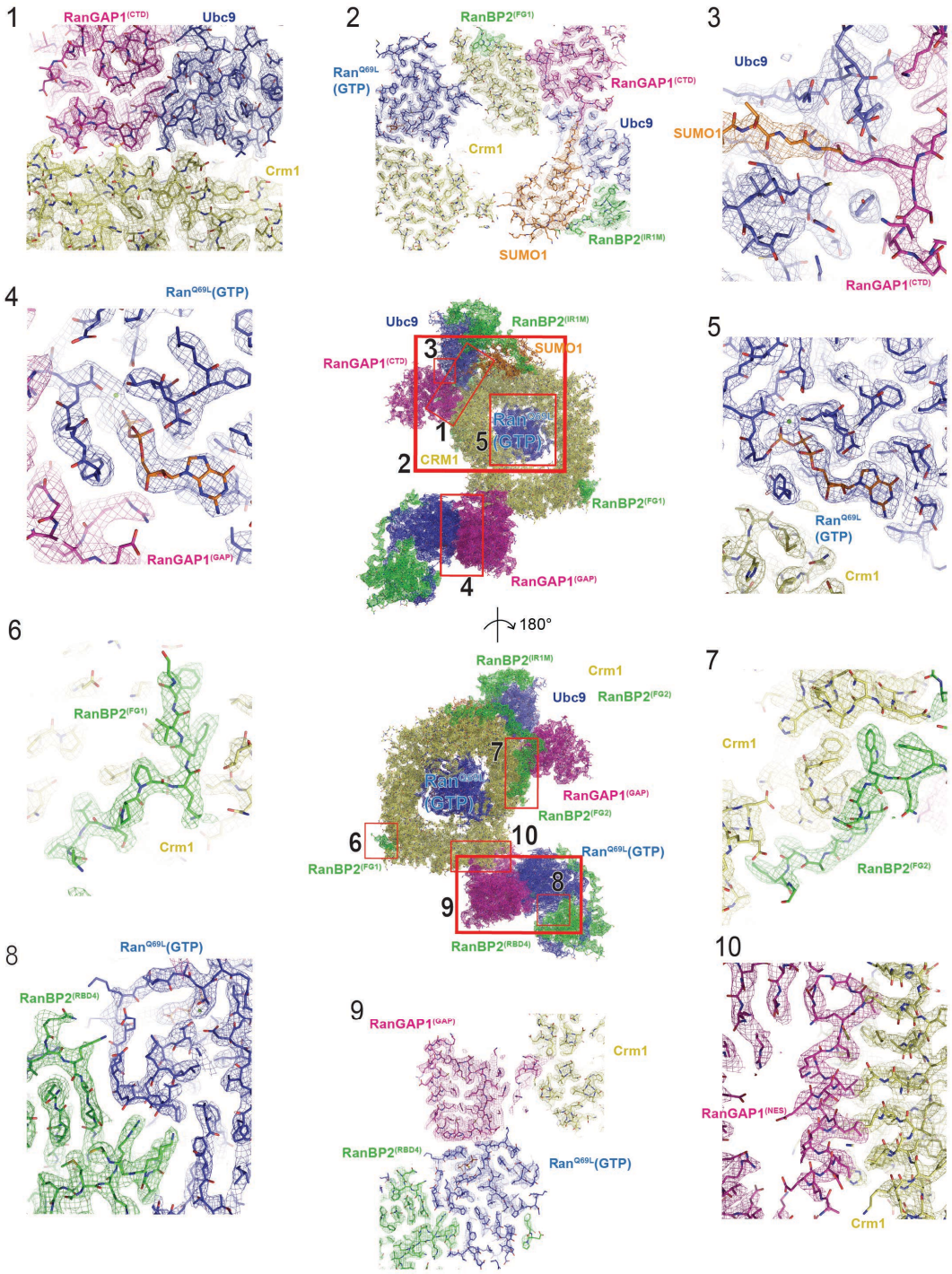

Figure S3 – Examples of EM density maps – related to Figures 2-5. Two overall views of the RanBP2^{RBD4}/SUMO1-RanGAP1/Ubc9/Crm1/Ran^{Q69L}(GTP) complex (middle) with boxed regions magnified and shown in detail in the numbered panels. Coloring same as in Fig. 2.

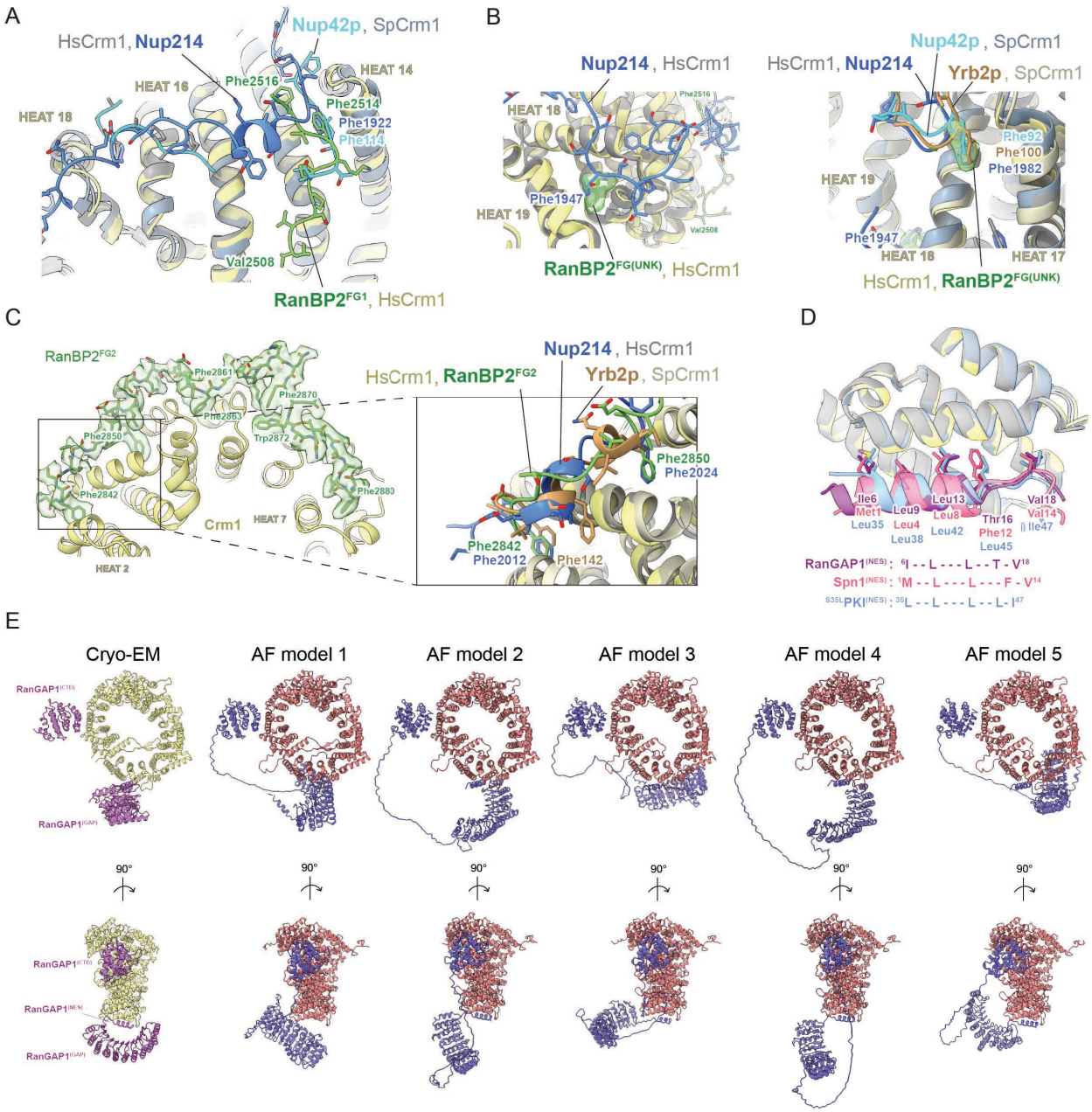

Figure S4 – Comparisons of RanBP2 FG repeats to those of other FG-repeat containing proteins and predictions of RanGAP1-Crm1 interfaces by AlphaFold multimer - related to Figures 3 and 5.

A Superpositions of the RanBP2 FG1 region with the FG repeats in previously determined structures for the human Nup214-Crm1-Spn1-Ran(GTP) (PDB 5DIS)[51] and *S. pombe* Nup42p-Crm1-PKI-Ran(GTP) (PDB 5XOJ)[53] complexes. Crm1 molecules were structurally aligned

(represented in cartoon) and all chains individually colored and indicated. Residues discussed in the text are labelled.

B Isolated, unassigned densities near the RanBP2^{FG1} region (RanBP2$^{FG(UNK)}$) observed in our cryo-EM reconstruction and the corresponding phenylalanines modelled in previously determined structures. Structures colored and indicated as in A with the addition of the yeast Yrb2p-Crm1-Ran(GTP) complex (PDB 3WYF).[54] Residues discussed in the text are labelled.

C Magnified view of a region of RanBP2^{FG2} near HEAT repeats 2-4 and overlaid structures of FG repeats from Nup214 and Yrb2p as colored in B. Residues discussed in the text are labelled.

D Superposition of the NES from RanGAP1 with the NES motifs from Spn1 (PDB 5DIS)[51] and ^{S35L}PKI (PDB 5XOJ).[53] Crm1 molecules were structurally aligned (represented in cartoon) and colored as in A and B and individual NES helices were colored as indicated. Key residues comprising the NES motifs are indicated in stick representation with the sequences indicated below.

E AlphaFold2 multimer predictions for RanGAP1-Crm1 interactions. Full-length RanGAP1 and Crm1 sequences were used as inputs for AlphaFold multimer, generating 5 models, each of which contained 5 predictions. The highest confidence predictions (as judged by ipTM + pTM scores) are shown for each model. All 5 models predicted the RanGAP1^{CTD}-Crm1 interaction and 4 of the 5 predicted the RanGAP1^{NES}-Crm1 interaction (models 2-5). When taking into account all 25 predictions, 24 of 25 show the CTD interaction and 17 of 25 show the NES interaction.

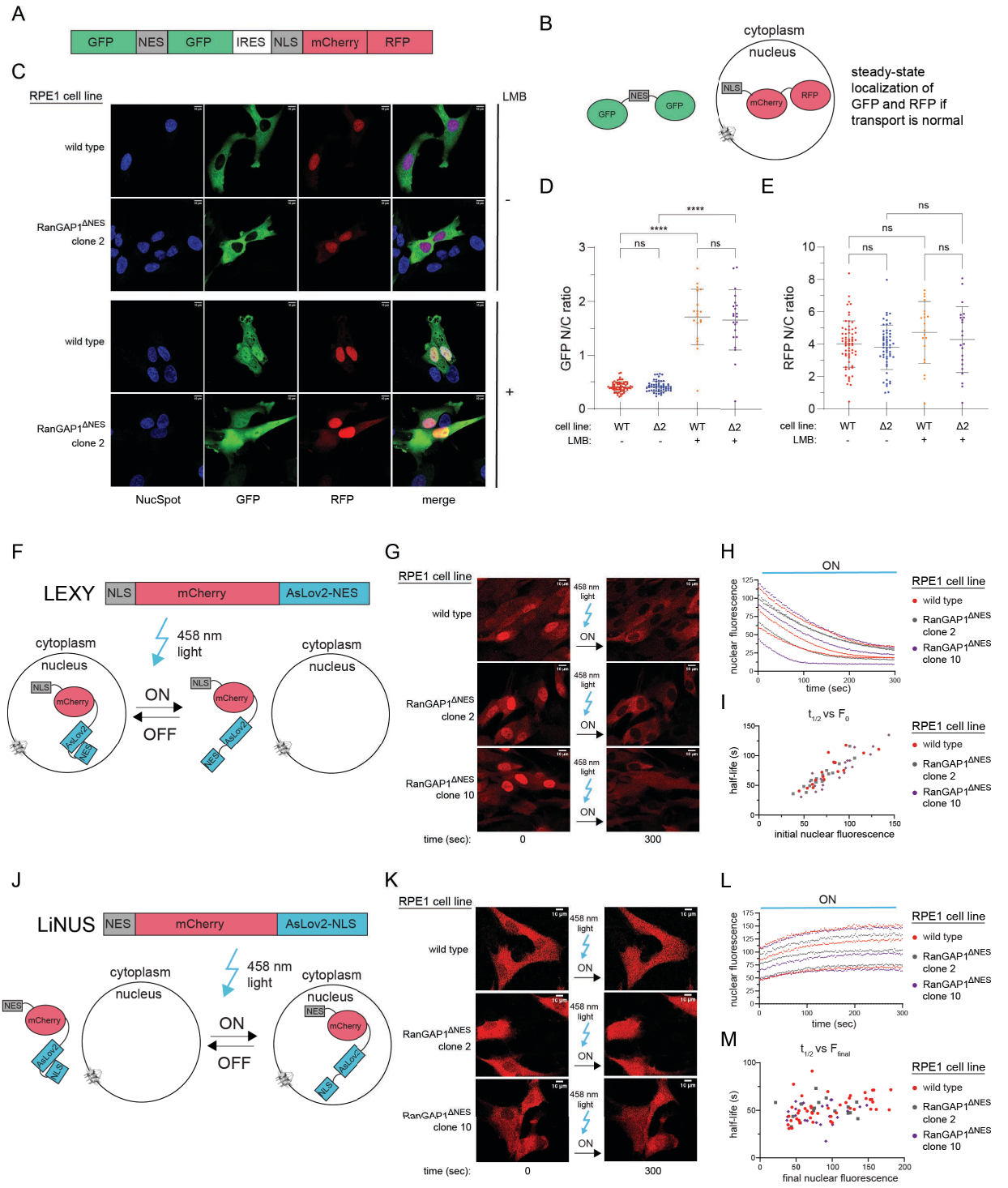

Figure S5 – engineered cells expressing the RanGAP1$^{\Delta NES}$ variant do not exhibit overt defects in nucleocytoplasmic transport – related to Figure 6.

A Construct encoding 2xGFP-NES-IRES-2xRFP-NLS[61] used to generate stable RPE1 cell lines in cell lines expressing wild type RanGAP1 or RanGAP1$^{\Delta NES}$.

B Expected localization for GFP and RFP in cells exhibiting normal NCT.

C Representative GFP and RFP average confocal z-stack images of live wild type RPE1 and RanGAP1$^{\Delta NES}$ clone 2 cells in the absence (-) or presence (+) of 50 nM LMB. Brightness/contrast adjusted for individual channels.

D Quantification of N/C ratios for GFP for wild type and RanGAP1$^{\Delta NES}$ clone 2 cells in the absence (-) or presence (+) of 50 nM LMB. Individual points plotted and bars represent means +/- SD. Statistical significance calculated in the same way as in Fig. 6 (G-H). P-values as defined in Fig. 6 (G-H).

E Quantification of N/C ratios for RFP for wild type and RanGAP1$^{\Delta NES}$ clone 2 cells in the absence (-) or presence (+) of 50 nM LMB. Individual points plotted and bars represent means +/- SD. Statistical significance calculated in the same way as in Fig. 6 (G-H). P-values as defined in Fig. 6 (G-H).

F Schematic of construct and experimental design for the LEXY assay.[63] mCherry fused to a constitutive NLS signal and an NES bound to and masked by the AsLov2 domain localizes primarily to the nucleus in the dark (OFF). Upon illumination with 458 nm light (ON), the NES is exposed by disengaging from the AsLov2 domain resulting in the export of mCherry into the cytoplasm.

G Example images of mCherry in live wild type RPE1, RanGAP1$^{\Delta NES}$ clone 2, and RanGAP1$^{\Delta NES}$ clone 10 cell lines stably expressing the LEXY construct before exposure (time = 0) and 5 minutes after pulsatile exposure (time = 300 seconds) to 458 nm light.

H Representative data generated by quantifying nuclear mCherry fluorescence in LEXY cells at 2.57 second intervals during 458 nm light exposure (see Star Methods for details).

I Plots of half-lives vs. initial nuclear fluorescence calculated from curves (fit to first order exponential models in Prism) such as shown in (H). Note that although the half-life for mCherry

export increases with increasing initial mCherry nuclear fluorescence, no difference is observed for wild type and RanGAP1$^{\Delta NES}$ cells across a wide range of initial nuclear mCherry fluorescence levels. Curves fitted to first order kinetic model in Prism to calculate half-life values.

J Schematic of construct and experimental design for the LiNUS assay.[62] mCherry fused to a constitutive NES signal and an NLS masked by the AsLov2 domain localizes primarily to the cytoplasm in the dark (OFF). Upon illumination with 458 nm light, the NLS is exposed resulting in nuclear translocation of mCherry (ON).

K Example images of mCherry in wild type RPE1, RanGAP1$^{\Delta NES}$ clone 2, and RanGAP1$^{\Delta NES}$ clone 10 cell lines stably expressing the LiNUS construct before exposure (time = 0) and 5 minutes after pulsatile exposure (time = 300 seconds) to 458 nm light.

L Representative data generated by quantifying nuclear mCherry fluorescence in LiNUS cells at 2.57 second intervals during 458 nm light exposure (see Star Methods for details).

M Plots of half-lives vs. final nuclear fluorescence calculated from curves (fit to first order exponential models in Prism) such as shown in (L). No difference is observed for wild type and RanGAP1$^{\Delta NES}$ cells.

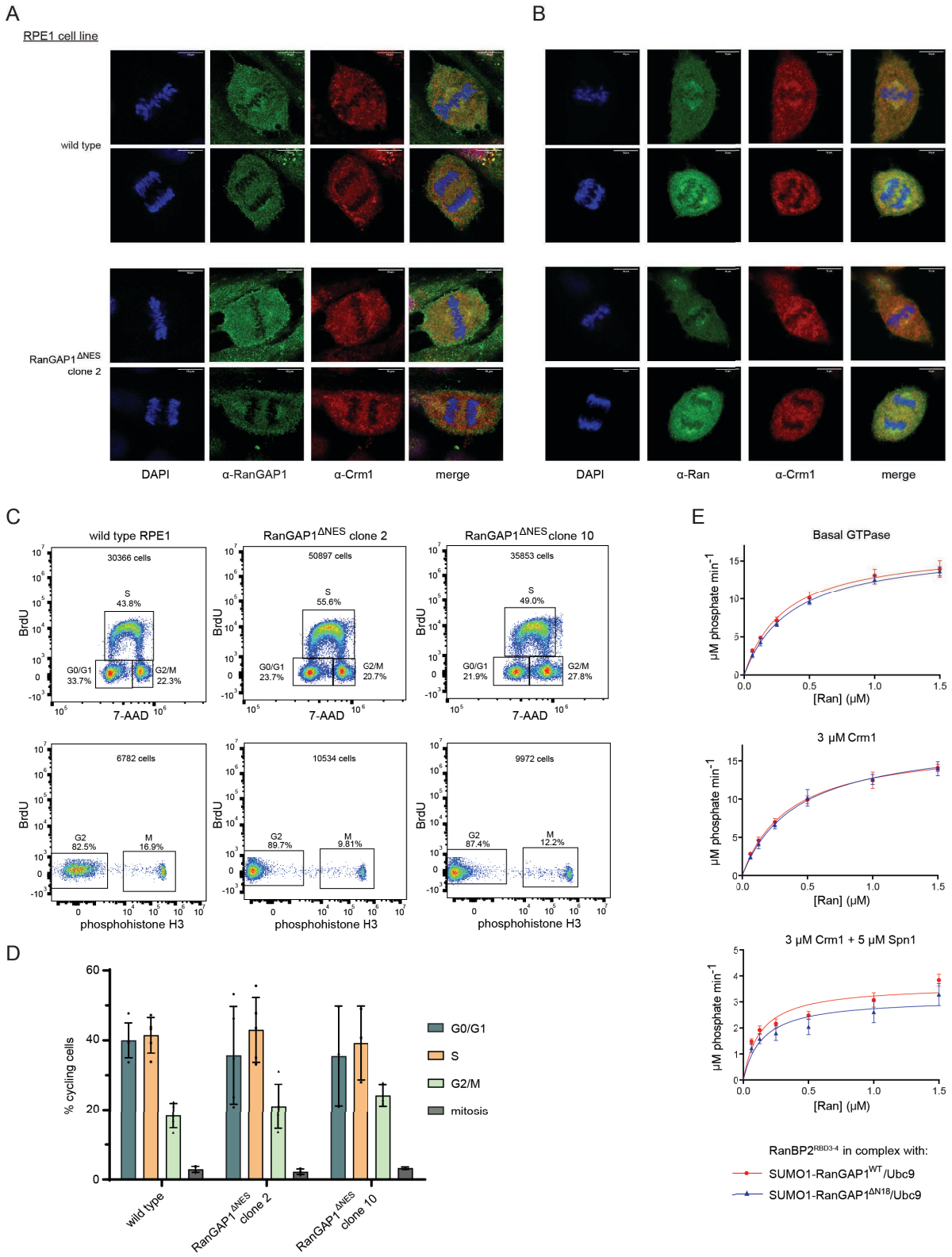

Fig. S6 - Cells expressing the RanGAP1$^{\Delta NES}$ variant exhibit the same mitotic localization of RanGAP1, Crm1, and Ran as wild type cells and do not show overt cell cycle defects. The NES

from RanGAP1 does not play a major role in the GTPase cycle or export complex disassembly. – related to Figure 6.

A Confocal microscopy images of fixed metaphase and anaphase wild type RPE1 (top) and RanGAP1$^{\Delta NES}$ clone 2 cells (bottom) co-stained with α-RanGAP1 and α-Crm1 antibodies and counterstained by DAPI. RanGAP1 detected with rabbit α-RanGAP1 polyclonal primary antibody (Bethyl, A302-027A) and alpaca α-rabbit IgG-Alexa488 secondary nanobody (Thermo, SA5-10323), both at 1:1000 dilution. Crm1 detected with mouse monoclonal α-Crm1 antibody directly labelled with Alexa647 (Santa Cruz, SC74454) used at 1:40 dilution. Representative 2D images are shown; brightness/contrast adjusted for individual channels.

B Confocal microscopy images of fixed metaphase and anaphase wild type RPE1 (top) and RanGAP1$^{\Delta NES}$ clone 2 cells (bottom) co-stained with α-Ran and α-Crm1 antibodies and counterstained by DAPI. Ran detected with rabbit polyclonal α-Ran antibody (Proteintech, 10469-1-AP) at a 1:100 dilution and alpaca α-rabbit IgG-Alexa488 secondary nanobody (Thermo, SA5-10323) at 1:1000 dilution. Crm1 detected as in (A) but antibody used at 1:300 dilution. Representative z-stack average projections are shown; brightness/contrast adjusted for individual channels.

C Representative FACS plots for wild type RPE1, RanGAP1$^{\Delta NES}$ clone 2, and RanGAP1$^{\Delta NES}$ clone 10 cell lines. Distribution of G0/G1, S, G2/M phases shown in BrdU vs. 7-AAD plots (top); cells in mitosis shown in BrdU vs. phosphohistone H3 plots (bottom). Boxed regions assigned to indicated cell cycle phases and cells within were quantified as indicated. Note that the indicated percentage of cells in mitosis is out of the G2/M population.

D Quantification of FACS data from plots such as those shown in C. Data from individual biological replicates plotted. Bars represent means +/- SD. At least 3 biological replicates were analyzed for each cell line.

E *In vitro* GTPase assays with pre-assembled RanBP2^{RBD3-4}/SUMO1-RanGAP1/Ubc9 complexes containing either wild type SUMO1-RanGAP1 or SUMO1-RanGAP1$^{\Delta N18}$ and wild

type Ran only (basal, top panel), Crm1 and Ran (middle panel), or Crm1, Spn1, and Ran (bottom panel). Data was fit to the Michaelis-Menten model.

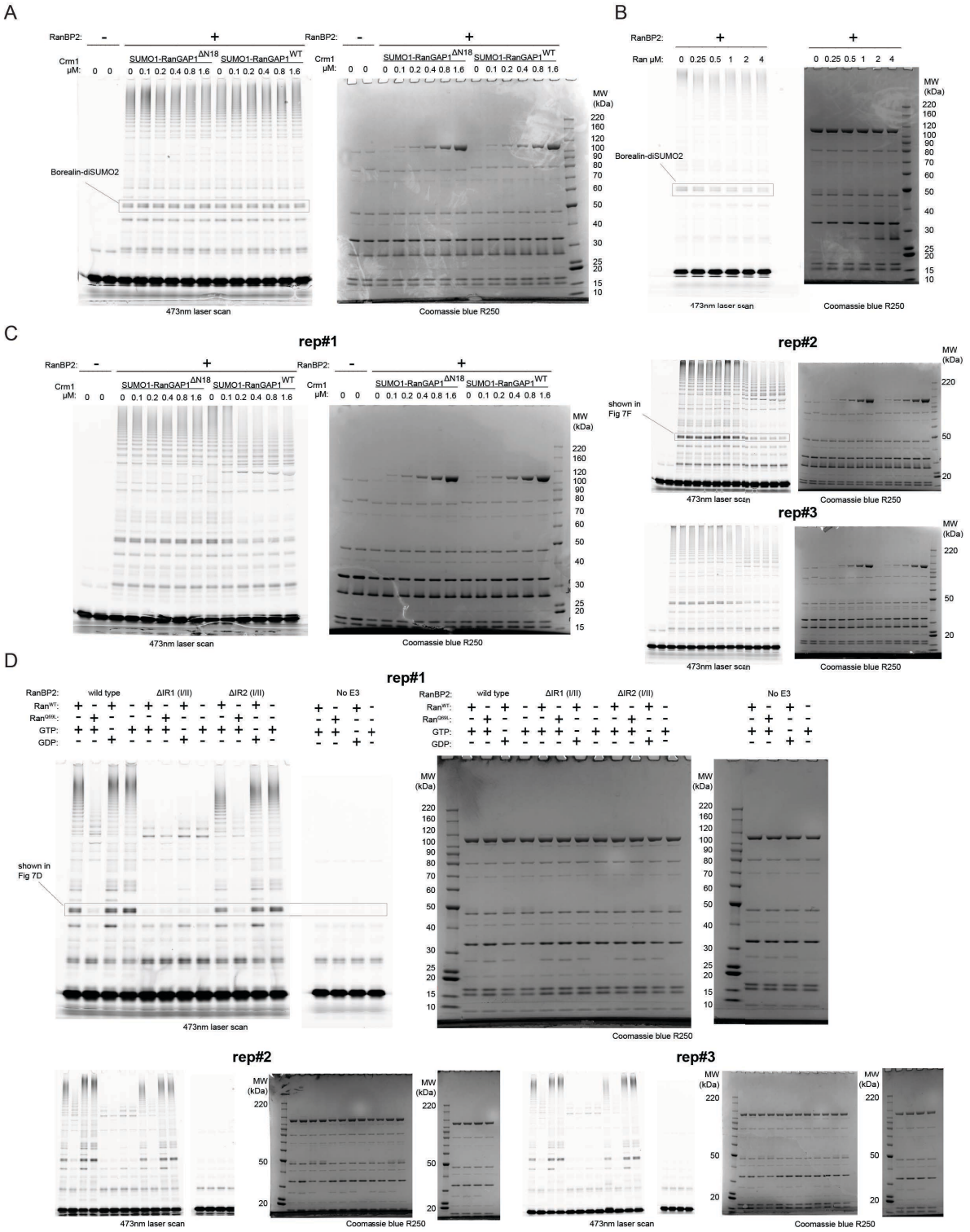

Figure S7 – The effect of wild type Ran on SUMO conjugation and full gels and replicates of SUMO conjugation assays – related to Figure 7.

A Crm1 does not inhibit SUMO conjugation in an NES-dependent manner in the presence of wild type Ran. Crm1 was titrated into reactions containing 3.2 μM wild type Ran and RanBP2^{RBD3-4} complexes containing either wild type SUMO1-RanGAP1 or SUMO1-RanGAP1$^{\Delta N18}$ as in Fig. S6E. Assays were done as for Ran^{Q69L}(GTP) in Fig. 7F except reactions were quenched after 50 minutes at 37 °C. Gels were scanned and stained as in Fig. 7F.

B Wild type Ran inhibits SUMO conjugation. Ran was titrated at the indicated concentrations into reactions containing wild type RanBP2^{RBD3-4}/SUMO1-RanGAP1/Ubc9/Crm1 complexes and reactions were done under the same conditions as in Fig. 7D. Gels were scanned and stained as in Fig. 7D.

C-D Full gels and associated replicates of data shown in Fig. 7 (D-G).

Source Data

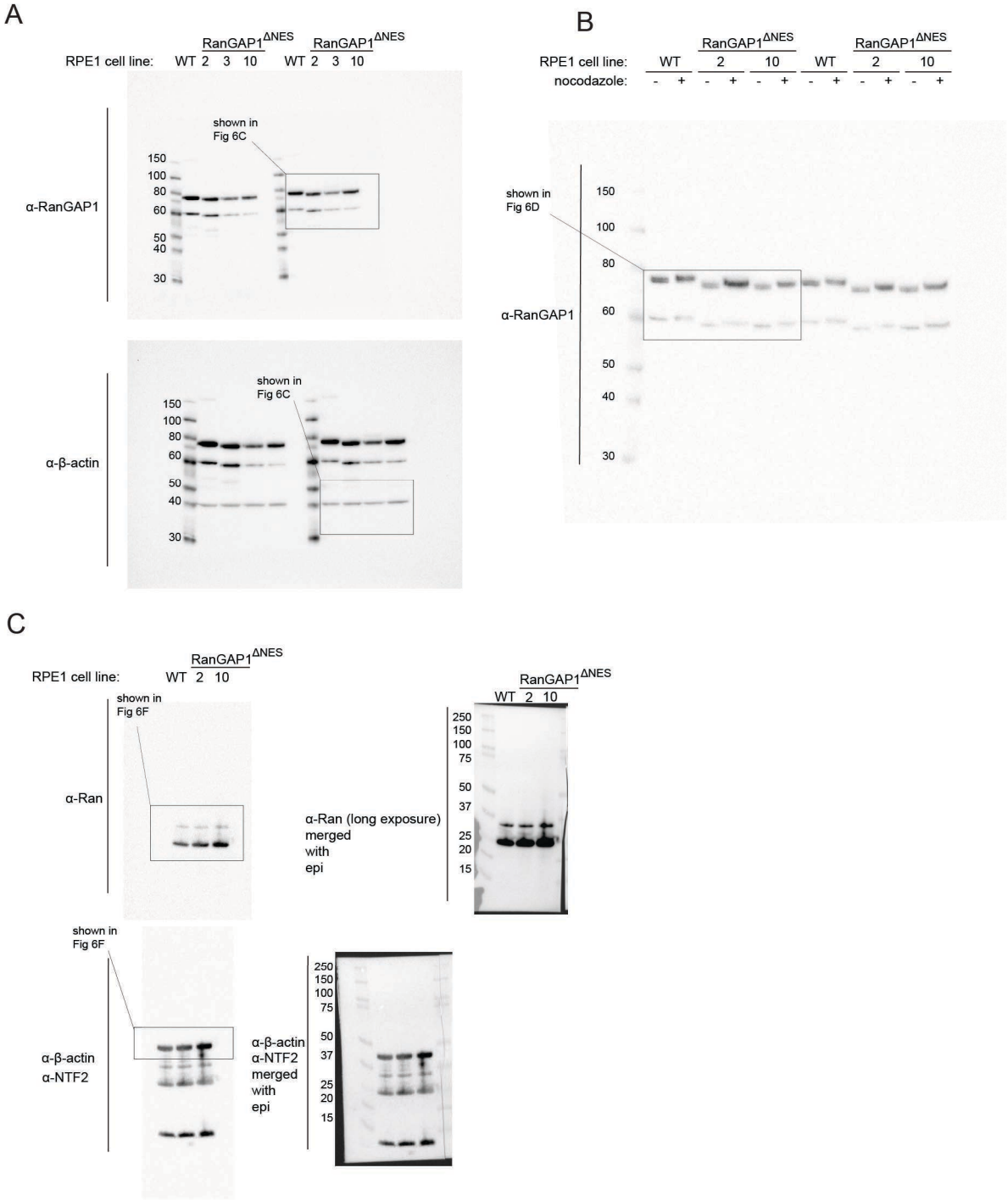

Full gels for panels shown in Fig. 6C, D, F.

STAR Methods

KEY RESOURCES TABLE –

REAGENT or RESOURCE	SOURCE	IDENTIFIER
Antibodies		
Rabbit polyclonal anti-RanGAP1	Bethyl Laboratories/Thermo Fisher Scientific	Cat#A302-027A
Rabbit polyclonal anti-RanGAP1	Sigma/Prestige	Cat#HPA062034
Mouse monoclonal anti-Ran	BD Biosciences	Cat#610340
Rabbit polyclonal anti-Ran	Proteintech	Cat#10469-1-AP
Mouse monoclonal anti-β-actin	Novus	Cat#NBP1-47423
Mouse monoclonal anti-β-actin	Santa Cruz	Cat#SC81178
Mouse monoclonal anti-Crm1-Alexa647 conjugate	Santa Cruz	Cat#SC74454
Goat polyclonal anti-rabbit IgG HRP conjugated secondary	Promega	Cat#W401B
Goat polyclonal anti-mouse IgG HRP conjugated secondary	Promega	Cat#W402B
Alpaca monoclonal anti-rabbit IgG-Alexa488 nanobody (VHH)	Thermo Fisher Scientific	Cat#SA5-10323
Alpaca monoclonal anti-rabbit IgG-Alexa647 nanobody (VHH)	Thermo Fisher Scientific	Cat#SA5-10327
Donkey polyclonal anti-mouse IgG-Alexa647 antibody (H+L)	Thermo Fisher Scientific	Cat#A32787
Mouse monoclonal anti-histone H3 phospho (Ser10) conjugated to PE	BioLegend	Cat#650808
Bacterial strains		
E. coli BL21CodonPlus(DE3)	Agilent Technologies	Cat#230245
E. cloni 10G competent cells	Lucigen	Cat#60106-2
E. coli SoluBL21(DE3)	Genlantis	Cat#C700200
Chemicals, peptides, and recombinant proteins		
IGEPAL CA-630	Sigma	Cat#I8896
Benzonase, ultrapure	Sigma	Cat#E8263
GTP	Thermo Fisher Scientific	Cat#R0461
ECL Prime Western blotting detection reagent	Cytiva	Cat#RPN2236
NuPAGE MES SDS Running Buffer (20X)	Thermo Fisher Scientific	Cat#NP000202
NuPAGE MOPS SDS Running Buffer (20X)	Thermo Fisher Scientific	Cat#NP000102
NuPAGE LDS Sample Buffer (4X)	Thermo Fisher Scientific	Cat#NP0007
NuPage 4-12% Bis-Tris protein gels	Thermo Fisher Scientific	Cat#NP0322BOX
Ni-NTA agarose	Qiagen	Cat#30250
HiLoad 26/600 Superdex 200 pg	Cytiva	Cat#28989336
HiLoad 26/600 Superdex 75 pg	Cytiva	Cat#28989334
Superdex 200 Increase 10/300 GL	Cytiva	Cat#28990944
Mono Q 10/100 GL	Cytiva	Cat#17-5167-01

Mono S 10/100 GL	Cytiva	Cat#17-5169-01
Mono Q 5/50 GL	Cytiva	Cat#17-5166-01
Ulp1 protease catalytic domain	In-house	N/A
Fetal Bovine Serum	Sigma	Cat#F2442
DME:F12 HG + HEPES + Glutamine + sodium bicarbonate cell media	MSK Media Preparation Facility	N/A
Costar 96-well flat bottom non-treated polystyrene plate	Sigma	CLS3370-100EA
µ-Slide 4-well glass bottom chamber slides	Ibidi	Cat#80427
4% Paraformaldehyde in PBS	Biotium	Cat#22023
Vectashield Plus Antifiade mounting medium with DAPI	Vector labs	Cat#H-2000-10
Leptomycin B solution	Enzo Life Sciences	Cat#ALX-380-100-C100
CytoFLEX LX Flow cytometer	Beckman/MSK flow cytometry facility	N/A
QuickExtract DNA solution	Biosearch Tech	Cat#QE09050
Critical commercial assays		
EnzChek Phosphate Assay Kit	Thermo Fisher Scientific	Cat#E6646
NucSpot Live 650 kit	Biotium	Cat#40082
BD Pharmingen APC BrdU Kit	BD	Cat#552598
Deposited data		
RanBP2/Ran(GTP)/SUMO1-RanGAP1/Ubc9/Crm1/Ran(GTP) - model	This paper	PDB: 9B62
RanBP2/Ran(GTP)/SUMO1-RanGAP1/Ubc9/Crm1/Ran(GTP) - composite map	This paper	EMDB-44235
RanBP2/SUMO1-RanGAP1/Ran(GTP)/Ubc9/Crm1/Ran(GTP) complex - overall map	This paper	EMDB-44236
Crm1/Ran(GTP) – focused refinement map	This paper	EMDB-44237
RanBP2 RBD4/Ran(GTP)/RanGAP1 GAP domain – overall map	This paper	EMDB-44238
RanBP2 RBD4/Ran(GTP) - focused refinement map	This paper	EMDB-44239
RanGAP1 GAP domain – focused refinement map	This paper	EMDB-44240
RanBP2/Ran(GTP)/SUMO1-RanGAP1/Ubc9/Crm1/Ran(GTP) complex where SUMO1-RanGAP1/Ubc9 was present – overall map	This paper	EMDB-44241
RanGAP1 C-terminal domain-SUMO1/Ubc9/RanBP2 E3 domain – focused refinement map	This paper	EMDB-44242
RanGAP1 C-terminal domain-SUMO1/Ubc9/RanBP2/Crm1/Ran(GTP) – focused refinement map	This paper	EMDB-44243
Experimental models: Cell lines		
Human: hTERT-RPE1 cell line	ATCC	Cat#:CRL4000

Human: hTERT-RPE1 lines harboring RanGAP1$^{\Delta NES}$ generated by CRISPR-Cas9	This paper	N/A
Human: hTERT-RPE1 cell lines stably transfected with pCMV-2xGFPNES-IRES-2xRFPNLS	This paper	N/A
Human: hTERT-RPE1 cell lines stably transfected with pCMV-NLS-mCherry-LEXY	This paper	N/A
Human: hTERT-RPE1 cell lines stably transfected with pCMV-NES-mCherry-LiNUS	This paper	N/A
Human: hTERT-RPE1 cell lines stably transfected with pCMV-RanGAP1$^{1\text{-}18\text{-}WT}$-mEGFP	This paper	N/A
Human: hTERT-RPE1 cell lines stably transfected with pCMV-RanGAP1$^{1\text{-}18\text{-}4AMUT}$-mEGFP	This paper	N/A
Human: hTERT-RPE1 cell lines harboring RanGAP1$^{\Delta NES}$ stably transfected with pCMV-2xGFPNES-IRES-2xRFPNLS	This paper	N/A
Human: hTERT-RPE1 cell lines harboring RanGAP1$^{\Delta NES}$ stably transfected with pCMV-NLS-mCherry-LEXY	This paper	N/A
Human: hTERT-RPE1 cell lines harboring RanGAP1$^{\Delta NES}$ stably transfected with pCMV-NES-mCherry-LiNUS	This paper	N/A
Oligonucleotides		
VB236_sgRNA_1 CACCGCAGCTTGGCAATGTCTTCCG Top strand of guide RNA 236 with BbsI site for ligation into PX458 and CRISPR	This paper	N/A
VB236_sgRNA_2 AAACCGGAAGACATTGCCAAGCTGC Bottom strand of guide RNA 236 with BbsI site for ligation into PX458 and CRISPR	This paper	N/A
VB240_sgRNA_1 CACCGGACACTTGCCAAGACTCAGG Top strand of guide RNA 240 with BbsI site for ligation into PX458 and CRISPR	This paper	N/A
VB240_sgRNA_2 AAACCCTGAGTCTTGGCAAGTGTCC Bottom strand of guide RNA 240 with BbsI site for ligation into PX458 and CRISPR	This paper	N/A
VB243 – forward primer for sequencing endogenous RanGAP1 locus for CRISPR-induced Δ5-17 deletion TACTGCAACTTTGGCCTCCT	This paper	N/A

VB244 – reverse primer for sequencing endogenous RanGAP1 locus for CRISPR-induced Δ5-17 deletion GGGCAAATGATCTCTGAGCC	This paper	N/A
Recombinant DNA		
pet28b-His$_5$-RanBP2$^{2300-3060}$	This paper	N/A
pet28b-His$_6$-RanBP2$^{2446-3060}$	This paper	N/A
pet28b-His$_6$-RanBP2$^{2300-2910}$	This paper	N/A
pet28b-His$_6$-RanBP2$^{2300-3060,\ \Delta 2631-2660}$ (ΔIR1 (motifs I/II))	This paper	N/A
pet28b-His$_6$-RanBP2$^{2300-3060,\ \Delta 2709-2738}$ (ΔIR2 (motifs I/II))	This paper	N/A
pSmt3-His$_6$-smt3-Crm1	This paper	N/A
pet28b-His$_6$-Ran	This paper	N/A
pet28b-His$_6$-Ran^{Q69L}	This paper	N/A
pet28b-His$_6$-SUMO1^{Q94P}	This paper	N/A
pet21a-SUMO2^{A2C}-His$_6$	This paper	N/A
pet28b-His$_6$-RanGAP1	This paper	N/A
pet28b-His$_6$-RanGAP1$^{\Delta N18}$	This paper	N/A
pet28b-His$_6$-Ubc9	Yunus and Lima, 2009	N/A
pet11c-SAE1	Yunus and Lima, 2009	N/A
pet28b-His$_6$-SAE2$^{1-549}$	Yunus and Lima, 2009	N/A
pUCIDT-Rcc1	IDT	Ref#211260129
pet28b-His$_6$-Rcc1	This paper	N/A
pMK-RQ-Bb-Incenp$^{1-58}$-Survivin-His$_6$-Borealin	Thermo Fisher Scientific	ConstructID:18AA7WPP
pRSFDuet1-His$_6$-Trx-Incenp$^{1-58}$-Survivin-Borealin	This paper	N/A
pSpCas9(BB)-2A-GFP (PX458)	Fa et al., 2013	Addgene plasmid #48138; RRID:Addgene_48138
pSpCas9(BB)-2A-mCherry (PX458-mCherry)	This paper	N/A
mEGFP-N1	Gift from Michael Davidson	Addgene plasmid #54767; RRID:Addgene_54767
pLVX-EF1alpha-2xGFP:NES-IRES-2xRFP:NLS	Mertens et al., 2015	Addgene plasmid #71396; RRID:Addgene_71396
pEGFP-N1-CMV-2xGFP:NES-IRES-2xRFP-NLS	This paper	N/A
pCDNA3.1-NLS-mCherry-LEXY (pDN122)	Niopek D., et al., 2016	Addgene plasmid #72655; RRID:Addgene_72655

pCDNA3.1-NES-mCherry-LiNUS (pDN77)	Niopek D., et al., 2014	Addgene plasmid #61347; RRID:Addgene_61347
Software and algorithms		
CellProfiler v4.2.5	Stirling D.R. et al., 2021	https://cellprofiler.org/; RRID:SCR_007358
FlowJo v10	BD Biosciences	https://www.flowjo.com/; RRID:SCR_008520
Coot	Emsley et al., 2010	https://www2.mrc-lmb.cam.ac.uk/personal/pemsley/coot/; RRID:SCR_014222
Gctf	Zhang, 2016	https://www2.mrc-lmb.cam.ac.uk/research/locally-developed-software/zhang-software/#gctf; RRID:SCR_016500
Fiji 1.53t	Schindelin et al., 2012	https://fiji.sc; RRID:SCR_002285
Jalview version 2.11.3.3	Waterhouse et al., 2009	www.jalview.org/; RRID:SCR_006459
MolProbity	Chen et al., 2010	http://molprobity.biochem.duke.edu; RRID:SCR_014226
Phenix suite	Adams et al., 2010	https://www.phenix-online.org/; RRID:SCR_014224
Prism version 10	Graphpad	https://www.graphpad.com/scientific-software/prism/; RRID:SCR_002798
Pymol version 2.5.4	Schroedinger LLC	https://pymol.org; RRID:SCR_000305
RELION 3.0 and 3.1.2	Scheres, 2012; Zivanov et al., 2018	http://www2.mrc-lmb.cam.ac.uk/relion; RRID:SCR_016274
Serial EM data collection software	Mastronarde et al., 2005	http://bio3d.colorado.edu/SerialEM/; RRID:SCR_017293
CryoSPARC 2	Punjani et al., 2017	www.cryosparc.com; RRID:SCR_016501
UCSF ChimeraX version 1.8	Pettersen et al., 2021	https://www.cgl.ucsf.edu/chimerax/; RRID:SCR_015872

UCSF MotionCor2	Zheng et al., 2017	https://emcore.ucsf.edu/ucsf-software; RRID:SCR_016499
Other		
Vitrobot Mark IV	FEI – Thermo Fisher	https://www.fei.com
Titan Krios	FEI – Thermo Fisher	https://www.fei.com
K2 Summit Camera	Gatan, Inc	www.gatan.com
UltrAuFoil R 1.2/1.3 holey grids	Quantifoil	www.quantifoil.com/products/ultraufoil

RESOURCE AVAILABILITY

Lead Contact

Further information and requests for resources and reagents should be directed to and will be fulfilled by the lead contact, Christopher D. Lima (limac@mskcc.org).

Materials Availability

All stable cell lines and plasmids generated in this study are available from the Lead Contact.

Data and code availability

- Cryo-EM density maps and atomic coordinates are deposited in the Electron Microscopy Data Bank (EMDB) and Protein Data Bank (PDB). Accession numbers can be found in key resources table.
- This paper does not report original code
- Any additional information required to reanalyze the data reported in this paper is available from the lead contact upon request.

Cloning, Protein Expression and Purification

Cloning and expression vectors for recombinant overexpression in *E. coli*

Human RanBP2$^{2300-3224}$ (RBD3 to C-terminus), RanGAP1, Crm1, and Ran were amplified from Invitrogen human cDNA libraries (tissue from lung, kidney, testes, and/or brain). RanBP2$^{2300-3060}$ (RanBP2^{RBD3-4}), RanBP2$^{2300-2910}$ (RanBP2^{RBD3}), RanBP2$^{2446-3060}$ (RanBP2^{RBD4}), RanBP2$^{2300-3060,\Delta 2631-2660}$ (RanBP2$^{RBD3-4,\Delta IR1(I/II)}$), and RanBP2$^{2300-3060,\Delta 2709-2738}$ (RanBP2$^{RBD3-4,\Delta IR2(I/II)}$) fragments were generated by using RanBP2$^{2300-3224}$ as template and subcloned into pet28b via restriction cloning or Gibson assembly. Wild type RanGAP1 was used as template to generate RanGAP1$^{\Delta N18}$ and both were cloned into pet28b. Wild type Ran was used as template to generate Ran^{Q69L} and both were cloned into pET28b. Wild type Crm1 was cloned into pSmt3 (pET28b based vector with N-terminal 6xHis-Smt3 tag). The gene for human Rcc1 was synthesized in pUCIDT (IDT) with flanking NdeI and XhoI restriction sites, digested with NdeI and XhoI, and cloned into pet28b. GST-Incenp$^{1-58}$/Survivin/His$_6$-Borealin was synthesized as a tricistronic construct in pMK-RQ-Bb (Thermo) with restriction sites flanking each protein module and T7 promoter, lac operator, and ribosome binding site sequences from the pRSF-Duet1 vector (Novagen) between GST-Incenp and Survivin and between Survivin and His$_6$-Borealin. The synthetic construct was cut out of pMK-RQ-Bb and cloned into pRSF-Duet1 between NcoI and XhoI sites. GST was then replaced by His$_6$-Trx (thioredoxin) by restriction cloning and the His$_6$ tag on Borealin was deleted via standard PCR protocols to generate the final His$_6$-Trx-Incenp$^{1-58}$/Survivin/Borealin construct in pRSF-Duet1. Full length SUMO2 harboring the A2C mutation was generated by PCR mutagenesis and cloned into pet21a. SUMO1$^{1-97}$ harboring the Q94P mutation was generated by PCR mutagenesis and cloned into pet28b. Wild type human Ubc9 (SUMO E2) was cloned into pet28b as previously described.[76] SAE1 and SAE2$^{1-549}$ (human SUMO E1$^{\Delta C}$) were cloned into pet11c and pet28b as previously described.[76] The gene

for Snurportin1 was synthesized in pcDNA3.1 (Invitrogen GeneArt) and cloned into the pSmt3 vector between the BamHI and SalI restriction sites.

Expression and purification of RanBP2

RanBP2 variants used for cryo-EM reconstitutions and analytical gel filtration runs (see Figs. 1 and S1) were expressed in BL21(DE3) Codon Plus (RIL) (Stratagene) cells using pET28b vectors encoding a thrombin-cleavable His_6-tag. For expression, cells were grown in Superbroth medium at 37°C in shaker flasks to OD_{600} of ~4-5, transferred to an ice bath for 30 min, and induced with 0.5 mM isopropyl-beta-D-thiogalactopyranoside (IPTG) in the presence of 2% ethanol. Cultures were grown overnight at 18 °C and harvested after 16 h, pellets resuspended in 50 mM Tris pH 8.0, 20% sucrose, and flash-frozen in liquid nitrogen. RanBP2 was purified by thawing bacterial cells and lysing them in 50 mM Tris pH 8.0, 20% (w/v) sucrose, 500 mM NaCl, 20 mM imidazole, 0.1% IGEPAL, 1 mM phenylmethylsulfonyl fluoride (PMSF), 2 mM β-mercaptoethanol (BME), and 1 µl benzonase (250 U, Sigma), 5 mM $MgCl_2$, and 0.5 mg/ml lysozyme. Sonication was then performed to complete lysis using a Branson sonifier (SFX550) and lysate was then centrifuged using a Beckman JA-20 rotor at 19000 rpm. Supernatant was then incubated with Ni-NTA resin (QIAGEN) equilibrated in His-wash buffer (HWB; 20 mM Tris-HCl pH 8.0, 500 mM NaCl, 10 mM imidazole, and 1mM tris-2-carboxyethylphosphine (TCEP)), a chaperone wash was done with HWB supplemented with 50 mM KCl and 10 mM $MgSO_4$, and the protein was eluted with His-elution buffer (HEB; 20 mM Tris-HCl pH 8.0, 500 mM NaCl, 250 mM imidazole, and 1mM TCEP). Further purification of RanBP2 was performed via size-exclusion chromatography (SEC) with a Superdex 200 HiLoad 26/600 prep grade column (Cytiva) equilibrated in 50 mM Tris pH 8.0, 500 mM NaCl, and 1 mM TCEP. Peak fractions were pooled, concentrated to ~100 µM with Amicon Ultra-15 concentrators (Millipore Sigma), and flash-frozen prior to reconstitution.

For use in SUMO conjugation assays, wild type RanBP2^{RBD3-4} was expressed as described above but in the absence of cold shock and ethanol. Pellets were resuspended in 50 mM Tris pH 7.5, 500 mM NaCl, 20 mM imidazole, 0.5 mM EDTA, 0.5 mM DTT, and SigmaFAST EDTA-free protease inhibitor tablets (lysis buffer). Cells were lysed and centrifuged as described above and supernatant was applied to Ni-NTA and washed with lysis buffer without SigmaFAST tablets (wash buffer). Protein was eluted with wash buffer supplemented with 250 mM imidazole, concentrated via Amicon Ultra-15 concentrators, and applied onto a Superdex 200 HiLoad 26/600 prep grade column equilibrated in 50 mM Tris pH 7.5, 500 mM NaCl, 0.5 mM EDTA, and 1mM DTT. Peak fractions were collected, concentrated, and dialyzed overnight at 4 °C against 50 mM Tris pH 7.5, 150 mM NaCl, 0.5 mM EDTA, 0.5 mM DTT in the presence of thrombin to cleave the His_6 tag. Dialyzed protein was injected onto a Mono Q 5/50 GL column (Cytiva) equilibrated in the dialysis buffer but containing 1 mM DTT. Protein was eluted in a linear gradient from 150 mM NaCl to 500 mM NaCl over 25 column volumes. Peak fractions were pooled and exchanged into 50 mM Tris pH 7.5, 300 mM NaCl, 1 mM TCEP, 0.1 mM EDTA (BP2 storage buffer) via Amicon Ultra-15 concentrators, aliquoted, and flash frozen. RanBP2-$^{RBD3-4,\Delta IR1(I/II)}$ and RanBP2$^{RBD3-4,\Delta IR2(I/II)}$ variants that were used in SUMO conjugation assays were expressed and purified as described for RanBP2 used in cryo-EM reconstitutions. However, after the Superdex 200 gel filtration step, RanBP2$^{RBD3-4,\Delta IR1(I/II)}$ and RanBP2$^{RBD3-4,\Delta IR2(I/II)}$ variants were further dialyzed, cleaved with thrombin, and run on a MonoQ 5/50 GL column exactly as described for the wild type RanBP2^{RBD3-4} variant that was used in SUMO conjugation assays. Peak fractions were pooled, exchanged into BP2 storage buffer, aliquoted, and flash frozen.

Expression and purification of RanGAP1

Full-length human RanGAP1 that was used for cryo-EM reconstitutions was expressed as described above for RanBP2 that was used in cryo-EM reconstitutions, but the cell line used was BL21(DE3) SoluBL21 cells (Genlantis) transformed with Codon Plus (RIL) plasmid

(Stratagene). Lysis and purification are also as described above for RanBP2, but with a lower NaCl concentration (350 mM vs 500 mM) at all relevant steps. Peak fractions off of the Superdex 200 26/600 column were pooled, concentrated to ~300 μM, and flash frozen.

Wild type and RanGAP1$^{\Delta N18}$ proteins that were used in SUMO conjugation assays were expressed as described above without cold shock or ethanol addition during expression. Cells were harvested and lysed as described above except that lysis buffer consisted of 50 mM Tris pH 7.5, 500 mM NaCl, 20 mM imidazole, 0.25 mM EDTA, 1 mM dithiothreitol (DTT), 1.5 μL per liter of culture of benzonase (250 U), and SigmaFAST EDTA-free protease inhibitor tablets. Lysate was loaded onto Ni-NTA and washed extensively with lysis buffer but without benzonase and protease inhibitors (wash buffer). Protein was eluted from Ni-NTA with wash buffer supplemented with 250 mM imidazole and loaded onto a Superdex 200 26/600 column equilibrated with 50 mM Tris pH 7.5, 350 mM NaCl, 1 mM EDTA, and 1 mM DTT. Peak fractions were collected, concentrated to ~10 mL, supplemented with thrombin to cleave the His_6 tag, and dialyzed against 4 L of buffer consisting of 25 mM pH Tris 7.5, 150 mM NaCl, 0.5 mM DTT, and 1 mM EDTA. Dialyzed sample was loaded onto a Mono Q 10/100 GL column (Cytiva) equilibrated with the dialysis buffer and protein was eluted via a linear gradient from 150 mM to 600 mM NaCl over 13 column volumes. Peak fractions were concentrated, exchanged into 25 mM Tris pH 7.5, 250 mM NaCl, 0.1 mM EDTA, and 1 mM TCEP via Amicon-15 Ultra concentrators, and flash frozen.

Expression and purification of Crm1

Full-length human Crm1 that was used for cryo-EM reconstitutions was expressed as described above for RanGAP1 that was used in cryo-EM reconstitutions. A pSmt3 vector, containing an N-terminal His_6-Smt3 tag, was used as a solubility enhancer for expression of Crm1. Lysis was carried out with 50 mM Tris pH 8.0, 20% (w/v) sucrose, 350 mM NaCl, 20 mM imidazole, 0.1% IGEPAL, 1 mM PMSF, 2 mM BME, and 1 μl benzonase (250 U), 2 mM

$Mg(OAc)_2$, and 0.5 mg/ml lysozyme. Sonication was then performed to complete lysis using a Branson sonifier and lysate was centrifuged using the JA-20 rotor at 19000 rpm. Supernatant was incubated with Ni-NTA resin equilibrated against His-wash buffer (HWB; 20 mM Tris pH 8.0, 500 mM NaCl, 10 mM imidazole, and 1 mM TCEP, a chaperone wash was done with HWB supplemented to a final concentration of 50 mM KCl and 10 mM $MgSO_4$, and the protein was eluted with His-elution buffer (HEB; 20 mM Tris pH 8.0, 500 mM NaCl, 250 mM imidazole, and 1 mM TCEP). The Ni eluate was then dialyzed O/N at 4°C (against 50 mM Tris pH 8.0, 150 mM NaCl, 2 mM $Mg(OAc)_2$, and 1 mM TCEP) in the presence of Ulp1 (to cleave Smt3 tag). The recovered dialysate was then loaded onto a Superdex 200 HiLoad 26/600 prep grade column equilibrated with 50 mM Tris pH 7.5/8.0, 50 mM NaCl, 2 mM $Mg(OAc)_2$, and 1 mM TCEP. Peak fractions were pooled and loaded onto a MonoQ 10/100 GL equilibrated in 50 mM Tris pH 8.0, 50 mM NaCl, 2 mM $Mg(OAC)_2$, 1 mM TCEP in order to further purify Crm1 and remove any trace Ulp1. Crm1 was eluted with a linear gradient of 50 mM Tris pH 8.0, 1 M NaCl, 2 mM $Mg(OAc)_2$, 1 mM TCEP. Peak fractions were pooled, concentrated to ~90 μM with Amicon Ultra-15 concentrators, and flash frozen prior to reconstitution.

Crm1 protein used for GTPase and SUMO conjugation assays was expressed as described above except no cold shock was done and ethanol was not added during expression. Pellets were harvested and resuspended in lysis buffer consisting of 50 mM Tris pH 7.5, 500 mM NaCl, 20 mM imidazole, 0.5 mM TCEP, 2 mM $Mg(OAc)_2$, and SigmaFAST EDTA-free protease inhibitor tablets. Protein was lysed and bound to Ni-NTA as described above except the wash buffer consisted of 50 mM Tris pH 7.5, 500 mM NaCl, 20 mM imidazole, 0.5 mM TCEP, and 2 mM $Mg(OAc)_2$ without KCl or $MgSO_4$. Dialysis and Ulp1 cleavage proceeded as above except Tris pH 7.5 was used whereas the Superdex 200 HiLoad 26/600 run was done in 50 mM Tris pH 7.5, 100 mM NaCl, 2 mM $Mg(OAc)_2$, and 1 mM TCEP. Peak fractions were pooled, diluted with buffer for a final concentration of 60 mM NaCl, and loaded onto a Mono Q 10/100 GL column equilibrated in 50 mM Tris pH 7.5, 60 mM NaCl, 2 mM $Mg(OAc)_2$, and 1 mM

TCEP. Crm1 was eluted in a linear gradient from 60 mM – 300 mM NaCl over 20 column volumes. Peak fractions were collected, exchanged into 50 mM Tris 7.5, 150 mM NaCl, 2 mM $Mg(OAc)_2$, and 1 mM TCEP via Amicon Ultra-15 concentrators, and flash frozen.

Expression and purification of Ran(GTP)

Human Ran was expressed as described above for RanBP2. Lysis of bacterial cells was performed in the presence of 50 mM Tris pH 8.0, 500 mM NaCl, 15 mM imidazole, 4 mM MgCl2, 10% glycerol, 2.5 mM β-mercaptoethanol, 1 mM PMSF, 0.5 mg/ml lysozyme, 20 μM GTP, and 1 μl benzonase (250 U). Sonication was performed to complete lysis using a Branson sonifier and lysate was centrifuged using a Beckman JA-20 rotor at 19000 rpm. Supernatant was then incubated with Ni-NTA resin equilibrated with 20 mM Tris-HCl pH 8.0, 500 mM NaCl, 15 mM imidazole, 4 mM $MgCl_2$, 10% glycerol, 2.5 mM BME, and 20 μM GTP, and the protein was eluted with 20 mM Tris-HCl pH 8.0, 500 mM NaCl, 500 mM imidazole, 4 mM $MgCl_2$, 10% glycerol, 2.5 mM BME, 20 μM GTP. After elution, the protein sample was treated with thrombin to cleave the His_6 tag and dialyzed overnight against 20 mM Tris pH 8.0, 250 mM NaCl, 4 mM $MgCl_2$, 10% glycerol, 1 mM TCEP and 10 μM GTP. Upon recovery from dialysis, Ran was loaded with GTP nucleotide by first incubating at RT for 30 min with 10x molar excess of Tris-buffered GTP pH 7.5 and 20 mM EDTA pH 8.0. Then, Tris-buffered 1 M $MgCl_2$ pH 7.5 was added to a final concentration of 40 mM $MgCl_2$, and the sample was incubated on ice for 30 min. After this, Ran was loaded onto a Superdex 75 HiLoad 26/600 (Cytiva) prep grade column for size-exclusion chromatography. Peak fractions were pooled and dialyzed a second time, against 20 mM Tris pH 8.0, 50 mM NaCl, 5 mM $MgCl_2$, 1 mM TCEP, followed by anion exchange chromatography on a MonoQ 10/100 GL column to separate Ran(GTP) from Ran(GDP). A linear ionic strength gradient was applied from 50 mM NaCl to 1 M NaCl, in the presence of 20 mM Tris pH 8.0, 5 mM $MgCl_2$, and 1 mM TCEP. Appropriate peak fractions were

pooled and concentrated in 3K MWCO Amicon Ultra-15 concentrators, flash frozen, and stored at -80 °C.

Wild type Ran protein used for GTPase and SUMO conjugation assays was expressed as described above except no cold shock was done and ethanol was not added during expression. Purification was as described above except 20-50 mM Tris pH 7.5 was used as buffer, 0.5-1 mM DTT as reducing agent, SigmaFAST EDTA-free tablets as protease inhibitor, and no lysozyme was used during lysis.

Expression and purification of Spn1

Human Spn1 was expressed as described for Crm1 that was used in cryo-EM reconstitutions. Lysis was carried out with 50 mM Tris pH 8.0, 20% (w/v) sucrose, 500 mM NaCl, 10 mM imidazole, 0.1% IGEPAL, 1 mM PMSF, 2 mM BME, 6 µl benzonase (250 U), 2 mM $Mg(OAc)_2$, and 0.5 mg/ml lysozyme. Sonication was then performed to complete lysis using a Branson sonifier and lysate was then centrifuged using the JA-20 rotor at 19000 rpm. Supernatant was then incubated with Ni-NTA resin equilibrated against wash buffer (50 mM Tris pH 8.0, 500 mM NaCl, 10 mM imidazole, 2 mM $Mg(OAc)_2$ and 1mM TCEP), and the protein was eluted with wash buffer containing 250 mM imidazole. The Ni eluate was then dialyzed O/N at 4 °C against 50 mM Tris pH 8.0, 200 mM NaCl, 2 mM $Mg(OAc)_2$ (dialysis buffer), and 1 mM TCEP in the presence of Ulp1 to cleave the Smt3 tag. Dialyzed protein was loaded onto a Superdex 75 HiLoad 26/600 column equilibrated with dialysis buffer. Peak fractions were pooled and concentrated in Amicon Ultra-15 concentrators, flash frozen, and stored at -80 °C.

Expression and purification of human Rcc1

BL21(DE3) Codon Plus (RIL) cells harboring pet28b-hRcc1 (containing a thrombin-cleavable N-terminal His_6 tag) were grown at 37°C in LB to OD 0.6-0.8, shifted to 18°C, and induced with 0.5 mM IPTG. After 16-20 hours of expression cells were pelleted and

resuspended in a lysis buffer consisting of 50 mM Tris pH 7.5, 500 mM NaCl, 20 mM imidazole, 0.25 mM EDTA, 0.5 mM DTT, 1.5 µL of Ultrapure Benzonase (Sigma) per 1 L of culture, and *Complete* EDTA-free protease inhibitor cocktail tablets (Roche). After sonication, lysate was centrifuged using a Beckman JA-20 rotor at 18000 rpm and supernatant was applied onto Ni-NTA beads. After washing the Ni-NTA beads with at least 10 CV of wash buffer (lysis buffer without protease inhibitors or Benzonase), protein was eluted with a buffer containing 50 mM Tris pH 7.5, 300 mM NaCl, 250 mM imidazole, 0.25 mM EDTA, 0.5 mM DTT. Eluted protein was concentrated via Amicon Ultra- 30 concentrators and diluted 10-fold with a buffer consisting of 50 mM Tris pH 7.5, 150 mM NaCl, 0.5 mM DTT, and 1 mM EDTA. The His_6 tag was cleaved by adding 50 units of thrombin (Sigma, T7513) and incubating overnight at 4 °C. After cleavage by thrombin, protein was injected onto the Superdex HiLoad S200 26/600 column equilibrated in 50 mM Tris pH 7.5, 150 mM NaCl, 1 mM DTT, and 1 mM EDTA. Peak fractions were pooled, concentrated, and injected onto a Mono S 10/100 GL column equilibrated in the same buffer as the S200 26/600 column. Protein was eluted from 150 mM NaCl – 600 mM NaCl over 10 column volumes. Peak fractions were pooled, concentrated, and exchanged into 50 mM Tris pH 7.5, 200 mM NaCl, 1 mM DTT, 1 mM EDTA via an Amicon concentrator. Protein concentration was measured via absorbance at 280 nm and protein was flash frozen and stored at -80 °C.

Expression and purification of the Incenp$^{1-58}$-Survivin-Borealin complex

BL21 DE3 Codon Plus (RIL) cells harboring pRSFDuet His_6-Trx-Incenp$^{1-58}$-Survivin-Borealin (His_6-Trx-ISB) were grown in LB at 37 °C to OD ~0.7, protein expression was induced by the addition of 0.5 mM IPTG, and cells were moved to 18 °C for overnight expression. After 16-20 hours, cells were pelleted and resuspended in lysis buffer consisting of 50 mM Tris pH 7.5, 500 mM NaCl, 20 mM imidazole, 0.5 mM DTT, 0.5 mM EDTA, 1.5 µL of Ultrapure Benzonase per 1 L of culture, and 1 tablet of SigmaFAST protease inhibitor per 60 mL of buffer. Cells were lysed, centrifuged, and applied to Ni-NTA as described for Rcc1 above. Ni-NTA

beads were washed with at least 10 CV of wash buffer (same as for Rcc1) and eluted in 50 mM Tris pH 7.5, 500 mM NaCl, 250 mM imidazole, 0.25 mM EDTA, 0.5 mM DTT. The Ni-NTA eluate was concentrated via Amicon Ultra-15 concentrator and loaded onto the Superdex HiLoad S200 26/600 column pre-equilibrated in 50 mM Tris pH 7.5, 350 mM NaCl, 1 mM DTT, and 1mM EDTA. Appropriate fractions were pooled, concentrated to ~10 mL, and TEV protease (in-house) was added to a final concentration of 0.5 μM to cleave the His_6-Trx tag. Sample was dialyzed overnight at 4 °C into 25 mM HEPES pH 7.5, 150 mM NaCl, 2 mM DTT, 1 mM EDTA using a 12 mL 7K MWCO dialysis cassette (Thermo). Dialyzed protein was loaded onto the Mono S 10/100 GL equilibrated in 25 mM HEPES pH 7.5, 150 mM NaCl, 1 mM DTT, 1 mM EDTA and eluted via gradient from 150 mM NaCl – 750 mM NaCl over 15 column volumes. Appropriate fractions were concentrated and exchanged into 50 mM Tris pH 7.5, 250 mM NaCl, 1 mM DTT, 0.25 mM EDTA via the Amicon Ultra-15 concentrator, aliquoted, and frozen at -80 °C.

Expression and purification of SUMO2^{A2C}, SUMO1^{Q94P}, Ubc9, and SUMO E1$^{\Delta C}$

Full length C-terminally His_6-tagged SUMO2^{A2C} and N-terminally His_6-tagged mature SUMO1^{Q94P} were expressed in BL21 DE3 Codon Plus (RIL) cells in LB and purified as described for other His_6 tagged SUMO variants.[33,76] BL21 DE3 Codon Plus (RIL) cells expressing His_6-tagged Ubc9 were grown in LB at 37 °C until OD ~0.6-0.8, cold-shocked on ice, and shifted to 18 °C prior to adding 2% ethanol and 0.5 mM IPTG. Ubc9 was lysed and purified in a manner similar to the RanBP2 that was used for cryo-EM reconstitutions except the Ni-NTA buffer contained 350 mM NaCl and the Ni-NTA eluate was concentrated and injected onto a Superdex 75 HiLoad 26/600 column equilibrated in 20 mM Tris pH 8.0, 150 mM NaCl, and 1 mM TCEP. Appropriate gel filtration fractions were pooled, concentrated, and flash frozen. SUMO E1$^{\Delta C}$ was expressed and purified as described above for Ubc9 except the Ni-NTA eluate

was injected onto a Superdex 200 HiLoad 26/600 column, peak fractions were pooled, concentrated, and flash frozen in liquid nitrogen.

Electron Microscopy Sample Preparation, Imaging and Analysis

Reconstitution of RanBP2 Complexes

Purified RanGAP1 was first conjugated to SUMO1^{Q94P} in vitro. Briefly, RanGAP1 and SUMO1 were incubated in a 1:1.5 molar ratio for 7 h at 37 °C in the presence of human SUMO E1 and E2 enzymes in 20 mM HEPES pH 7.4, 50 mM NaCl, 5 mM $MgCl_2$, 1 mM TCEP, and 5 mM ATP. The reaction was tracked by SDS-PAGE with hourly time points to determine when ~95% of RanGAP1 was modified by a single SUMO1 moiety. Purification of SUMO1^{Q94P}-RanGAP1 from leftover unreacted species was performed via anion exchange chromatography by passing over a MonoQ 10/100 GL column equilibrated in 20 mM Tris pH 8.0, 100 mM NaCl, 1 mM TCEP and eluted via a linear gradient of Buffer B, 20 mM Tris pH 8.0, 1000 mM NaCl, 1 mM TCEP. RanBP2^{RBD4}/RanGAP1-SUMO1^{Q94P}/Ubc9 was then reconstituted by incubating purified RanGAP1-SUMO1^{Q94P} with excess RanBP2^{RBD4} and Ubc9 (1.0 : 2.5 : 2.5 molar ratio), dialyzed against 20 mM Tris pH 8.0, 100 mM NaCl, 1 mM TCEP, and purified on a MonoQ column (Buffer A: 20 mM Tris pH 8.0, 50 mM NaCl, 1 mM TCEP; Buffer B: 20 mM Tris pH 8.0, 1000 mM NaCl, 1 mM TCEP) and eluted via a two-step gradient where the first was 0-30% B over 2 column volumes and the second was 30-55% B over 14 column volumes . Finally, purified RanBP2^{RBD4}/SUMO1-RanGAP1^{Q94P}/Ubc9 was incubated with excess Crm1 and Ran^{Q69L}(GTP) and purified by gel filtration on an S200 Increase 10/100 GL (Cytiva) column equilibrated with 20 mM HEPES pH 7.4, 110 mM potassium acetate, 2 mM magnesium acetate, and 1 mM TCEP. The appropriate fractions were pooled and the complex was concentrated to ~ 9 mg/ml using Amicon UltraCel 10K MWCO centrifugal filters (Merck Millipore).

Crosslinking for cryo-electron microscopy

Reconstituted and purified RanBP2^{RBD4}/SUMO1^{Q94P}-RanGAP1/Ubc9/Crm1/ Ran^{Q69L}(GTP) was lightly crosslinked with 250 μM bis(sulfosuccinimidyl)suberate (BS^3), an amine-to-amine crosslinker that is water-soluble and non-cleavable. After crosslinking for 30 min, the reaction was quenched with 50 mM Tris pH 7.5. The sample was then supplemented with 0.1% CHAPSO and immediately used for grid preparation. Aliquots for analysis of protein were added to 4X LDS sample buffer supplemented with 10% v/v BME and separated by SDS-PAGE followed by Coomassie or SYPRO Ruby staining.

Cryo-electron microscopy data collection

UltrAuFoil R 1.2/1.3 holey grids were glow-discharged for 60 s at 0.37 mBar, 15 mA in a Pelco easiGlow air system (TED PELLA). Three μl of a suspension of lightly cross-linked complexes of hRanBP2^{RBD4}/SUMO1^{Q94P}-RanGAP1/Ubc9/Crm1/Ran^{Q69L}[GTP] at a concentration of 9.7 mg/ml were applied per grid and plunge-frozen in liquid ethane using a Vitrobot Mark IV (FEI) at 22 °C, 100% humidity (20 s wait time, 3.0 s blot time). Grids were screened for suitable particle density using an MSKCC in-house Titan Krios 300kV (FEI) microscope and Serial EM data collection software.[77] Data collection was performed on a Titan Krios 300kV (FEI) instrument using a K2 Summit direct detector (Gatan). A total of 6882 movies (50 frames/movie, 10 s exposure time) were collected from 4 grids in super-resolution mode with a defocus range from -1.0 to -3.0 μm at a dose rate of 10.0 e-/px/sec and a total dose of 85.2 e-/Å^2/movie. The exposure of the movies was filtered in a dose-dependent manner to weigh the amplitudes of each movie frame, preserving low-resolution contrast across the exposure while favoring high-resolution information from early frames that sustained less radiation damage.

Image Processing and Map Reconstruction

Movies were processed with MotionCor2 to generate dose-weighted aligned and averaged micrographs alongside aligned movies with pixel size of 1.09 Å/pixel.[78] 5964 micrographs were selected for further processing based on their appearance, CTF estimation and number of particles. In RELION 3.0,[79] ~1000 particles were selected to generate a small set of 2D class averages that were then used as templates for auto-picking the remaining particles. During initial auto-picking in RELION 3.0, 1294521 particles were extracted with box size of 300 x 300 pixels. This particle stack was input to cryoSPARC2 (Structura Biotechnology Inc) to obtain an initial set of 2D class averages and to remove junk particles. After 2D classification in cryoSPARC2, 895509 particles remained. These ~895K particles were used for generation of *ab initio* reconstructions in cryoSPARC2, asking in parallel for 1, 2, 3 and 4 distinct reconstructions. Initial 3D classification in cryoSPARC2 (employing heterogeneous refinements) resulted in isolation of a subset of particles (count: 540834) containing Crm1 bound with Ran^{Q69L}(GTP) and an amorphous protrusion of electron density off the side of Crm1 that was preliminarily thought to be the GAP domain of RANGAP1. Left behind from this classification were ~322k particles that upon reconstruction gave rise to free Crm1. The ~540K subset of particles clearly containing a central Crm1/Ran^{Q69L}(GTP) were ported back into RELION 3.0 for further analysis. After initial rounds of particle orientation assignment and image reconstruction, focused refinement of the central Crm1/Ran^{Q69L}(GTP) was performed, as this was observed to be the part of the structure that exhibited the greatest degree of structural rigidity. Using these orientations as a starting point, four rounds of the following four steps were carried out to improve the achievable resolution of the particle data: (1) Bayesian particle polishing, (2) 3D refinement followed by focused refinement on Crm1/Ran^{Q69L}(GTP), (3) defocus (CTF) refinement, and finally (4) another 3D refinement step.

Subsequently, another round of 3D refinement followed by focused refinement on Crm1/Ran^{Q69L}(GTP) resulted in a sharpened map resolution of 2.89 Å for the central Crm1/Ran^{Q69L}(GTP). Additional densities were observed adjacent to the central

Crm1/Ran^{Q69L}(GTP). To resolve these densities, a 3D mask was generated around Crm1/Ran^{Q69L}(GTP) and to subtract that region within each particle. These subtracted particles were 3D classified without image alignment, using a reference mask that was large enough to accommodate the volume of all possible orientations. Seven of eight classes exhibited densities, which were resolved as the GAP domain of RanGAP1 bound to Ran^{Q69L}(GTP), which was engaging the RBD4 of RanBP2. Each of these were masked to subtract densities outside the mask followed by recentering as implemented in RELION 3.1.2. The resulting GAP/ Ran^{Q69L}(GTP)/RBD4 particles were aligned to a 3D reference and following several rounds of focused 3D classification without image alignment, the final, postprocessed reconstruction of the RanGAP1 GAP/Ran^{Q69L}(GTP)/RBD4 subcomplex was resolved to a resolution of 3.4 Å followed by focused refinements.

The third area of the structure encompassing the SUMO1-RanGAP1^{CTD}/Ubc9/RanBP2^{IR1} subcomplex was determined using a similar strategy whereby regions of the map not encompassing this subcomplex were subtracted from all particles, followed by a 3D focused classification with no image alignment, to isolate all particles that included the SUMO1-RanGAP1^{CTD}/Ubc9/RanBP2^{IR1} subcomplex. The final postprocessed maps for the SUMO1-RanGAP1^{CTD}/Ubc9/RanBP2^{IR1} subcomplex were resolved to 3.29 Å and 3.1 Å resolution after focused refinements.

Model building and refinement

Components of atomic models for the RanBP2^{RBD4}/SUMO1-RanGAP1/Ubc9/Crm1/Ran^{Q69L}(GTP) complex were docked into individual maps and manually rebuilt with Coot[80] using a prior crystal structure of human SUMO2-RanGAP1^{CTD}/Ubc9/RanBP2^{IR1} (PDB: 3UIN), human Snurportin1 and Ran(GTP) and mouse Crm1 (PDB: 3GJX), human RanBP2 RBD1 (PDB: 4L6E), and the human Ran(GMPPNP) complex with human RanBP1 and the *Schizosaccharomyces pombe* GAP domain of RanGAP1

(PDB: 1K5D). These models were used with all of the aforementioned individual reconstructions generate a composite map using Phenix.[81] Elements of RanBP2, SUMO1 and other non-human components from docked crystal structures were then manually placed or rebuilt into the composite map using Coot and refined using Phenix. Model geometry was analyzed using Molprobity.[82] Local resolution maps were generated using Phenix. Structures and maps were rendered using ChimeraX[83] or Pymol (Schrödinger, LLC).

Biochemical assays

SUMO-conjugation assays

Wild type RanGAP1 and RanGAP1$^{\Delta N18}$ were purified as described above for SUMO conjugation assays and conjugated to SUMO1^{Q94P} largely as described in the "Electron Microscopy Sample Preparation, Imaging and Analysis" section except the conjugation was allowed to proceed for 18 hours at 37 °C and Mono Q 10/100 purification was done in 50 mM Tris pH 7.5, 1 mM DTT, 0.5 mM EDTA using a linear gradient of 250 mM to 600 mM NaCl over 15 column volumes to elute the protein. SUMO2$^{1-93,A2C}$ was conjugated to Alexa488-maleimide as previously described for SUMO2$^{1-93,A2C,C48A}$.[33]

For conjugation reactions with RanBP2^{RBD3-4}, RanBP2$^{RBD3-4,\Delta IR1(I/II)}$, and RanBP2$^{RBD3-4,\Delta IR2(I/II)}$, 300 nM Ubc9 (E2), 100 nM Aos1/Uba2$^{\Delta C}$ (E1), 5 µM SUMO2$^{1-93,A2C}$-Alexa488, 2 µM Incenp$^{1-58}$-Survivin-Borealin (ISB), 500 nM Rcc1, 200 nM SUMO1^{Q94P}-RanGAP1, 750 nM Crm1, 100 nM RanBP2 variant (E3), 500 nM Ran variant (when present), and 3 mM GTP or GDP were incubated on ice in Buffer K (20 mM HEPES pH 7.5, 100 mM KOAc, 5 mM $MgCl_2$, 1 mM TCEP) and reaction was started by the addition of 1 mM ATP and transferred to a 37 °C heat block. After 50 minutes at 37 °C, 8 µL of sample was quenched with 4 µL of 4x NuPAGE LDS (Thermo) containing DTT. 6 µL of quenched reaction was run on 4-12% NuPAGE Bis-Tris gel (Thermo) and gel was scanned with Typhoon FLA-9500 (Cytiva) at 500V using the 473 nm laser

line. Intensity of bands corresponding to SUMO2-conjugated Borealin were quantified with ImageJ and plotted using Prism (GraphPad). To test the effect of the N-terminus of RanGAP1 and Crm1 on E3 ligase activity of RanBP2^{RBD3-4}, reactions were performed essentially as described above except 3.2 μM Ran^{Q69L}(GTP) or 3.2 μM wild type Ran was used, Crm1 was titrated starting at 1.6 μM via 2-fold serial dilutions, and reactions were run at 37 °C for 96 minutes for Ran^{Q69L} experiments and for 50 minutes for wild type Ran assays.

GTPase assays

RanBP2^{RBD3-4}/SUMO1-RanGAP1/Ubc9 complexes were first reconstituted by incubating RanBP2^{RBD3-4}, SUMO1^{Q94P}-RanGAP1, and Ubc9, purified as described for cryo-EM reconstitutions, overnight at 4 °C in a buffer containing 50 mM Tris pH 7.5, 150 mM NaCl, 0.5 mM DTT, and 0.25 mM EDTA in the presence of thrombin to cleave off residual His_6 tags. Reconstituted complexes were injected onto a Mono Q 10/100 GL column equilibrated in 50 mM Tris pH 7.5, 150 mM NaCl, and 1 mM DTT. Protein was eluted in a linear gradient from 250 mM NaCl to 600 mM NaCl in 15 column volumes. Peak fractions were concentrated, exchanged into a buffer containing 50 mM Tris pH 7.5, 300 mM NaCl, 1 mM TCEP, and injected onto the Superdex Increase 10/300 GL equilibrated in the same buffer. Peak fractions were pooled, concentrated, aliquoted, and flash frozen.

All assays were done in clear 96-well Costar flat bottom plates (Corning 3370) at 37 °C in an M5 SpectraMax plate reader (Molecular Devices) with the lid on. Real time GTPase activity was measured by measuring phosphate release, which is coupled to absorption change at 360 nm by the action of PNP on its substrate MESG, using the EnzChek Phosphate Assay Kit (Thermo). Experiments were performed in a buffer consisting of 50 mM Tris pH 7.5, 150 mM NaCl, 2 mM $MgCl_2$, 0.25 mM TCEP in a reaction volume of 100 μL. Reactions consisted of a 25 nM complex of RanBP2^{RBD3-4} preassembled with SUMO1^{Q94P}-RanGAP1/Ubc9 or SUMO1^{Q94P}-RanGAP1$^{\Delta N18}$/Ubc9 as described above; 2 μM Rcc1; 3 μM Crm1 when present; 5 μM Spn1

when present; varying concentrations of Ran; 200 μM MESG; 1 U/mL PNPase; and 1 mM GTP. Components were preincubated at 37 °C for 5 minutes, the RanBP2^{RBD3-4}/SUMO1^{Q94P}-RanGAP1/Ubc9 complex was added to initiate the reaction, and reaction progress was monitored by absorbance at 360 nm every 4 or 5 seconds. Slope was calculated for the linear portion of the reaction and μM phosphate hydrolyzed min^{-1} was calculated using an equation derived from a phosphate standard curve generated using known free phosphate concentrations and measuring absorbance of MESG after PNPase action under the utilized experimental conditions.

Generation of RanGAP1$^{\Delta NES}$ cell lines by CRISPR-Cas9

Vectors, primers, and guide RNAs used for CRISPR

pSpCas9(BB)-2A-GFP (PX458) was a gift from Feng Zhang (Addgene plasmid # 48138; http://n2t.net/addgene:48138; RRID:Addgene 48138). PX458 harboring mCherry instead of EGFP (PX458-mCherry) was constructed by digesting parental PX458 with EcoRI and ligating a T2A-mCherry gBlock (IDT) also digested with EcoRI. Guide RNAs with the sequences CAGCTTGGCAATGTCTTCCG (sgRNA236, target site 10 base pairs from A of the initiator ATG codon of the RanGAP1 gene) and GACACTTGCCAAGACTCAGG (sgRNA240, target site 49 base pairs from A of the initiator ATG codon of the RanGAP1 gene) where generated with BbsI sites, annealed, and cloned into PX458 and PX458-mCherry using the BbsI restriction site following Zhang lab general cloning protocol (https://media.addgene.org/cms/filer_public/6d/d8/6dd83407-3b07-47db-8adb-4fada30bde8a/zhang-lab-general-cloning-protocol-target-sequencing_1.pdf). PCR amplification of genomic DNA for verification of CRISPR-mediated deletion was done with primers VB243 (TACTGCAACTTTGGCCTCCT) and VB244 (GGGCAAATGATCTCTGAGCC) which bind upstream of exon 1 and between exons 1 and 2, respectively.

Transfection with CRISPR-Cas9 plasmids and selection of single clones

Human hTERT-immortalized retinal pigment epithelial cells (hTERT-RPE1; ATCC, CRL-4000) were maintained at 37 °C and 5% CO_2 in regular media (DME:F12 HG containing 15 mM HEPES, 2.4 mg/mL $NaHCO_3$, 2.5 mM L-glutamine (MSK Media Preparation Core)) supplemented with 10% FBS (Sigma, F2442) and 1% penicillin/streptomycin (Gibco). Prior to transfection, cells were moved to antibiotic-free media. At ~70% confluency, one 10 cm plate of hTERT-RPE1 cells was co-transfected with 10 µg of PX458 harboring sgRNA236 and 10 µg of PX458-mCherry harboring sgRNA240 using 43.4 µL Lipofectamine 3000 and 40 µL P3000 reagent following the Lipofectamine 3000 protocol (Thermo). Three days post transfection cells were trypsinized, resuspended in FACS-sorting media (1x PBS with 25 mM HEPES pH 7.0, 2% FBS, 2 mM EDTA), and sorted on an Aria flow cytometer (BD, MSK Flow Cytometry Core Facility) selecting for top GFP and mCherry co-expressing cells (~5600 cells; about 12% of FACS input). Sorted cells were maintained in regular media with 1% pen/strep for 3 weeks then dilution cloned on 24-well plates at 0.5 cells/well. Single clones were expanded to 6-well plates after ~ 2 weeks of growth on 24-well plates and genomic DNA was extracted using Quick Extract DNA extraction solution (Lucigen). Primers flanking the expected deletion region (VB243 and VB244) were used to screen for clones with deleted RanGAP1 residues 5-17 (a ~40 base pair deletion compared to wild type). PCR products corresponding to the size of the expected 40 base pair deletion were gel extracted and cloned into CloneJet (Thermo) for sequencing. Western blots on whole cell lysates with several α-RanGAP1 antibodies (Sigma HPA062034, Santa Cruz sc-28322) were done on each clone to confirm the expression of truncated RanGAP1.

<u>Generation of stable hTERT-RPE1 cell lines</u>

Cloning of constructs

Full length wild type RanGAP1 or full length RanGAP1 containing the I6A, L9A, L13A, T16A mutations (4A mutant) were cloned on the N-terminus of monomeric EGFP in the mEGFP-N1 vector (mEGFP-N1 was a gift from Michael Davidson - Addgene plasmid # 54767; http://n2t.net/addgene:54767; RRID:Addgene_54767) via restriction site cloning (BglII, KpnI sites). PCR was then used to delete residues 19-587 of RanGAP1 to generate RanGAP1$^{1\text{-}18\text{-}WT}$-mEGFP and RanGAP1$^{1\text{-}18\text{-}4AMUT}$-mEGFP. To generate pEGFP-N1-2xGFP:NES-IRES-2xRFP:NLS, pLVX-EF1alpha-2xGFP:NES-IRES-2xRFP:NLS was used as template for PCR addition of NheI and XbaI sites to the 2xGFP:NES-IRES-2xRFP:NLS insert (pLVX-EF1alpha-2xGFP:NES-IRES-2xRFP:NLS was a gift from Fred Gage; Addgene plasmid # 71396; http://n2t.net/addgene:71396; RRID:Addgene_71396), and the insert was cut out and ligated into pEGFP-N1 plasmid prepped from a *dam*$^-$ *dcm*$^-$ *E.coli* strain (New England Biolabs Cat# C2925H) and digested with NheI and XbaI. NLS-mCherry-LEXY (pDN122) was a gift from Barbara Di Ventura & Roland Eils (Addgene plasmid # 72655; http://n2t.net/addgene:72655; RRID:Addgene_72655). NES-mCherry-LiNUS (pDN77) was a gift from Barbara Di Ventura & Roland Eils (Addgene plasmid # 61347; http://n2t.net/addgene:61347; RRID:Addgene_61347).

Transfection and generation of stable cell lines

hTERT-RPE1 cells were maintained in DME:F12 HG media containing 15 mM HEPES, 2.4 mg/mL $NaHCO_3$, 2.5 mM L-glutamine supplemented with 10% FBS and 1% penicillin/streptomycin as described above. To generate stable hTERT-RPE1 cell lines, 2.5 µg of plasmid was transfected into the appropriate hTERT-RPE1 cell line at ~70-90% confluency following the Lipofectamine 3000 manufacturer's protocol. After 5-7 days, cells were moved into the same DME:F12 media but supplemented with 300 µg/mL G418 (Sigma) instead of 1% pen/strep. After 16-17 days in selection media, aliquots of cells were frozen down in Recovery Cell Culture Medium (Gibco) and passaging was continued in regular media supplemented with

200 µg/mL G418 in the absence of pen/strep. hTERT-RPE1 cells expressing 2xGFP:NES-IRES-2xRFP:NLS were further sorted by FACS on an Aria flow cytometer (MSK Flow Cytometry Core Facility) for the top-expressing GFP^+/RFP^+ double positive cells using the same gating for wild type and $RanGAP1^{\Delta NES}$ expressing cell lines.

Confocal microscopy and calculation of N/C ratios

Leptomycin B treatment and fixation for confocal microscopy for RanGAP1 and Ran N/C localization analyses

Wild type RPE1 and $RanGAP1^{\Delta NES}$ cells were plated on 4-well µ-slides (Ibidi), allowed to attach overnight, and 50 nM leptomycin B (LMB, Enzo Life Sciences) was added for 20-21 hours where indicated. Cells were washed twice with 1x PBS containing 1 mM $MgCl_2$ and 1 mM $CaCl_2$ (PBS^{++}) and fixed in 2% paraformaldehyde (PFA, Biotium) in PBS for 20 minutes at room temperature. After fixation, cells were washed three times in 1x TBS containing 0.05 % Tween-20 (TBST, Thermo) and then permeabilized in 100% methanol for 20 minutes at -20°C. Cells were washed three times with ice cold TBST and incubated with TBST containing 2% BSA (TBSTB) for 30 minutes at room temperature. For RanGAP1 localization experiments, rabbit α-RanGAP1 primary antibody (Bethyl, A302-027A) was diluted 1:1000 in TBST. For Ran localization experiments, mouse α-Ran primary antibody, (BD, 610340) and rabbit α-RanGAP1 primary antibody (Bethyl, A302-027A) were diluted 1:250 and 1:1000, respectively, in TBST. The primary antibodies were added to cells and incubated overnight at 4°C with mild agitation. Cells were washed three times with TBST for 5 minutes each at room temperature. For RanGAP1 localization studies, alpaca α-rabbit-IgG secondary nanobody conjugated to Alexa-647 (Thermo SA5-10327) was diluted in TBSTB at 1:1000 and incubated with cells for 30 minutes at room temperature. For Ran localization experiments, alpaca anti-rabbit IgG secondary nanobody conjugated to Alexa488 (VHH, Thermo SA5-10323) and donkey anti-

mouse IgG secondary antibody conjugated to Alexa647 (H+L Thermo A32787) were each diluted in TBSTB at 1:1000 and added to cells for 30 minutes at room temperature. Cells were washed again in TBST three times for 5 minutes each at room temperature and mounted with 250µL per well of Vectashield Plus Antifade Mounting Medium with DAPI (Vector Laboratories, H-2000).

Fixation of RanGAP1$^{1\text{-}18\text{-}WT}$-mEGFP and RanGAP1$^{1\text{-}18\text{-}4AMUT}$-mEGFP for confocal microscopy

Stable cell lines expressing RanGAP1$^{1\text{-}18\text{-}WT}$-mEGFP or RanGAP1$^{1\text{-}18\text{-}4AMUT}$-mEGFP were plated on 4-well Ibidi µ-slides and allowed to attach overnight. Cells were washed once with PBS^{++}, incubated in transport buffer (20 mM HEPES pH 7.5, 110 mM KoAc, 2 mM $Mg(OAC)_2$, 0.5 mM EGTA, 2mM DTT, 1x Halt protease/phosphatase inhibitor (Thermo)) for 4 minutes at room temperature, and washed twice with PBS^{++} again. Cells were fixed in 3% PFA for 15 minutes at room temperature, washed three times in TBST, and mounted with 250 µL per well of Vectashield Plus Antifade Mounting Medium with DAPI.

Preparation of cells expressing 2xGFP-NES-IRES-2xRFP-NLS, NLS-mCherry-LEXY, and NES-mCherry-LiNUS for live imaging

Stable, FACS-sorted wild type RPE1 and RanGAP1$^{\Delta NES}$ clone #2 cells expressing 2xGFP-NES-IRES-2xRFP-NLS were plated on 4-well Ibidi µ-slides and allowed to attach overnight. 50 nM LMB was added for 21-24 hours where indicated. Media was supplemented with 1x NucSpot 650 (Biotium) to stain nuclei prior to imaging. Wild type RPE1 cells and RanGAP1$^{\Delta NES}$ clones 2 and 10 stably expressing NLS-mCherry-LEXY or NES-mCherry-LiNUS (but not FACS-sorted) were prepared for imaging in the same way except without LMB addition.

Imaging and calculation of N/C ratios

Imaging of fixed cells was done on a laser-scanning Leica TCS SP8 confocal microscope with the 63x/1.4 HC PL APO CS2 objective in oil and using the white light laser for excitation (MSK Molecular Cytology Core Facility). Z-stack images in steps of 0.5 μm were acquired and the images with the maximum DAPI signal +/- 1 μm were 2D-projected using average projection in FIJI[84] and fed into custom CellProfiler[74] pipelines. Briefly, for calculation of RanGAP1 N/C ratios, nuclei were first automatically identified from the DAPI signal using adaptive Otsu thresholding and single nuclei were manually confirmed. Next, cell boundaries were automatically identified from the RanGAP1 signal using the "Watershed – Image" method and a global robust background thresholding strategy. Correctly identified cell boundaries were manually confirmed and total cytoplasmic RanGAP1 signal intensity was calculated by subtracting total nuclear RanGAP1 signal intensity from total whole cell RanGAP1 signal intensity. Nuclear ring staining signal was not counted as part of nuclear signal (i.e. it was assumed to be cytoplasmic). Nuclear to cytoplasmic ratio was calculated by dividing average RanGAP1 nuclear signal intensity over average RanGAP1 cytoplasmic signal intensity. N/C ratios for Ran were calculated by using the RanGAP1 signal to mark cell boundaries and dividing average nuclear over the average cytoplasmic Ran signal using a very similar custom CellProfiler pipeline as that used for RanGAP1 calculations but without taking into the nuclear ring signal, which was not pronounced for Ran. Live imaging of cells expressing 2xGFPNES-IRES-2x-RFPNLS was done via the same microscope setup as for fixed cells but with the addition of the Tokai Hit STXG incubation chamber (MSK Molecular Cytology Core Facility) set to 37 °C and 5% CO_2. Z-stack images in 0.5 μm steps were acquired as described above and the images with the maximum NucSpot 650 signal +/- 1 μm were 2D-projected using average projection in FIJI. N/C ratios for cells were calculated by using the GFP signal to mark cell boundaries, NucSpot 650 signal to mark nuclei, and the same custom CellProfiler pipeline used for Ran N/C calculations.

Imaging and quantification of transport kinetics in NLS-mCherry-LEXY and NES-mCherry-LiNUS cell lines

Cells expressing NLS-mCherry-LEXY or NES-mCherry-LiNUS were grown on 4-well µ-slides and imaged in the presence of 1x NucSpot 650 on the Leica TCS SP8 confocal microscope equipped with the Tokai Hit STXG incubation chamber set to 37 °C and 5% CO_2 and the 20x/0.75 HC PL APO CS2 objective immersed in oil. Cells were incubated in the dark for at least 10 minutes prior to initiation of nuclear export (LEXY) or import (LiNUS) of mCherry, which was induced by 458 nm excitation via the Argon laser at 19.8 W output power (20% of maximum laser power). Pulsatile excitation at 458 nm continued every 2.57 seconds and images in the mCherry and NucSpot 650 channels were collected concurrently for 5-10 minutes. Images were processed in FIJI as follows. First, nuclear masks were made using the NucSpot 650 signal and thresholding via the Default method. Next, the Trackmate[85] plugin was used to track individual nuclei and measure their mCherry fluorescence over time. Lastly, mCherry fluorescence was plotted against time and fit to a single exponential in Prism and the half-life of each curve was calculated.

Flow cytometry and mitotic index determination

Wild type RPE1 cells or RanGAP1$^{\Delta NES}$ clones 2 and 10 were grown on 10 cm plates to 40-70% confluence and pulsed with 10 µM BrdU (BD Pharmigen flow kit) for 45 minutes. Cells were trypsinized and fixed with 2% PFA in PBS (Biotium) for 10 minutes at room temperature. Fixed cells were washed with FACS staining buffer (PBS with 3% FBS (Sigma) and 0.03% azide) followed by a wash with ice cold PBS and permeabilized with 100% MeOH (1 mL per $1x10^6$ cells) overnight at -20 °C. Permeabilized cells were washed several times in FACS staining buffer, resuspended in 100 µL DNAse (300 µg/mL, BD Pharmigen flow kit), and incubated for 1 hour at 37 °C. Cells were washed with FACS staining buffer and incubated with

α-BrdU antibody conjugated to APC (1:50, BD Pharmigen flow kit) and α-pHH3 (Ser10) antibody conjugated to R-phycoerythrin (2.5 µg/mL, BioLegends) for 20 minutes at room temperature. Antibody-stained cells were washed in FACS staining buffer and resuspended in 20 µL 7-actinomycin D (7-AAD, BD Pharmigen flow kit) for 5 minutes at room temperature. 250 µL of FACS staining buffer was added and cells were sorted on a CytoFLEX LX Flow cytometer (Beckman, MSK Flow Cytometry Core Facility) using appropriate lasers for PE (585 nm), 7-AAD (690 nm), and APC (660 nm). Data was processed with FlowJo (BD) and cell populations in G0/G1, S, and G2/M were visualized by plotting the α-BrdU-APC signal vs. 7-AAD whereas mitotic cells were visualized by plotting the α-BrdU-APC signal vs. the α-pHH3-PE signal.

Western Blots

Cell pellets were lysed in 50 mM Tris pH 7.5, 150 mM NaCl, 0.5 mM EDTA, 2 mM DTT, and 2% SDS at 70 °C and passed through an 18 gauge needle several times prior to quantification of total protein via Bradford. 4x LDS (Thermo) and DTT were added to the sample to a final 1x concentration (40 mM DTT in 1x) and 10-30 µg of total protein was loaded onto 4-12% Bis-Tris gels (Thermo) and run in MOPS or MES buffer (Thermo). Gels were transferred via the Trans-Blot Turbo transfer instrument (BioRad) at a constant current of 2.5 A and variable voltage of up to 25 V for 10 minutes using the Trans-Blot Turbo Mini 0.2 µm PVDF Transfer Packs (BioRad). Membranes were blocked for 2 hours at room temperature in Tris-buffered saline (TBS) + 0.1% Tween-20 + 5% non-fat milk (block buffer) and incubated with primary antibodies overnight at 4 °C in TBS + 0.1% Tween-20 + 2% non-fat milk (Ab buffer). Blots were washed in TBS + 0.1% Tween-20 (Western wash buffer) and incubated with secondary antibodies in Ab buffer for 1 hour at room temperature. Blots were washed in Western wash buffer, developed using ECL Prime Western Blotting detection reagent (Cytiva), and imaged on a ChemiDoc XRS+ imager (BioRad). The following primary antibodies were used for Western

blots: α-RanGAP1 (Sigma, HPA062034); α-β-actin (Santa Cruz, sc81178); α-β-actin (Novus, NBP1-47423); α-Ran (BD, 610340).

Table S1. EM data and refinement, Related to Figs. S1, S2 and STAR Methods.

	RanBP2/Ubc9/SUMO1-RanGAP1/Ran(GTP)/Crm1/Ran(GTP) complex – K2
Data collection	Dataset 1 - 4
Magnification	22,500x
Voltage (kV)	300
Electron exposure ($e^-/Å^2$)	85.2
Defocus range (μm)	-1.0 to -3.0
Super-resolution pixel size (Å)	0.544
Fourier cropped pixel size (Å)	1.088
Initial particle projections (#)	540,834
Final particle projections (#)	
Overall map	
(All components)	534,708
Focused Refinement (Foc. Ref.)	
Crm1/Ran(GTP)	534,708
Overall map	
RanBP2-RBD4/Ran(GTP)/RanGAP1-GAP	287,278
Foc. Ref.	
RanBP2-RBD4/Ran(GTP)	287,278
RanGAP1-GAP	287,278
Overall map	
RanBP2/Ubc9/SUMO1-RanGAP1/Ran(GTP)	61,110
Foc. Ref.	
RanBP2/Ubc9/SUMO1-RanGAP1	61,110
Crm1/Ran(GTP)/Ubc9/SUMO1-RanGAP1	61,110
Symmetry imposed	C1
Map resolution (Å)	
FSC threshold = 0.143	
Overall	
(All components)	3.18
Focused Refinement (Foc. Ref.)	
Crm1/Ran(GTP)	2.89
Overall	
RanBP2-RBD4/Ran(GTP)/RanGAP1-GAP	3.52
Foc. Ref.	
RanBP2-RBD4/Ran(GTP)	3.52
RanGAP1-GAP	3.37
Overall	
RanBP2/Ubc9/SUMO1-RanGAP1/Ran(GTP)	3.40
Foc. Ref.	
RanBP2/Ubc9/SUMO1-RanGAP1	3.29
Crm1/Ran(GTP)/Ubc9/SUMO1-RanGAP1	3.10
Map resolution range (Å)	**Box (contoured)**
Overall	
(All components)	2.44-10.70 (2.59-7.39; 0.055 sig)
Focused Refinement (Foc. Ref.)	
Crm1/Ran(GTP)	2.32-9.80 (2.42-5.59; 0.050 sig)
Overall	
RanBP2-RBD4/Ran(GTP)/RanGAP1-GAP	2.57-11.86 (2.74-6.04; 0.045 sig)
Foc. Ref.	
RanBP2-RBD4/Ran(GTP)	2.67-11.33 (2.86-6.20; 0.045 sig)
RanGAP1-GAP/Ran(GTP)	2.63-11.98 (2.63-4.02; 0.045 sig)
Overall	
RanBP2/Ubc9/SUMO1-RanGAP1/Ran(GTP)	2.56-11.82 (2.70-8.58; 0.035 sig)
Foc. Ref.	
RanBP2/Ubc9/SUMO1-RanGAP1	2.96-11.11 (2.95-6.05; 0.025 sig)
Crm1/Ran(GTP)/Ubc9/SUMO1-RanGAP1	2.50-10.48 (2.69-6.52; 0.045 sig)
Refinement	
Initial models used (PDB code)	3UIN, 3GJX, 4L6E, 1K5D
Model resolution (Å) FSC threshold = 0.5	2.97
Map sharpening B factor ($Å^2$)	
Overall map	
(All components)	-82.11
Focused Refinement (Foc. Ref.)	
Crm1/Ran(GTP)	-63.36
Overall map	
RanBP2-RBD4/Ran(GTP)/RanGAP1-GAP	-135.37
Foc. Ref.	
RanBP2-RBD4/Ran(GTP)	-142.82
RanGAP1-GAP	-154.44
Overall map	
RanBP2/Ubc9/SUMO1-RanGAP1/Ran(GTP)	-55.18
Foc. Ref.	
RanBP2/Ubc9/SUMO1-RanGAP1	-86.25
Crm1/Ran(GTP)/Ubc9/SUMO1-RanGAP1	-53.40
Model composition	
Non-hydrogen atoms	19,287
Protein residues	2,414
Nucleic acid residues	2
Ligand (Mg^{2+})	2
Mean *B* factors	
Protein	62.9
Nucleic acid	40.8
Ligand (Mg^{2+})	43.4
RMS deviations	
Bond lengths (Å)	0.003
Bond angles (°)	0.447
Validation	
Molprobity score	1.43
Clashscore	4.14
Rotamer Outliers (%)	1.54
C-beta deviations (%)	0
Ramachandran plot	
% favored	92.11
% allowed	7.89
% outliers	0

References

1. Petrovic, S., Mobbs, G.W., Bley, C.J., Nie, S., Patke, A., and Hoelz, A. (2022). Structure and Function of the Nuclear Pore Complex. Cold Spring Harb Perspect Biol *14*. 10.1101/cshperspect.a041264.
2. Paine, P.L., Moore, L.C., and Horowitz, S.B. (1975). Nuclear envelope permeability. Nature *254*, 109-114. 10.1038/254109a0.
3. Keminer, O., and Peters, R. (1999). Permeability of single nuclear pores. Biophys J *77*, 217-228. 10.1016/s0006-3495(99)76883-9.
4. Görlich, D., Seewald, M.J., and Ribbeck, K. (2003). Characterization of Ran-driven cargo transport and the RanGTPase system by kinetic measurements and computer simulation. Embo j *22*, 1088-1100. 10.1093/emboj/cdg113.
5. Wing, C.E., Fung, H.Y.J., and Chook, Y.M. (2022). Karyopherin-mediated nucleocytoplasmic transport. Nature Reviews Molecular Cell Biology *23*, 307-328. 10.1038/s41580-021-00446-7.
6. Kalab, P., Weis, K., and Heald, R. (2002). Visualization of a Ran-GTP gradient in interphase and mitotic Xenopus egg extracts. Science *295*, 2452-2456. 10.1126/science.1068798.
7. Bischoff, F.R., Klebe, C., Kretschmer, J., Wittinghofer, A., and Ponstingl, H. (1994). RanGAP1 induces GTPase activity of nuclear Ras-related Ran. Proc Natl Acad Sci U S A *91*, 2587-2591. 10.1073/pnas.91.7.2587.
8. Bischoff, F.R., and Ponstingl, H. (1991). Catalysis of guanine nucleotide exchange on Ran by the mitotic regulator RCC1. Nature *354*, 80-82. 10.1038/354080a0.
9. Wu, J., Matunis, M.J., Kraemer, D., Blobel, G., and Coutavas, E. (1995). Nup358, a cytoplasmically exposed nucleoporin with peptide repeats, Ran-GTP binding sites, zinc fingers, a cyclophilin A homologous domain, and a leucine-rich region. J Biol Chem *270*, 14209-14213. 10.1074/jbc.270.23.14209.
10. Wilken, N., Senécal, J.L., Scheer, U., and Dabauvalle, M.C. (1995). Localization of the Ran-GTP binding protein RanBP2 at the cytoplasmic side of the nuclear pore complex. Eur J Cell Biol *68*, 211-219.
11. Bley, C.J., Nie, S., Mobbs, G.W., Petrovic, S., Gres, A.T., Liu, X., Mukherjee, S., Harvey, S., Huber, F.M., Lin, D.H., et al. (2022). Architecture of the cytoplasmic face of the nuclear pore. Science *376*, eabm9129. 10.1126/science.abm9129.
12. Desgraupes, S., Etienne, L., and Arhel, N.J. (2023). RANBP2 evolution and human disease. FEBS Lett *597*, 2519-2533. 10.1002/1873-3468.14749.
13. Yokoyama, N., Hayashi, N., Seki, T., Panté, N., Ohba, T., Nishii, K., Kuma, K., Hayashida, T., Miyata, T., Aebi, U., and et al. (1995). A giant nucleopore protein that binds Ran/TC4. Nature *376*, 184-188. 10.1038/376184a0.
14. Matunis, M.J., Wu, J., and Blobel, G. (1998). SUMO-1 modification and its role in targeting the Ran GTPase-activating protein, RanGAP1, to the nuclear pore complex. J Cell Biol *140*, 499-509. 10.1083/jcb.140.3.499.
15. Mahajan, R., Gerace, L., and Melchior, F. (1998). Molecular characterization of the SUMO-1 modification of RanGAP1 and its role in nuclear envelope association. J Cell Biol *140*, 259-270. 10.1083/jcb.140.2.259.
16. Hutten, S., Flotho, A., Melchior, F., and Kehlenbach, R.H. (2008). The Nup358-RanGAP complex is required for efficient importin alpha/beta-dependent nuclear import. Mol Biol Cell *19*, 2300-2310. 10.1091/mbc.e07-12-1279.

17. Ritterhoff, T., Das, H., Hofhaus, G., Schroder, R.R., Flotho, A., and Melchior, F. (2016). The RanBP2/RanGAP1*SUMO1/Ubc9 SUMO E3 ligase is a disassembly machine for Crm1-dependent nuclear export complexes. Nat Commun *7*, 11482. 10.1038/ncomms11482.
18. Yaseen, N.R., and Blobel, G. (1999). Two distinct classes of Ran-binding sites on the nucleoporin Nup-358. Proc Natl Acad Sci U S A *96*, 5516-5521. 10.1073/pnas.96.10.5516.
19. Saitoh, H., Pu, R., Cavenagh, M., and Dasso, M. (1997). RanBP2 associates with Ubc9p and a modified form of RanGAP1. Proc Natl Acad Sci U S A *94*, 3736-3741. 10.1073/pnas.94.8.3736.
20. Kerscher, O., Felberbaum, R., and Hochstrasser, M. (2006). Modification of proteins by ubiquitin and ubiquitin-like proteins. Annu Rev Cell Dev Biol *22*, 159-180. 10.1146/annurev.cellbio.22.010605.093503.
21. Streich, F.C., Jr., and Lima, C.D. (2014). Structural and functional insights to ubiquitin-like protein conjugation. Annu Rev Biophys *43*, 357-379. 10.1146/annurev-biophys-051013-022958.
22. Cappadocia, L., and Lima, C.D. (2018). Ubiquitin-like Protein Conjugation: Structures, Chemistry, and Mechanism. Chem Rev *118*, 889-918. 10.1021/acs.chemrev.6b00737.
23. Matunis, M.J., Coutavas, E., and Blobel, G. (1996). A novel ubiquitin-like modification modulates the partitioning of the Ran-GTPase-activating protein RanGAP1 between the cytosol and the nuclear pore complex. J Cell Biol *135*, 1457-1470. 10.1083/jcb.135.6.1457.
24. Lee, G.W., Melchior, F., Matunis, M.J., Mahajan, R., Tian, Q., and Anderson, P. (1998). Modification of Ran GTPase-activating protein by the small ubiquitin-related modifier SUMO-1 requires Ubc9, an E2-type ubiquitin-conjugating enzyme homologue. J Biol Chem *273*, 6503-6507. 10.1074/jbc.273.11.6503.
25. Zhang, H., Saitoh, H., and Matunis, M.J. (2002). Enzymes of the SUMO modification pathway localize to filaments of the nuclear pore complex. Mol Cell Biol *22*, 6498-6508. 10.1128/mcb.22.18.6498-6508.2002.
26. Bernier-Villamor, V., Sampson, D.A., Matunis, M.J., and Lima, C.D. (2002). Structural basis for E2-mediated SUMO conjugation revealed by a complex between ubiquitin-conjugating enzyme Ubc9 and RanGAP1. Cell *108*, 345-356. 10.1016/s0092-8674(02)00630-x.
27. Reverter, D., and Lima, C.D. (2005). Insights into E3 ligase activity revealed by a SUMO-RanGAP1-Ubc9-Nup358 complex. Nature *435*, 687-692. 10.1038/nature03588.
28. Pichler, A., Gast, A., Seeler, J.S., Dejean, A., and Melchior, F. (2002). The nucleoporin RanBP2 has SUMO1 E3 ligase activity. Cell *108*, 109-120. 10.1016/s0092-8674(01)00633-x.
29. Saitoh, H., Sparrow, D.B., Shiomi, T., Pu, R.T., Nishimoto, T., Mohun, T.J., and Dasso, M. (1998). Ubc9p and the conjugation of SUMO-1 to RanGAP1 and RanBP2. Curr Biol *8*, 121-124. 10.1016/s0960-9822(98)70044-2.
30. Pichler, A., Knipscheer, P., Saitoh, H., Sixma, T.K., and Melchior, F. (2004). The RanBP2 SUMO E3 ligase is neither HECT- nor RING-type. Nat Struct Mol Biol *11*, 984-991. 10.1038/nsmb834.
31. Hochstrasser, M. (2001). SP-RING for SUMO: new functions bloom for a ubiquitin-like protein. Cell *107*, 5-8. 10.1016/s0092-8674(01)00519-0.

32. Ulrich, H.D. (2009). The SUMO system: an overview. Methods Mol Biol *497*, 3-16. 10.1007/978-1-59745-566-4_1.
33. Cappadocia, L., Pichler, A., and Lima, C.D. (2015). Structural basis for catalytic activation by the human ZNF451 SUMO E3 ligase. Nat Struct Mol Biol *22*, 968-975. 10.1038/nsmb.3116.
34. Plechanovová, A., Jaffray, E.G., Tatham, M.H., Naismith, J.H., and Hay, R.T. (2012). Structure of a RING E3 ligase and ubiquitin-loaded E2 primed for catalysis. Nature *489*, 115-120. 10.1038/nature11376.
35. Pruneda, Jonathan N., Littlefield, Peter J., Soss, Sarah E., Nordquist, Kyle A., Chazin, Walter J., Brzovic, Peter S., and Klevit, Rachel E. (2012). Structure of an E3:E2∼Ub Complex Reveals an Allosteric Mechanism Shared among RING/U-box Ligases. Molecular Cell *47*, 933-942. https://doi.org/10.1016/j.molcel.2012.07.001.
36. Dou, H., Buetow, L., Sibbet, G.J., Cameron, K., and Huang, D.T. (2013). Essentiality of a non-RING element in priming donor ubiquitin for catalysis by a monomeric E3. Nature Structural & Molecular Biology *20*, 982-986. 10.1038/nsmb.2621.
37. Hay, R.T. (2005). SUMO: A History of Modification. Molecular Cell *18*, 1-12. https://doi.org/10.1016/j.molcel.2005.03.012.
38. Tatham, M.H., Kim, S., Jaffray, E., Song, J., Chen, Y., and Hay, R.T. (2005). Unique binding interactions among Ubc9, SUMO and RanBP2 reveal a mechanism for SUMO paralog selection. Nat Struct Mol Biol *12*, 67-74. 10.1038/nsmb878.
39. Zhu, S., Goeres, J., Sixt, K.M., Békés, M., Zhang, X.D., Salvesen, G.S., and Matunis, M.J. (2009). Protection from isopeptidase-mediated deconjugation regulates paralog-selective sumoylation of RanGAP1. Mol Cell *33*, 570-580. 10.1016/j.molcel.2009.02.008.
40. Gareau, J.R., Reverter, D., and Lima, C.D. (2012). Determinants of small ubiquitin-like modifier 1 (SUMO1) protein specificity, E3 ligase, and SUMO-RanGAP1 binding activities of nucleoporin RanBP2. J Biol Chem *287*, 4740-4751. 10.1074/jbc.M111.321141.
41. Klein, U.R., Haindl, M., Nigg, E.A., and Muller, S. (2009). RanBP2 and SENP3 function in a mitotic SUMO2/3 conjugation-deconjugation cycle on Borealin. Mol Biol Cell *20*, 410-418. 10.1091/mbc.e08-05-0511.
42. Dawlaty, M.M., Malureanu, L., Jeganathan, K.B., Kao, E., Sustmann, C., Tahk, S., Shuai, K., Grosschedl, R., and van Deursen, J.M. (2008). Resolution of sister centromeres requires RanBP2-mediated SUMOylation of topoisomerase IIalpha. Cell *133*, 103-115. 10.1016/j.cell.2008.01.045.
43. Werner, A., Flotho, A., and Melchior, F. (2012). The RanBP2/RanGAP1*SUMO1/Ubc9 complex is a multisubunit SUMO E3 ligase. Mol Cell *46*, 287-298. 10.1016/j.molcel.2012.02.017.
44. Cha, K., Sen, P., Raghunayakula, S., and Zhang, X.D. (2015). The Cellular Distribution of RanGAP1 Is Regulated by CRM1-Mediated Nuclear Export in Mammalian Cells. PLoS One *10*, e0141309. 10.1371/journal.pone.0141309.
45. Feng, W., Benko, A.L., Lee, J.H., Stanford, D.R., and Hopper, A.K. (1999). Antagonistic effects of NES and NLS motifs determine S. cerevisiae Rna1p subcellular distribution. J Cell Sci *112 (Pt 3)*, 339-347. 10.1242/jcs.112.3.339.

46. Joseph, J., Tan, S.H., Karpova, T.S., McNally, J.G., and Dasso, M. (2002). SUMO-1 targets RanGAP1 to kinetochores and mitotic spindles. J Cell Biol *156*, 595-602. 10.1083/jcb.200110109.
47. Arnaoutov, A., Azuma, Y., Ribbeck, K., Joseph, J., Boyarchuk, Y., Karpova, T., McNally, J., and Dasso, M. (2005). Crm1 is a mitotic effector of Ran-GTP in somatic cells. Nat Cell Biol *7*, 626-632. 10.1038/ncb1263.
48. Sun, Q., Carrasco, Y.P., Hu, Y., Guo, X., Mirzaei, H., Macmillan, J., and Chook, Y.M. (2013). Nuclear export inhibition through covalent conjugation and hydrolysis of Leptomycin B by CRM1. Proc Natl Acad Sci U S A *110*, 1303-1308. 10.1073/pnas.1217203110.
49. Monecke, T., Güttler, T., Neumann, P., Dickmanns, A., Görlich, D., and Ficner, R. (2009). Crystal structure of the nuclear export receptor CRM1 in complex with Snurportin1 and RanGTP. Science *324*, 1087-1091. 10.1126/science.1173388.
50. Guttler, T., Madl, T., Neumann, P., Deichsel, D., Corsini, L., Monecke, T., Ficner, R., Sattler, M., and Gorlich, D. (2010). NES consensus redefined by structures of PKI-type and Rev-type nuclear export signals bound to CRM1. Nat Struct Mol Biol *17*, 1367-1376. 10.1038/nsmb.1931.
51. Port, S.A., Monecke, T., Dickmanns, A., Spillner, C., Hofele, R., Urlaub, H., Ficner, R., and Kehlenbach, R.H. (2015). Structural and Functional Characterization of CRM1-Nup214 Interactions Reveals Multiple FG-Binding Sites Involved in Nuclear Export. Cell Rep *13*, 690-702. 10.1016/j.celrep.2015.09.042.
52. Monecke, T., Dickmanns, A., and Ficner, R. (2014). Allosteric control of the exportin CRM1 unraveled by crystal structure analysis. FEBS J *281*, 4179-4194. 10.1111/febs.12842.
53. Koyama, M., Hirano, H., Shirai, N., and Matsuura, Y. (2017). Crystal structure of the Xpo1p nuclear export complex bound to the SxFG/PxFG repeats of the nucleoporin Nup42p. Genes Cells *22*, 861-875. 10.1111/gtc.12520.
54. Koyama, M., Shirai, N., and Matsuura, Y. (2014). Structural insights into how Yrb2p accelerates the assembly of the Xpo1p nuclear export complex. Cell Rep *9*, 983-995. 10.1016/j.celrep.2014.09.052.
55. Seewald, M.J., Körner, C., Wittinghofer, A., and Vetter, I.R. (2002). RanGAP mediates GTP hydrolysis without an arginine finger. Nature *415*, 662-666. 10.1038/415662a.
56. Bos, J.L., Rehmann, H., and Wittinghofer, A. (2007). GEFs and GAPs: critical elements in the control of small G proteins. Cell *129*, 865-877. 10.1016/j.cell.2007.05.018.
57. Vetter, I.R., Nowak, C., Nishimoto, T., Kuhlmann, J., and Wittinghofer, A. (1999). Structure of a Ran-binding domain complexed with Ran bound to a GTP analogue: implications for nuclear transport. Nature *398*, 39-46. 10.1038/17969.
58. Jumper, J., Evans, R., Pritzel, A., Green, T., Figurnov, M., Ronneberger, O., Tunyasuvunakool, K., Bates, R., Žídek, A., Potapenko, A., et al. (2021). Highly accurate protein structure prediction with AlphaFold. Nature *596*, 583-589. 10.1038/s41586-021-03819-2.
59. Raghunayakula, S., Subramonian, D., Dasso, M., Kumar, R., and Zhang, X.-D. (2015). Molecular Characterization and Functional Analysis of Annulate Lamellae Pore Complexes in Nuclear Transport in Mammalian Cells. PLOS ONE *10*, e0144508. 10.1371/journal.pone.0144508.

60. Swaminathan, S., Kiendl, F., Körner, R., Lupetti, R., Hengst, L., and Melchior, F. (2004). RanGAP1*SUMO1 is phosphorylated at the onset of mitosis and remains associated with RanBP2 upon NPC disassembly. J Cell Biol *164*, 965-971. 10.1083/jcb.200309126.
61. Mertens, J., Paquola, A.C.M., Ku, M., Hatch, E., Böhnke, L., Ladjevardi, S., McGrath, S., Campbell, B., Lee, H., Herdy, J.R., et al. (2015). Directly Reprogrammed Human Neurons Retain Aging-Associated Transcriptomic Signatures and Reveal Age-Related Nucleocytoplasmic Defects. Cell Stem Cell *17*, 705-718. 10.1016/j.stem.2015.09.001.
62. Niopek, D., Benzinger, D., Roensch, J., Draebing, T., Wehler, P., Eils, R., and Di Ventura, B. (2014). Engineering light-inducible nuclear localization signals for precise spatiotemporal control of protein dynamics in living cells. Nat Commun *5*, 4404. 10.1038/ncomms5404.
63. Niopek, D., Wehler, P., Roensch, J., Eils, R., and Di Ventura, B. (2016). Optogenetic control of nuclear protein export. Nat Commun *7*, 10624. 10.1038/ncomms10624.
64. Joseph, J., Liu, S.T., Jablonski, S.A., Yen, T.J., and Dasso, M. (2004). The RanGAP1-RanBP2 complex is essential for microtubule-kinetochore interactions in vivo. Curr Biol *14*, 611-617. 10.1016/j.cub.2004.03.031.
65. Swaminathan, S., Kiendl, F., Korner, R., Lupetti, R., Hengst, L., and Melchior, F. (2004). RanGAP1*SUMO1 is phosphorylated at the onset of mitosis and remains associated with RanBP2 upon NPC disassembly. J Cell Biol *164*, 965-971. 10.1083/jcb.200309126.
66. Di Cesare, E., Moroni, S., Bartoli, J., Damizia, M., Giubettini, M., Koerner, C., Krenn, V., Musacchio, A., and Lavia, P. (2023). Aurora B SUMOylation Is Restricted to Centromeres in Early Mitosis and Requires RANBP2. Cells *12*. 10.3390/cells12030372.
67. Gilistro, E., de Turris, V., Damizia, M., Verrico, A., Moroni, S., De Santis, R., Rosa, A., and Lavia, P. (2017). Importin-β and CRM1 control a RANBP2 spatiotemporal switch essential for mitotic kinetochore function. Journal of Cell Science *130*, 2564-2578. 10.1242/jcs.197905.
68. Chen, S., Lyanguzova, M., Kaufhold, R., Plevock Haase, K.M., Lee, H., Arnaoutov, A., and Dasso, M. (2021). Association of RanGAP to nuclear pore complex component, RanBP2/Nup358, is required for pupal development in Drosophila. Cell Rep *37*, 110151. 10.1016/j.celrep.2021.110151.
69. Paraskeva, E., Izaurralde, E., Bischoff, F.R., Huber, J., Kutay, U., Hartmann, E., Luhrmann, R., and Gorlich, D. (1999). CRM1-mediated recycling of snurportin 1 to the cytoplasm. J Cell Biol *145*, 255-264. 10.1083/jcb.145.2.255.
70. Sakin, V., Richter, S.M., Hsiao, H.H., Urlaub, H., and Melchior, F. (2015). Sumoylation of the GTPase Ran by the RanBP2 SUMO E3 Ligase Complex. J Biol Chem *290*, 23589-23602. 10.1074/jbc.M115.660118.
71. Shen, Q., Wang, Y.E., Truong, M., Mahadevan, K., Wu, J.J., Zhang, H., Li, J., Smith, H.W., Smibert, C.A., and Palazzo, A.F. (2021). RanBP2/Nup358 enhances miRNA activity by sumoylating Argonautes. PLoS Genet *17*, e1009378. 10.1371/journal.pgen.1009378.
72. Maarifi, G., Fernandez, J., Portilho, D.M., Boulay, A., Dutrieux, J., Oddos, S., Butler-Browne, G., Nisole, S., and Arhel, N.J. (2018). RanBP2 regulates the anti-retroviral activity of TRIM5α by SUMOylation at a predicted phosphorylated SUMOylation motif. Communications Biology *1*, 193. 10.1038/s42003-018-0198-0.
73. Nishijima, H., Nakayama, J., Yoshioka, T., Kusano, A., Nishitani, H., Shibahara, K., and Nishimoto, T. (2006). Nuclear RanGAP is required for the heterochromatin assembly and

is reciprocally regulated by histone H3 and Clr4 histone methyltransferase in Schizosaccharomyces pombe. Mol Biol Cell *17*, 2524-2536. 10.1091/mbc.e05-09-0893.
74. Stirling, D.R., Swain-Bowden, M.J., Lucas, A.M., Carpenter, A.E., Cimini, B.A., and Goodman, A. (2021). CellProfiler 4: improvements in speed, utility and usability. BMC Bioinformatics *22*, 433. 10.1186/s12859-021-04344-9.
75. Jeyaprakash, A.A., Klein, U.R., Lindner, D., Ebert, J., Nigg, E.A., and Conti, E. (2007). Structure of a Survivin-Borealin-INCENP core complex reveals how chromosomal passengers travel together. Cell *131*, 271-285. 10.1016/j.cell.2007.07.045.
76. Yunus, A.A., and Lima, C.D. (2009). Purification of SUMO conjugating enzymes and kinetic analysis of substrate conjugation. Methods Mol Biol *497*, 167-186. 10.1007/978-1-59745-566-4_11.
77. Mastronarde, D.N. (2005). Automated electron microscope tomography using robust prediction of specimen movements. J Struct Biol *152*, 36-51. 10.1016/j.jsb.2005.07.007.
78. Zheng, S.Q., Palovcak, E., Armache, J.P., Verba, K.A., Cheng, Y., and Agard, D.A. (2017). MotionCor2: anisotropic correction of beam-induced motion for improved cryo-electron microscopy. Nat Methods *14*, 331-332. 10.1038/nmeth.4193.
79. Zivanov, J., Nakane, T., Forsberg, B.O., Kimanius, D., Hagen, W.J., Lindahl, E., and Scheres, S.H. (2018). New tools for automated high-resolution cryo-EM structure determination in RELION-3. Elife *7*. 10.7554/eLife.42166.
80. Emsley, P., Lohkamp, B., Scott, W.G., and Cowtan, K. (2010). Features and development of Coot. Acta Crystallogr D Biol Crystallogr *66*, 486-501. 10.1107/s0907444910007493.
81. Adams, P.D., Afonine, P.V., Bunkóczi, G., Chen, V.B., Davis, I.W., Echols, N., Headd, J.J., Hung, L.W., Kapral, G.J., Grosse-Kunstleve, R.W., et al. (2010). PHENIX: a comprehensive Python-based system for macromolecular structure solution. Acta Crystallogr D Biol Crystallogr *66*, 213-221. 10.1107/s0907444909052925.
82. Chen, V.B., Arendall, W.B., 3rd, Headd, J.J., Keedy, D.A., Immormino, R.M., Kapral, G.J., Murray, L.W., Richardson, J.S., and Richardson, D.C. (2010). MolProbity: all-atom structure validation for macromolecular crystallography. Acta Crystallogr D Biol Crystallogr *66*, 12-21. 10.1107/s0907444909042073.
83. Pettersen, E.F., Goddard, T.D., Huang, C.C., Meng, E.C., Couch, G.S., Croll, T.I., Morris, J.H., and Ferrin, T.E. (2021). UCSF ChimeraX: Structure visualization for researchers, educators, and developers. Protein Sci *30*, 70-82. 10.1002/pro.3943.
84. Schindelin, J., Arganda-Carreras, I., Frise, E., Kaynig, V., Longair, M., Pietzsch, T., Preibisch, S., Rueden, C., Saalfeld, S., Schmid, B., et al. (2012). Fiji: an open-source platform for biological-image analysis. Nature Methods *9*, 676-682. 10.1038/nmeth.2019.
85. Tinevez, J.-Y., Perry, N., Schindelin, J., Hoopes, G.M., Reynolds, G.D., Laplantine, E., Bednarek, S.Y., Shorte, S.L., and Eliceiri, K.W. (2017). TrackMate: An open and extensible platform for single-particle tracking. Methods *115*, 80-90. https://doi.org/10.1016/j.ymeth.2016.09.016.